

DISS. ETH Nr. 26630

Haemolysis in Bearingless Centrifugal Pumps

A thesis submitted to attain the degree of

DOCTOR OF SCIENCES of ETH ZURICH
(Dr. sc. ETH Zurich)

presented by

PASCAL PÜNTENER

MSc ETH ME, ETH Zurich

born on 04.04.1989

citizen of Erstfeld, Uri

accepted on the recommendation of

Prof. Dr. Johann W. Kolar, examiner

Prof. Dr. Elena Lomonova, co-examiner

2020

ETH Zurich
Power Electronic Systems Laboratory
Technoparkstrasse 1
8005 Zurich
Switzerland

<http://www.pes.ee.ethz.ch>

© 2020 by Pascal Püntener

Preface

This thesis is the outcome of my doctoral studies at the Power Electronic Systems Laboratory at ETH Zurich, in close cooperation with the company Levitronix GmbH. The interdisciplinary character of the task made the doctorate extremely diverse and instructive.

I would like to express my special thanks to my supervisor, Prof. Dr. Johann W. Kolar, for the trust he has placed in me and for the opportunity to complete a doctorate with a close connection to the industry.

Furthermore, I would like to thank Prof. Dr. Elena Lomonova for her kind acceptance of the co-examination.

The cooperation with the company Levitronix has been very enjoyable. I owe this to all employees, who have always offered their friendly support. Special thanks go to Dr. Daniel Steinert, Dr. Thomas Nussbaumer, and Dr. Reto Schöb for the numerous discussions and helpful contributions.

I want to thank my co-doctoral students for the pleasant cooperation and lively discussions. The atmosphere was always very collegial and motivating. Special thanks go to Dr. Marcel Schuck for his untiring efforts in the numerous corrections and his help with the publications. His motivating manner contributed significantly to the success of the present work. I would also like to thank all the students whose work I got to supervise. Without their contributions, the present work would not have been possible to this extent. I particularly appreciate the assistance with the *in vitro* experiments. I would also like to thank the staff of the D-ITET workshop for the careful and professional processing of the prototypes.

Last but not least, I would like to thank my family, who always gave me support and helped me to get motivated. Special thanks to my wife Sabrina. Her excellent medical knowledge and many discussions helped me a lot in understanding the topics that were foreign to me. Especially since the birth of our son Andrin, her support has been invaluable.

Zurich, January 2020

Pascal Püntener

Abstract

Extracorporeal life support procedures are used to maintain blood circulation in case of organ failure and are required during open-heart surgery, as bridge-to-recovery or as destination therapy. Magnetically levitated pumps are already being implanted as ventricular assist devices. They cause fewer complications than diaphragm pumps and pumps with mechanical bearings. In particular, the risk of thrombus formation can be significantly reduced. For extracorporeal applications, such as cardiopulmonary bypass, extracorporeal membrane oxygenation, and dialysis machines, mechanical and peristaltic pumps are still dominantly used. This is for cost reasons and because magnetically levitated pumps did not yield sufficient improvements for such applications in the past.

In order to make the bearingless technology attractive for extracorporeal applications and to further increase the survival rate of the patients, the work at hand deals with the causes and the reduction of cell damage in bearingless centrifugal pumps. A suitable pump design can significantly reduce cell damage compared to the current market-leading products.

In the scope of this work, a low-haemolysis pump is designed, and several prototypes are implemented, which were used to investigate the cell damage with in vitro experiments. Additionally, CFD simulations were carried out. The factor with most important influence on cell damage was found to be the surface quality of the pump head. While a surface roughness of $R_a = 0.4 \mu\text{m}$ is sufficiently smooth under atmospheric conditions, the influence of the roughness increases with increasing pressure. For extracorporeal applications, the threshold value is lower. Even a local abrasive wear leads to significantly increased haemolysis.

Six different haemolysis models are implemented in fluid dynamic simulations. Although current approaches significantly overestimate cell damage, a good agreement with in vitro measurements can be achieved by appropriate parameter selection. Also, a high correlation can be shown with respect to geometry variations. The sensitivity of the model used is, however, lower than that of the in vitro experiments. Important effects, such as the surface quality, cannot be taken into account due to computational limitations.

Comprehensive investigations on the pump geometry showed that high cell damage occurs in the radial gap, between the impeller and

the housing, as well as at the inlet radius of the nozzle. Enlarging the radial gap by 75% reduces haemolysis by 25%. A larger fillet radius of the inlet nozzle allows for a further reduction by 40%.

To demonstrate the potential of the pump designed with the above mentioned aspects in mind, in vitro benchmark tests for comparison with commercial products were carried out. In addition to a reduction in haemolysis by 50%, the priming volume was reduced to half compared to the state of the art.

Kurzfassung

Bei Organversagen kommen extrakorporale Organersatzverfahren zum Einsatz welche den Kreislauf aufrechterhalten. Dies kann während einer Operation am offenen Herzen, als Überbrückung bis zur Transplantation oder als Dauerlösung erfolgen. Bereits heute werden magnetgelagerte Pumpen als Herzunterstützungssysteme implantiert, welche, gegenüber Membran- und mechanisch gelagerten Pumpen, weniger Komplikationen aufweisen. Insbesondere das Risiko der Thrombenbildung kann deutlich reduziert werden. Für extrakorporale Anwendungen, wie den kardiopulmonalen Bypass, Herz-Lungen-Maschinen und Dialysegeräte, dominieren nach wie vor mechanisch gelagerte Pumpen und Peristaltikpumpen.

Um die magnetisch gelagerten Pumpen auch für extrakorporale Anwendungen attraktiv zu gestalten und die Überlebenschancen von Patienten weiter zu steigern, befasst sich die vorliegende Arbeit mit den Ursachen und der Reduktion der Zellschädigung in lagerlosen Zentrifugalpumpen. Durch eine geeignete Konstruktion der Pumpe lässt sich die Zellschädigung gegenüber marktführenden Produkten deutlich verringern.

Im Rahmen dieser Arbeit wurde eine zellschonende Pumpe ausgelegt; nachfolgend wurden mehrere Prototypen implementiert, mithilfe deren die Zellschädigung simulativ und durch in vitro Experimente untersucht wurde. Als wichtigster Einflussfaktor stellte sich die Oberflächengüte des Pumpkopfs heraus. Während unter atmosphärischen Bedingungen ein Mittenrauwert von $R_a = 0.4 \mu\text{m}$ ausreichend ist, nimmt der Einfluss der Rauigkeit mit zunehmendem Druck zu. Für extrakorporale Anwendungen liegt der Schwellenwert tiefer. Bereits ein lokaler abrasiver Verschleiss führt zu einer deutlich erhöhten Hämolyse.

Sechs unterschiedliche Hämolysemodelle wurden in fluiddynamischen Simulationen implementiert. Obwohl die gängigen Ansätze die Zellschädigung in der Pumpe deutlich überschätzen, lässt sich durch eine geeignete Parameterwahl eine gute Übereinstimmung mit in vitro Messungen erreichen. Ebenfalls kann eine hohe Korrelation in Hinsicht auf Geometrievariationen aufgezeigt werden. Die Sensitivität des verwendeten Modells fällt allerdings geringer aus als jene der in vitro Experimente. Wichtige Effekte wie die Oberflächengüte können aufgrund limitierter Rechenleistung und einer geringen Datenbasis nicht berücksichtigt werden.

Umfassende Untersuchungen der Pumpengeometrie verdeutlichen,

dass im Radialspalt, zwischen Impeller und Gehäuse, sowie an der Rundung des Einlassstutzens, hohe Zellschädigungen auftreten. Durch eine Vergrößerung des Spalts um 75% lässt sich die Hämolyse um 25% reduzieren. Eine stärkere Rundung des Einlassstutzens ermöglicht eine weitere Reduktion um 40%.

Um das Potenzial einer Pumpe, welche unter Berücksichtigung der genannten Aspekte konstruiert wurde, aufzuzeigen, wurden in vitro Vergleichstests mit kommerziellen Produkten durchgeführt. Neben einer Reduktion der Hämolyse um 50% konnte auch das Primingvolumen gegenüber dem Stand der Technik halbiert werden.

Nomenclature

Symbols

Latin

A	surface	m^2
A	linear current density	A/m
B	magnetic flux density	T
\hat{c}_v	coefficient of variation	
d	diameter	m
D	pulse width	
e	error	
e	specific internal energy	J/kg
E	energy	J
f	frequency	Hz
f	force density	N/m ²
F	force	N
h	specific enthalpy	J/kg
h	height	m
H	magnetic field strength	H
H_b	haemoglobin	mg/dl
$H_{b,pf}$	plasma-free haemoglobin	mg/dl
HI	index of haemolysis	
H_t	haematocrit	
I	current	A
j	current density	A/m ²
L	angular momentum	Nms
m	mass	kg
n	rotational speed	rpm
N	number of	
NIH	normalised index of haemolysis	mg/dl
Nu	Nusselt-number	
p	pressure (1 mmHg = 133.32 Pa)	Pa
p	pole pair number	
p	momentum	Ns
P	power	W
Pr	Prandtl-number	
q	line force density	N/m

Nomenclature

Q	volumetric flow rate	m^3/s
r	radius	m
R	resistance	Ω
Ra	Rayleigh-number	
R_a	mean roughness index	μm
Re	Reynolds-number	
R_z	average maximum profile height	μm
s	experimental standard deviation	
S	source term	$(\cdot)/\text{s}$
t	time	s
t	thickness	m
T	torque	Nm
Ta	Taylor-number	
u	circumferential velocity	m/s
U	voltage	V
v	absolute velocity	m/s
V	volume	m^3
w	relative velocity	m/s
w	width	m
Y	specific work	m^2/s^2

Greek

α	tilting angle	$^\circ$
α	absolute flow angle	$^\circ$
β	tilting angle	$^\circ$
β	blade angle	$^\circ$
β	relative flow angle	$^\circ$
γ	slip coefficient	
δ_C	diameter number	
ϵ	blade blockage	
η	efficiency	
θ	rotor angle	rad
ϑ	temperature	K
Θ	magnetomotive force	A
μ	magnetic permeability	H/m
μ_{fl}	dynamic viscosity	$\text{Pa} \cdot \text{s}$
ν	kinematic viscosity	m^2/s
ξ	pressure loss coefficient	

ρ	density	kg/m ³
ρ_{cu}	specific resistance	Ωm
σ	mechanical stress	N/m ²
σ	standard deviation	
σ_C	specific speed	
τ	shear stress	N/m ²
ϕ	flow coefficient	
φ	angular coordinate	rad
ψ	residence time	s
ω	angular speed	rad/s

Coordinate Systems and Unit Vectors

\vec{n}	normal vector	
x, y, z	Cartesian coordinates	m
r, φ, z	polar coordinates	m
d, q, z	rotor oriented coordinates	m
$\delta x, \delta z, \delta z$	lateral rotor deflection	m
$\delta \alpha, \delta \beta$	rotor tilting	rad

Indices

$(\cdot)_a$	outside/outlet	
$(\cdot)_{abs}$	absolute	
$(\cdot)_{air}$	air	
$(\cdot)_{amb}$	ambient	
$(\cdot)_{ax}$	axial	
$(\cdot)_{bl}$	blade	
$(\cdot)_{bng}$	bearing	
$(\cdot)_{crit}$	critical	
$(\cdot)_{cu}$	copper	
$(\cdot)_S$	shroud	
$(\cdot)_{drv}$	drive	
$(\cdot)_{ec}$	eddy current	
$(\cdot)_{el}$	electric	
$(\cdot)_{exp}$	exposure	
$(\cdot)_{fl}$	fluid	

Nomenclature

(\cdot) _{free}	unbound carriers
(\cdot) _H	hub
(\cdot) _{hem}	haemolysis
(\cdot) _{hyd}	hydraulic
(\cdot) _{hys}	hysteresis
(\cdot) _i	inside/inlet
(\cdot) _{imp}	impeller
(\cdot) _L	Lorentz
(\cdot) _{leak}	leakage
(\cdot) _m	middle
(\cdot) _{in}	momentum
(\cdot) _m	meridional
(\cdot) _M	lateral surface
(\cdot) _{mag}	magnetic
(\cdot) _{max}	maximum
(\cdot) _{meas}	measurement
(\cdot) _{mech}	mechanical
(\cdot) _{mot}	motor
(\cdot) _{·,(n)}	n -th harmonic
(\cdot) _{net}	net
(\cdot) _{nom}	nominal
(\cdot) _P	pump
(\cdot) _{pf}	plasma-free
(\cdot) _{r,φ,z}	spacial direction in polar coordinates
(\cdot) _R	reluctance/friction
(\cdot) _{sim}	simulation
(\cdot) _{ref}	reference
(\cdot) _{rel}	relative
(\cdot) _{rot}	rotor
(\cdot) _{st}	shock
(\cdot) _{stat}	stator
(\cdot) _{sur}	surrounding
(\cdot) _{th}	theoretic/threshold/thermal
(\cdot) _{tot}	total
(\cdot) _{tooth}	stator tooth
(\cdot) _V	loss
(\cdot) _{vM}	von Mises
(\cdot) _{vol}	volumetric
(\cdot) _{Vol}	volute

$(\cdot)_W$	wall
$(\cdot)_{x,y,z}$	spacial direction in Cartesian coordinates
$(\cdot)_\infty$	limit value

Constants

g	gravity of earth	9.81 m/s^2
μ_0	vacuum permeability	$4\pi \cdot 10^{-7} \text{ N/A}^2$

Conventions and Operators

d	differential operator
∂	partial derivative
$\frac{D\Psi}{Dt}$	substantial derivative $\frac{D\Psi}{Dt} = \frac{\partial\Psi}{\partial t} + (\vec{u} \cdot \nabla)\Psi$
Δ	difference
$f(\dots)$	function of
∇	nabla / del
$\nabla\vec{u}$	gradient of a vector field \vec{u} : $\nabla\vec{u} = (\nabla \otimes \vec{u})^T$
\vec{x}	vector
\underline{x}	tensor
x_{ij}	tensor in component notation
\dot{x}	temporal derivative
\bar{x}	average
\hat{x}	peak value/amplitude
$ x $	absolute value
\otimes	dyadic product

Abbreviations

CFD	computational fluid dynamics
CPB	cardiopulmonary bypass
ECMO	extracorporeal membrane oxygenation
ECLS	extracorporeal life support
FEM	finite-element-method
ID	inner diameter
RBC	red blood cell

Nomenclature

VA	venous-arterial
VAD	ventricular assist device
VV	venous-venous

Contents

Abstract	v
Kurzfassung	vii
Nomenclature	ix
1 Introduction	1
1.1 Extracorporeal Life Support	1
1.2 Motivation	2
1.3 State of the Art	3
1.4 Objective of this Work	4
1.5 Structure of the Work	4
1.6 Publications	5
2 Bearingless Slice Motors	9
2.1 Structure and Topologies	9
2.2 Rotor Field	10
2.3 Torque and Force Generation	13
2.4 Loss Models	20
2.5 Topology Comparison for Pump Applications	22
2.6 Summary	32
3 The Bearingless Centrifugal Pump	33
3.1 Structure and Components	33
3.2 Operating Principle of the Centrifugal Pump	36
3.3 Losses	41
3.4 Hydraulic Forces	45
4 Blood Damage	51
4.1 Blood as Fluid	51
4.2 Haemolysis	54
4.3 CFD Simulations of Haemolysis	58
5 Systematics	67
5.1 Centrifugal Pump	67
5.2 Hydraulic Experiments	73
5.3 In Vitro Experiments	77
5.4 CFD Implementation	84

6	Influence of the Surface on Haemolysis	95
6.1	Influence of Surface Quality	96
6.2	Dependence on the Shear Rate	99
6.3	Dependence on the Static Pressure	99
6.4	Influence of the Surface Quality in Pumping Applications	101
6.5	Summary	102
7	Flow Conditions	105
7.1	Overview	105
7.2	Separation into Control Volumes	109
7.3	Blade Channel	109
7.4	Radial Gap	111
7.5	Bottom Volume	112
7.6	Front Shroud Gap	113
7.7	Washout Hole	113
8	Haemolysis in the Bearingless Pump	117
8.1	Overview of the In Vitro Experiments	117
8.2	Cell Damage Distribution	119
8.3	Influence of the Geometry	121
8.4	Summary	129
9	Benchmark Tests	131
9.1	Comparison Pumps	131
9.2	Test Conditions	132
9.3	Haemolysis Comparison	132
10	Summary and Outlook	135
10.1	Summary	135
10.2	Outlook	137
	Appendices	139
A	Forces in Magnetic Fields	141
A.1	The Macroscopic Maxwell's Equations	141
A.2	Boundary Conditions	142
A.3	Forces in the Magnetic Field	143
	Bibliography	147

1

Introduction

1.1 Extracorporeal Life Support

Extracorporeal life support is used during operations, as a support for failing organs and as a bridge to transplantation. The patient's blood circulation and, in some cases, other organ functions are supported or replaced extracorporeally.

During heart surgery, the so-called cardiopulmonary bypass (CPB) method is used to take over the function of the heart and lungs. Blood is pumped with blood pumps through an extracorporeal circulation. In this system, filtering, temperature control and gas exchange take place with the aid of an oxygenator.

In the case of an acute respiratory disease, a modified form of CPB is used: the so-called extracorporeal membrane oxygenation (ECMO/ECLS). These two methods differ concerning the pump function, mainly in the flow rate. Whereas during CPB, the total volume flow of approx. 5l/min has to be delivered by the pump, during ECMO, only about 80% thereof needs to be supported. The remaining blood flow is still maintained by the heart to prevent thrombus formation. The reduced strain on the diseased organs enables faster regeneration. The amount of volume flow taken over by the pump depends on the degree of damage of the organs to be relieved.

If ECMO applications require both heart and lung functions to be taken over, venous blood is drawn from the body. It is filtered outside the body, oxygenated and tempered before being reinjected arterially. This is referred to as the venous-arterial ECMO (VA ECMO). If only the lung function has to be taken over, the blood is both taken from

and returned to the vein (VV ECMO). The heart's function continues normally.

Another application is for dialysis, which is employed in case of kidney failure. Blood purification also takes place in an extracorporeal circuit using a membrane [1]. The continuous delivery takes place either via a peristaltic pump or a centrifugal pump specially designed for this application.

1.2 Motivation

In Europe, about 3.9 million deaths per year are caused by cardiovascular diseases. In about twelve countries, they are the main cause of death for men and in two of those also for women [2]. Since 1919, it has also been the leading cause of death in the statistics of the United States (over 800,000 deaths in 2014) [3]. Implantable ventricular assist devices (VAD) or heart transplants are available today as the last treatment option for severe cardiovascular diseases. In 2017, about 2100 such VADs were implanted [4].

Particularly in the field of implantable VADs, great efforts are being made to improve the products. The magnetically suspended HeartMate 3 (Abbott) received the CE marking in 2015 and has since been the most advanced VAD pump on the market [5]. Due to the long service life of such VAD systems, the product costs are secondary, which enables the use of advanced materials and technologies. Such technologies are rarely used for extracorporeal systems exactly because of their high costs, although such systems are used in the majority of cardiovascular treatments. Especially after the influenza A (H1N1) pandemic in 2009, ECLS therapies in adults have increased significantly [6]. According to the extracorporeal life support organization (ELSO), in 2018 alone, about 2923 respiratory and 3433 cardiac therapies were registered. The survival rate was 62% and 45%, respectively [7]. In addition, there were 2348 applications in newborns and children, with a survival rate of approximately 62%, and other unregistered patients. Complications occurred in about 3-4% of the cases due to elevated hemoglobin levels (> 50 mg/dl). Only 55% of lung and 32% of heart patients survived these complications. Both the occurrence of bleeding and an increased risk of thrombosis are among the main complications in ECMO applications [8]. It is not known which factors in the interaction between the patient and the circulatory system are responsible for such compli-

cations [9]. A potential problem is the direct damage of blood components, especially blood cells. As a result of mechanical transportation, the membranes of the blood cells are impaired. This is followed by a limitation of the functionality up to the destruction of the cell. The systemic stimulation of blood coagulation in the vascular system leads to excessive consumption of coagulation factors, resulting in a severe coagulopathy (DIC). This may be a possible cause of bleeding and excessive thrombus formation.

This work intends to contribute to the reduction of blood cell damage inflicted by pumps in mechanical circulatory support, in order to increase the success rate of above described treatments.

1.3 State of the Art

Until 2009, mainly peristaltic pumps were used for ECLS applications [6]. These pumps are still widely used due to their inexpensive components. An essential disadvantage is difficult handling. In particular, the risk of a tube rupture is high, as they displace a constant volume regardless of the backpressure.

In the meantime, peristaltic pumps have been almost completely replaced by centrifugal pumps. Due to their flat pump characteristics, the outlet pressure is limited, and the risk of tube rupture is low. However, the risk of haemolysis and the resulting organ failure appear to be increased in newborns and children [10, 11].

The first centrifugal pump for ECLS applications was tested as early as 1975. The Bio Medicus Vortex Pump (currently Medtronic BPX-80) was launched in the same year [6]. This pump is equipped with a mechanical pivot bearing. A magnetic torque coupling drives the pump through the housing bottom. The heat generated in the bearing is probably the most significant source of cell damage [12].

Further pumps with mechanical bearings followed in subsequent years. Widely used examples are the delstream DP3 (Medos), Rota-Flow RF-32 (Maquet), and revOlution (Sorin Group, LivaNova). In some cases, these pumps significantly exceed the cell compatibility of the BPX-80.

The first fully magnetically suspended pump (CentriMag) was clinically tested in 2004 [13]. Drive and bearings of this pump rely on the concept of the bearingless slice motor, which is presented in more detail in Chapter 2. Thanks to the low-shear and stagnation-free design, this

pump causes only minor damage to the blood cells. Due to the lack of mechanical abrasion, it is also suitable for long-term use. Promising results were achieved in several clinical trials [14–18]. However, a reduction of haemolysis compared to the mechanically supported RotaFlow pump could not be demonstrated [19,20].

1.4 Objective of this Work

The present work aims to identify the causes of cell damage in bearingless pumps. Simulations and in vitro experiments are used to locate critical points in the pump and identify suitable measures to reduce cell damage.

By choosing a small rotor diameter, both the production costs of the pump head and the priming volume are to be reduced compared to existing systems. At the same time, cell compatibility is to be maintained or even improved.

1.5 Structure of the Work

Chapter 2 describes the function of the bearingless slice motor. Two motor topologies are presented, namely the slotless slice motor and the grooved motor in temple design. This is followed by a description of the force and torque generation as well as an overview of the relevant loss mechanisms. By using the Cordier diagram and a simplified thermal model of the pump, the two topologies are compared for their application as medical pumps.

Chapter 3 describes the design and function of the bearingless centrifugal pump in detail. The geometric dimensions of the impeller are linked to the characteristic curve of the pump with the help of the law of conservation of momentum. Finally, the hydraulic forces acting on the impeller and the hydraulic loss mechanisms are described.

Starting with the composition and properties of human blood, Chapter 4 lays the necessary foundations for understanding haemolysis in blood pumps. The most critical factors influencing cell damage are highlighted. In addition, mathematical models for estimation of cell damage by use of CFD simulations are presented.

The procedures applied to investigate cell damage are presented in Chapter 5. In addition to the design of the prototypes, the test benches

used for in vitro investigations are presented. The implementation of the damage model in a CFD simulation environment is also shown.

Chapter 6 examines the influence of surface quality on haemolysis in the centrifugal pump. The dependence of cell damage on the surface quality, shear rate, and static pressure is shown using a simplified test bench.

CFD simulations are used to visualize the flow conditions within the pump in Chapter 7. The analysis takes place with the geometries of one of the prototypes. The focus is mainly on the flow conditions in the sidewall gaps and the shear forces that occur.

Chapter 8 presents the results from the in vitro experiments. CFD simulations are used to illustrate the effects of the individual geometric variations.

Chapter 9 compares the prototypes with market-leading products in the field of extracorporeal cardiac support. Finally, the most relevant results are summarized in Chapter 10.

1.6 Publications

Findings in the context of this dissertation that have been published in journals and presented at conferences, along with the student projects that have been supervised, are listed below.

Journals

- ▶ P. Puentener, M. Schuck, D. Steinert, T. Nussbaumer and J. W. Kolar, "A 150000 r/min Bearingless Slice Motor," *IEEE/ASME Trans. on Mechatronics*, vol. 23, no. 6, pp. 2963–2967, December 2018.
- ▶ M. Schuck, P. Puentener, T. Holenstein, and J. W. Kolar, "Scaling and Design of Miniature High-Speed Bearingless Slice Motors," *Elektrotechnik und Informationstechnik*, vol. 136, no. 2, pp. 112–119, April 2019.
- ▶ P. Puentener, M. Schuck, and J. W. Kolar, "The Influence of Impeller Geometries on Haemolysis in Bearingless Centrifugal Pumps," *IEEE Open Journal of Engineering in Medicine and Biology*, under review.

- ▶ P. Puentener, M. Schuck, and J. W. Kolar, "CFD Assisted Evaluation of In Vitro Experiments on Bearingless Blood Pumps," *IEEE Trans. on Biomedical Engineering*, under review.

Conference Publications

- ▶ P. Puentener, F. Hoffmann, D. Menzi, D. Steinert, and J. W. Kolar, "Homopolar Bearingless Slice Motor in Temple Design," *IEEE International Electric Machines and Drives Conference (IEMDC)*, Miami (FL), USA, May 2017.
- ▶ P. Puentener, M. Schuck, D. Steinert, and J. W. Kolar, "Comparison of Bearingless Slice Motor Topologies for Pump Applications," *IEEE International Electric Machines and Drives Conference (IEMDC)*, San Diego (CA), USA, May 2019.

Supervised Student Theses

- ▶ F. Hoffmann, D. Menzi, "Lagerlose Motoren mit hoher Lagersteifigkeit," LEM 1630, *Semester Thesis*, Autumn 2016.
- ▶ A. da Silva Fernandes, "A High-Speed Bearingless Electrical Motor," LEM 1633, *Master Thesis*, Autumn 2016.
- ▶ M. Sanchez, P. Seiler, "Charakterisierung einer magnetgelagerten Pumpe," LEM 1711, *Group Thesis*, Spring 2017.
- ▶ T. Felder, "Entwicklung eines lagerlosen Rotationsviskosimeter," LEM 1715, *Semester Thesis*, Spring 2017.
- ▶ N. Schlegel, "Experimental Setup for Analyzing Cell Damage Related to Surface Roughness," LEM 1720, *Masterarbeit*, Autumn 2017.
- ▶ S. Wyss, "Entwicklung einer auf Hallsensoren basierenden Positionssensorik für nuten- und lagerlose Motoren," LEM 1726, *Semester Thesis*, Autumn 2017.
- ▶ T. Lehner, "Investigation of the Influence of Impeller Geometry in Bearingless Pumps on Cell Damage in Biotechnological Fluids," LEM 1739, *Semester Thesis*, Autumn 2017.

- ▶ C. Burkard, "CFD Simulation of a Bearingless Pump," LEM 1822, *Semester Thesis*, Autumn 2018.
- ▶ T. Ackermann, M. Strässle, "Entwicklung einer mechatronischen Wafer-Halterung für magnetisch gelagerte Motoren," LEM 1826, *Semester Thesis*, Autumn 2018.
- ▶ B. Vukovic, "Design and Optimization of a Solenoid Pinch Valve," LEM 1833, *Semester Thesis*, Autumn 2018.
- ▶ M. Röthlisberger, "Single-Beam Acoustic Manipulation and Transport of Levitated Objects," LEM 1906, *Master Thesis*, Autumn 2019.
- ▶ S. Trossarello, "Feasibility Studies for High-Power Bearingless Pumps," LEM 1908, *Master Thesis*, Autumn 2019.
- ▶ F. Inderbitzin, "Untersuchung der Druckabhängigkeit der Zellschädigung in Medizinalpumpen," LEM 1909, *Semester Thesis*, Spring 2019.
- ▶ L. Kulmer, A. Mukherjee, "Entwicklung einer iOS App zur Bedienung lagerloser Pumpen," LEM 1915, *Group Thesis*, Spring 2019.
- ▶ N. Kleynhans, "Design and Implementation of an Artificial Intelligence Controller for Adaptive Control of Pump Speed and Flow Rate," LEM 1916, *Semester Thesis*, Spring 2019.
- ▶ P. Alff, "Drehmomentoptimierung eines lagerlosen Mixers," LEM 1922, *Semester Thesis*, Spring 2019.

2

Bearingless Slice Motors

The bearingless slice motor is an electric motor with a magnetically levitated rotor. The rotor consists of a diametrically magnetized ring magnet, which generates an almost sinusoidal field distribution in the air gap. In contrast to conventional magnetically suspended machines, the bearing forces and torque are generated in the same iron circuit. This enables a compact design.

The term slice motor indicates that the rotor diameter is larger than its height. This results in three passively stable degrees of freedom. The causes and the exact relationships are explained in detail in Section 2.3.6.

Six coils wound around the stator iron are available for bearing and drive. With suitable current supply, both bearing forces and a drive torque can be generated. A detailed description of the force and torque formation is given in Section 2.3.

Sections 2.4 and 2.5 summarize the motor losses and assess two motor topologies for pump applications.

2.1 Structure and Topologies

Since the development of the first bearingless slice motor [21], many different bearing concepts have been developed. Most of them rely on the principle of the homopolar bearing or use a reluctance rotor [22–25]. However, the focus of this work is on motors with heteropolar bearings. The permanently magnetized rotor biases the magnetic field to achieve a high torque density. The rotor is diametrically magnetized and radially suspended in the stator.

The available motor topologies can be roughly divided into two categories. The slotless motor, depicted in Fig. 2.1(a), consists of a single stator ring. The bearing and drive coils are wound toroidally around the stator. Compared to helical or concentrated windings, this winding arrangement achieves higher inductances [26, 27]. The rotor field penetrates the coils in the air gap. The operating principle of the motor is, therefore, primarily based on Lorentz forces.

In contrast, Fig. 2.1(b) depicts the slotted motor in temple design. The stator iron consists of six L-shaped stator claws. The magnetic flux path is closed on the underside through a ring-shaped back iron. The coils are wound around the leg of the stator claws and can increase or decrease the flux density in the respective tooth. The force and torque are generated mainly due to reluctance forces.

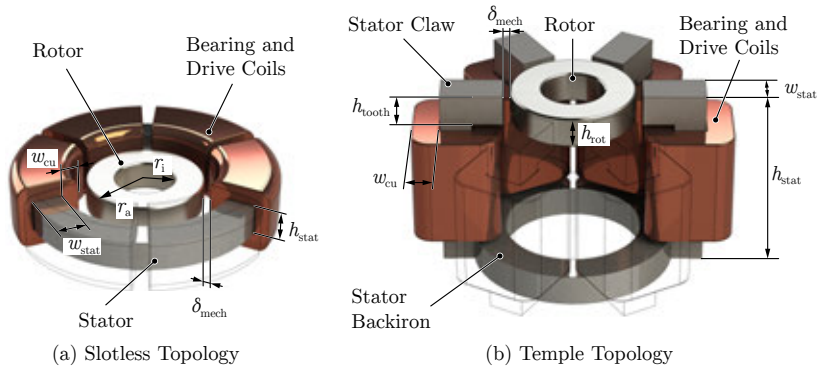


Figure 2.1: Rendered representations of the motor topologies investigated and the terminology used.

2.2 Rotor Field

The air gap field caused by the rotor magnet can be assumed to be approximately sinusoidal. Both radial B_r as well as tangential field components B_φ occur. The axial field component is negligibly small in the equilibrium position of the rotor and can be ignored when calculating the generation of active torque and bearing force.

The magnetic field in the air gap can be expressed as

$$\vec{B}_{\text{rot}}(\varphi, \theta) \approx \hat{B}_r \cos(p_{\text{rot}}(\varphi - \theta))\vec{e}_r + \hat{B}_\varphi \sin(p_{\text{rot}}(\varphi - \theta))\vec{e}_\varphi, \quad (2.1)$$

where θ is the mechanical rotor angle, p_{rot} is the number of pole pairs of the rotor, and φ is the angular coordinate.

The terminology and coordinates used in the following can be found in the top views in Fig. 2.2. A magnetically equivalent, two-dimensional arrangement of the stator is used for the temple motor.

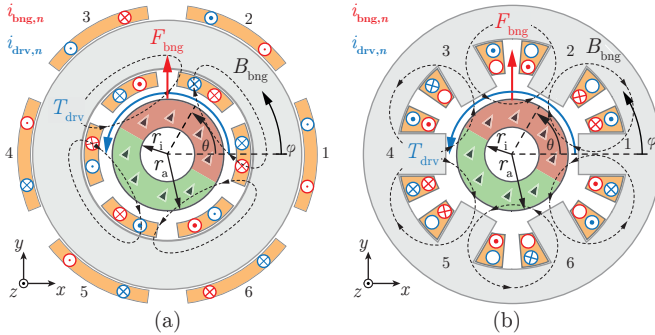


Figure 2.2: Top view of the slotless (a) and the slotted (b) bearingless slice motor. An equivalent two-dimensional representation was used for the slotted motor. In the coils, the bearing (red) and drive currents (blue) are marked qualitatively. The field lines caused by the bearing current are also indicated.

2.2.1 Stator Harmonics

In the case of a slotted stator with N stator claws, the rotor field is distorted by the angle-dependent reluctance. Near the faces of the teeth, the radial magnetic field is compressed, whereas it is slightly weakened between the stator teeth. Similarly, the tangential field component is strengthened in the areas of the teeth flanks.

The resulting radial air gap field can thus be approximated by superimposing the rotor field with a rectangular function with pulse width

$$D = \frac{N \Delta \varphi_{\text{tooth}}}{2\pi},$$

$$B_r = \hat{B}_r \cos(p_{\text{rot}}(\varphi - \theta)) \cdot \left(k_1 + k_2 \cdot \text{rect}\left(\varphi - \frac{D}{2}, D\right) \right), \quad (2.2)$$

$$\text{rect}(\varphi, D) = \text{sgn} \left(\frac{\varphi N}{2\pi} - \left\lfloor \frac{\varphi N}{2\pi} \right\rfloor - D \right). \quad (2.3)$$

Here k_1 stands for the attenuation of the fundamental harmonic compared to an unslotted stator.

The rectangle function can be represented using the Fourier series

$$\text{rect}\left(\varphi - \frac{D}{2}, D\right) = \sum_{n=1}^{\infty} \frac{N}{n\pi} \sin\left(n \frac{\Delta \varphi_{\text{tooth}}}{2}\right) \cos(nN\varphi). \quad (2.4)$$

The n -th harmonic of the radial field $B_{r,(n)}$ can thus be described as

$$B_{r,(n)} = \hat{B}_{r,(n)} \cos((p_{\text{rot}} \pm nN)\varphi - \theta_{\text{el}}), \quad (2.5)$$

$$\hat{B}_{r,(n)} = \hat{B}_r \frac{k_2 N}{2\pi n} \sin\left(n \frac{\Delta \varphi_{\text{tooth}}}{2}\right), \quad (2.6)$$

where $\theta_{\text{el}} = p_{\text{rot}}\theta$.

Fig. 2.3 demonstrates this approximation for $N = 6$ and $\Delta \varphi_{\text{tooth}} = 30^\circ$.

The harmonics caused by the stator shape show a higher spatial frequency compared to the slotless variant, but rotate with the same frequency as the fundamental harmonic.

To compare the two topologies, Fig. 2.4 illustrates the flux density in the center of the air gap for a slotless (a) and a slotted (b) motor, with the same rotor dimensions and air gap lengths. Both fields are illustrated for a rotor angle of $\theta = 0$.

In the case of a slotted temple motor with six rectangular claws and a rotor pole pair number $p_{\text{rot}} = 1$, the flux density in the air gap exhibits a fifth and seventh harmonic. The harmonics of the tangential flux component are more pronounced.

Due to the uniform reluctance in the air gap, the stator of the slotless motor does not cause harmonics. The tangential component is also less pronounced with $\hat{B}_\varphi \approx \hat{B}_r/12$ than with a slotted stator.

Furthermore, it can be seen that the maximum flux density of the slotted motor is higher because the field lines condense towards the stator tooth.

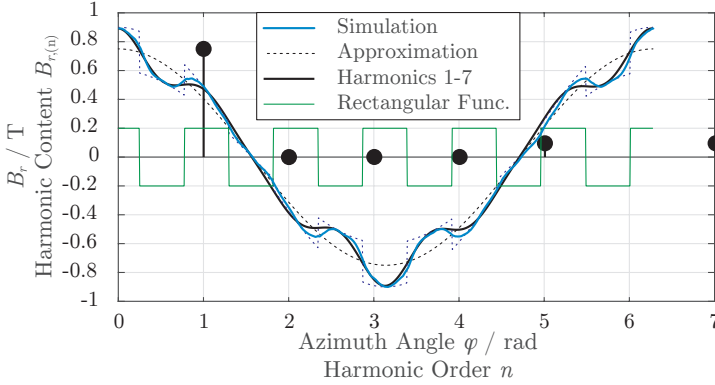


Figure 2.3: Approximation of the radial field B_r by superimposing the fundamental harmonics with a rectangular function. A comparison of the first seven harmonics with simulation results shows good agreement.

2.3 Torque and Force Generation

To explain the operating principle of the bearingless motor, it is assumed that the used materials exhibit linear, isotropic behaviour during operation. As described in Appendix A.3.11, the forces in the motor can be divided into Lorentz \vec{f}_L and reluctance forces \vec{f}_R . Magnetostriction and time-dependent effects are neglected.

2.3.1 Force Density

On the macroscopic level, the force density can thus be described as

$$\vec{f}_V = \vec{j}_{\text{free}} \times \vec{B} - \frac{1}{2} \vec{H}^2 \nabla \mu = \vec{f}_L + \vec{f}_R. \quad (2.7)$$

Furthermore, it can be assumed that $\mu_{\text{Fe}} \gg \mu_{\text{air}} \approx \mu_0$ applies. The magnetic field lines, therefore, enter the iron surface of the stator approximately perpendicularly. The reluctance force on the stator surface can thus be calculated in a simplified form as

$$\vec{f}_{R,\text{stat}} = \frac{1}{2\mu_0} B_n^2 \vec{n}_1 = \frac{1}{2\mu_0} B^2 \vec{n}_1, \quad (2.8)$$

where \vec{n}_1 stands for the normal vector on the surface.

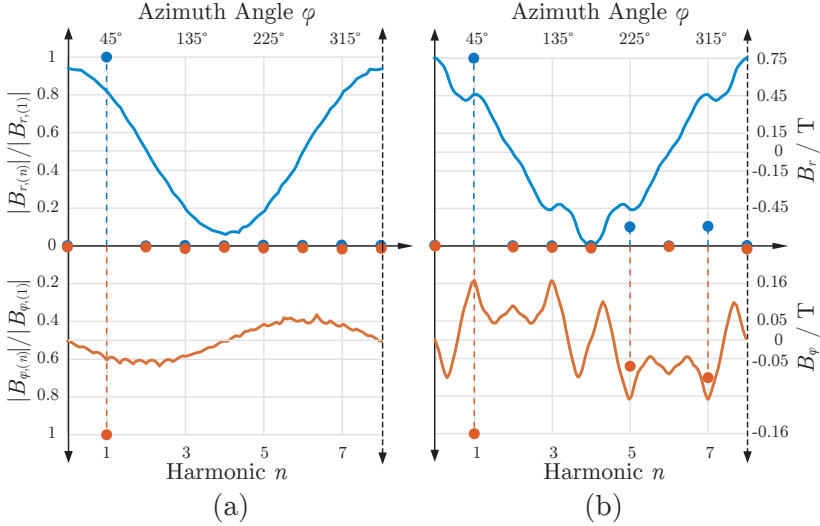


Figure 2.4: Field distribution in the slotless (a) and slotted (b) machine. The upper part depicts the radial field component B_r together with the frequency components along the angular coordinate φ in the middle of the air gap. In the lower part, the same applies for the tangential flux density B_φ .

The reluctance force thus always acts as a tensile force perpendicular to the surface. The Lorentz force acts only on the current-carrying conductors in the machine.

2.3.2 Action of Force

In order to describe the force and torque generation in the bearingless machine, the forces acting on the stator are determined. According to Newton's third law, these must be equal to the forces acting on the rotor in opposite direction.

$$-\vec{F}_{\text{rot}} = \vec{F}_{\text{stat}} = \int_{V_{\text{cu}}} \vec{j}_{\text{free}} \times \vec{B} \, dV + \int_{A_{\text{stat}}} \frac{B^2}{2\mu_0} \, d\vec{A}, \quad (2.9)$$

$$-\vec{T}_{\text{rot}} = \vec{T}_{\text{stat}} = \int_{V_{\text{cu}}} \vec{r} \times (\vec{j}_{\text{free}} \times \vec{B}) \, dV + \int_{A_{\text{stat}}} \frac{B^2}{2\mu_0} (\vec{r} \times \vec{n}) \, dA \quad (2.10)$$

The two considered topologies differ significantly in the generation of torques and forces. For the slotted motor, the current-carrying windings are located in almost field-free areas. All forces are thus attributable to reluctance forces. Since these forces always act perpendicular on the stator surface, the bearing forces are generated on the teeth faces and flanks, while the torque can only be generated on the teeth flanks. For the slotless motor, the bearing forces are generated by radially acting reluctance forces and tangentially acting Lorentz forces. The torque can only be generated by Lorentz forces. In contrast to the slotted machine, the torque-forming forces in the slotless motor thus act directly on the conductors. Therefore, they must be sufficiently fixed to prevent twisting.

2.3.3 Equivalent Modeling

Although the force generation of the two motor topologies is quite different, the operating principle can be described equally. For this purpose, the reluctance forces acting on the teeth flanks of the slotted motor are replaced by Lorentz forces acting on current sheets imagined to be located in the air gap. The resulting forces are equal in magnitude and direction [28, 29].

For the sake of simplicity, the following description of the operating principle is based on the slotless motor. Further considerations can be found in [30].

Linear Current Density

The copper area A_{cu} from Fig. 2.5 is considered in the form of a ring segment with inner and outer radius $r_{\text{cu,i}}$ and $r_{\text{cu,a}}$, respectively. This surface has a tangential expansion of $\Delta\varphi$ and a constant current density $\vec{j} = j\vec{e}_z$.

Correspondingly, the generated magnetomotive force is

$$\Theta = \frac{r_{\text{cu,a}}^2 - r_{\text{cu,i}}^2}{2} \Delta\varphi j. \quad (2.11)$$

The current density

$$\vec{A} = \frac{\Theta}{\Delta\varphi r} \vec{e}_z \quad (2.12)$$

is defined as the line current density on the radius r . The mean radius of the copper winding $r_{\text{cu,m}} = \frac{1}{2}(r_{\text{cu,i}} + r_{\text{cu,a}})$ is usually used.

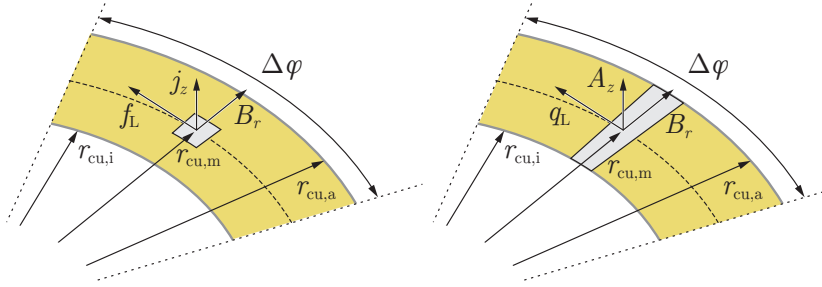


Figure 2.5: (a) representation of the current density j_z , the radial field B_r , and the resulting Lorentz force density f_L . (b) representation of the linear current density A_z , radial field B_r , and the resulting line force density q_L .

It follows

$$A_z = \frac{\Theta}{\Delta\varphi r_{cu,m}} = \frac{r_{cu,a}^2 - r_{cu,i}^2}{2r_{cu,m}} j. \quad (2.13)$$

2.3.4 Torque Generation

The drive of the bearingless disc motor is identical to that of the permanent magnet synchronous machine. The air gap field $\vec{B}_{rot}(\varphi, \theta)$ generated by the rotor is superimposed by a stator field with the same number of pole pairs p_{drv} . For this purpose, the current density $A_z(\varphi, \theta)$ in the drive coils is chosen in such a way that the basic component $A_{z,(1)}(\varphi, \theta)$ shows the desired amplitude and phase.

Assuming that the flux density along the stator height h_{stat} and along the radial extension of the conductor is constant, this leads to a distribution of the Lorentz line force density \vec{q}_L corresponding to

$$\vec{q}_L = q_r \vec{e}_r + q_\varphi \vec{e}_\varphi = h_{stat} \vec{A} \times \vec{B} = h_{stat} A_z(\varphi, \theta) \cdot (B_r \vec{e}_\varphi - B_\varphi \vec{e}_r). \quad (2.14)$$

The resulting torque, generated by the Lorentz forces, can be obtained by integration along the mean conductor radius $r_{cu,m}$,

$$T_{rot,z} = - \int_0^{2\pi} (\vec{r} \times \vec{q}_L) r d\varphi = -r_{cu,m}^2 \int_0^{2\pi} q_\varphi d\varphi. \quad (2.15)$$

Here, the force components on the cover surfaces were neglected.

The tangential portion of the line force density,

$$q_\varphi = h_{stat} A_z(\varphi, \theta) B_r(\varphi, \theta), \quad (2.16)$$

only depends on the radial rotor field and current.

If the fundamental harmonic of the drive current is chosen to be

$$A_{\text{drv},(1)}(\varphi) = -\hat{A}_{\text{drv}} \sin(p_{\text{drv}}\varphi - \theta_{\text{el}} + \varphi_{\text{drv}}) \quad (2.17)$$

the corresponding torque is

$$T_z = h_{\text{stat}} r_{\text{cu,m}}^2 \pi \hat{B}_r \hat{A}_{\text{drv}} \sin(\varphi_{\text{drv}}), \quad (2.18)$$

if $p_{\text{rot}} = p_{\text{drv}}$.

Both the amplitude \hat{A}_{drv} and the drive angle φ_{drv} can be used to control the torque. Since the motors under consideration show hardly different inductances in d - and q -directions, the drive angle can be fixed at $\varphi_{\text{drv}} = \pi/2$ and the q -current I_q is controlled. This minimizes the ohmic losses in the drive coils (MTPA control).

2.3.5 Generation of Radial Bearing Forces

The bearing forces in the slotless motor are generated by both Lorentz and Maxwell forces. In the following, first the force component caused by the Lorentz force will be described, and then the component caused by the reluctance force.

Lorentz Forces

Analogous to the calculation of the torque, the current flow in the bearing coils results in a Lorentz force density \vec{q}_L . It can be integrated along the stator circumference in order to obtain the resulting Lorentz force acting on the rotor. The following applies:

$$\vec{F}_{\text{rot},xy} = - \int_0^{2\pi} \vec{q}_L r_{\text{cu,m}} d\varphi = - \int_0^{2\pi} r_{\text{cu,m}} \mathbf{R} \cdot \begin{pmatrix} q_r \\ q_\varphi \end{pmatrix} d\varphi \quad (2.19)$$

where

$$\mathbf{R} = \begin{pmatrix} \cos(\varphi) & -\sin(\varphi) \\ \sin(\varphi) & \cos(\varphi) \end{pmatrix} \quad (2.20)$$

represents the transformation from the polar to the Cartesian coordinate system.

If a current density A_{bng} is assigned to the bearing coils, whose basic harmonic

$$A_{\text{bng},(1)}(\theta) = \hat{A}_{\text{bng}} \sin(p_{\text{bng}}\varphi - \theta_{\text{el}} - \varphi_{\text{bng}}) \quad (2.21)$$

shows a pole pair number $p_{\text{bng}} = p_{\text{rot}} + 1$, the resulting force is

$$\vec{F}_{xy} = \frac{\hat{A}_{\text{bng}}(\hat{B}_r + \hat{B}_\varphi)h_{\text{rot}}r_a\pi}{2} \begin{pmatrix} \cos(\varphi_{\text{bng}}) \\ \sin(\varphi_{\text{bng}}) \end{pmatrix}. \quad (2.22)$$

Maxwell Forces

In addition to the Lorentz forces described above, Maxwell forces also act in the bearingless motors. For the slotless motor, the stator magnetic field lags the current by 90° electrically. Since the field lines on the inside of the stator are almost perpendicular to the iron surface, the stator flux density is simplified to

$$\vec{B}_{\text{stat}} = \hat{B}_{\text{stat}} \cos(p_{\text{bng}}\varphi - \theta_{\text{el}} - \varphi_{\text{bng}})\vec{e}_r. \quad (2.23)$$

The resulting Maxwell force is given by

$$\vec{F}_{\text{rot},xy} = h_{\text{rot}}r_{i,\text{stat}} \int_0^{2\pi} \mathbf{R} \cdot \frac{B_{\text{tot}}^2}{2\mu_0} \vec{e}_r \quad (2.24)$$

with $B_{\text{tot}} = B_{\text{stat},r} + B_{\text{rot},r}$.

With a pole pair number of $p_{\text{bng}} = p_{\text{rot}} + 1$ a radial force is given by

$$\vec{F}_{\text{rot},xy} = \frac{h_{\text{rot}}r_{i,\text{stat}}\pi}{2\mu_0} \hat{B}_{\text{rot},r} \hat{B}_{\text{stat},r} \begin{pmatrix} \cos(\varphi_{\text{bng}}) \\ \sin(\varphi_{\text{bng}}) \end{pmatrix}. \quad (2.25)$$

The Maxwell forces thus add up to the Lorentz forces and increase the radial force. This applies to $p_{\text{stat}} = p_{\text{rot}} + 1$. Results for other pole pair numbers are discussed in [30].

2.3.6 Passive Properties

The passive properties of the motors are purely due to reluctance forces. The deflection of the rotor from its equilibrium position changes the field distribution and thus the energy stored in the magnetic field,

$$E_{\text{mag}} = \frac{1}{2} \int_{\mathbf{V}} BH \, dV. \quad (2.26)$$

Since the reluctance force acts perpendicularly on the stator surface, it becomes clear that different surfaces of the stator are responsible for

the force generation at the different deflections of the rotor. The radial forces always act on the face sides of the stator, while axial forces act on the upper and lower sides. The restoring torques around the d - and q -axis are formed both on face sides as well as on the upper and lower sides of the stator.

For the arrangement of a diametrically magnetized rotor, which is concentrically planarly centred in a stator (coaxial coupling), the axial degree of freedom is passively stable. In contrast, the radial direction is always unstable for such an arrangement [31]. A magnetic bearing based entirely on permanent magnets is not possible, according to the Earnshaw theorem [32].

For disc-shaped bearingless motors ($h_{\text{rot}} < r_{\text{rot}}$), in addition to the axial deflection δz (see Fig. 2.6(a)), the tilting about the d - and q -axis, $\delta\alpha$ and $\delta\beta$, respectively, is also passively stable. This can be seen qualitatively in Fig. 2.6(b). The reluctance increases by tilting the rotor around the q -axis. This applies as long as the reluctance forces acting on the upper and lower sides of the stator change more than the radial forces.

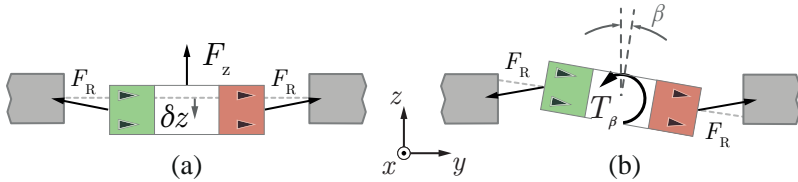


Figure 2.6: The generation of passive bearing forces is based on the increase of the reluctance due to the air gap change. Axial reluctance force F_z (a) and restoring tilting torque T_β (b).

Passive Bearing Stiffness

A bearing stiffness can be introduced to describe the bearing, analogous to a mechanical spring. For this purpose, each degree of freedom is assigned a corresponding stiffness around the equilibrium position,

$$k_x = -\frac{dF_x}{dx}, \quad k_y = -\frac{dF_y}{dy}, \quad k_z = -\frac{dF_z}{dz}, \quad (2.27)$$

$$k_\alpha = -\frac{dT_\alpha}{d\alpha}, \quad k_\beta = -\frac{dT_\beta}{d\beta}. \quad (2.28)$$

Here, F_i and T_i represent the forces in the direction i and the torque around the axis i , respectively.

Degrees of freedom, whose passive bearing stiffness is positive, have a stabilizing effect.

2.4 Loss Models

The losses in the bearingless motor consist primarily of ohmic copper losses and iron losses. The eddy current losses induced in the rotor shell due to the current ripples and the stator harmonics are subsequently neglected. They only become important at high speeds, or for large current ripples [30]. Since the rotation speeds required for pumping applications are relatively low, the eddy current losses contribution is negligible. To reduce eddy-current losses, only thin laminated stator irons are considered and edd current losses caused by the drive field are assumed to be negligible [33].

Skin and proximity effects are also not considered. Proximity effects can have a particularly large influence on the losses in the slotless motor, however, can be almost eliminated by using stranded wire [34].

2.4.1 Copper Losses

Ohmic losses occur in the current-carrying windings of the stator, which can be calculated according to

$$P_{\text{cu}} = RI^2 = \rho_{\text{cu}} V_{\text{cu}} j_{\text{rms}}^2. \quad (2.29)$$

Here, ρ_{cu} is the specific resistance of copper, V_{cu} the copper volume, and j_{rms} the RMS value of the current density.

For later analysis of the pump, it makes sense to assign the losses separately to the bearing and drive windings. The following applies:

$$P_{\text{cu,bng}} = \sum_{i=1}^{N_{\text{bng}}} \rho_{\text{cu}} V_{\text{cu,bng}} j_{\text{rms,bng},i}^2, \quad (2.30)$$

$$P_{\text{cu,drv}} = \sum_{i=1}^{N_{\text{drv}}} \rho_{\text{cu}} V_{\text{cu,drv}} j_{\text{rms,drv},i}^2, \quad (2.31)$$

where N_{bng} and N_{drv} represent the number of bearing and drive coils, respectively.

For the copper resistance, it is necessary to consider the linear temperature coefficient α according to equation (2.32) and to estimate the temperature ϑ , or to determine the temperature by simulations or measurements,

$$\rho_{\text{cu}} = \rho_{\text{cu},\vartheta_0}(1 + \alpha(\vartheta - \vartheta_0)). \quad (2.32)$$

At the reference temperature $\vartheta_0 = 20^\circ\text{C}$, a value of $\alpha \approx 3.9 \cdot 10^{-3} \text{ 1/K}$ and $\rho_{\text{cu},\vartheta_0} \approx 16.8 \text{ n}\Omega\text{m}$ can be assumed for copper [35].

2.4.2 Iron Losses

The iron losses occur in the stator and are caused by the rotating magnetic field, generated mainly by the rotor. The induction change causes both eddy current losses P_{ec} and hysteresis losses P_{hys} .

In the following, the Steinmetz formula

$$P_{\text{stat}} = P_{\text{hys}} + P_{\text{ec}} = C \int_{V_{\text{stat}}} f^\alpha \hat{B}^\beta dV, \quad (2.33)$$

is used to determine the iron losses. The Steinmetz parameters C , α and β can be determined by robustly minimizing the error squares using loss measurements from the data sheet. The resulting parameters for electrical steel M330-35A are listed in Tab. 2.1.

Table 2.1: Steinmetz parameters for electrical sheet M330-35 [36].

Electrical Sheet M330-35A	
C	24.54 W/(m ³ Hz ^{α} T ^{β})
α	1.5
β	1.85

While it is possible to find analytical solutions for the stator losses in the slotless motor [37], the conditions with the slotted temple motor are too complex. Therefore, in the following, FEM simulations are used to obtain the loss distribution.

In order to show the differences in the stator losses between the two topologies, the simulation results for the same rotor dimensions, air gap lengths, and outer radii of the motors are depicted in Fig. 2.7. The simulations were carried out with rotational speed set to 8000 rpm.

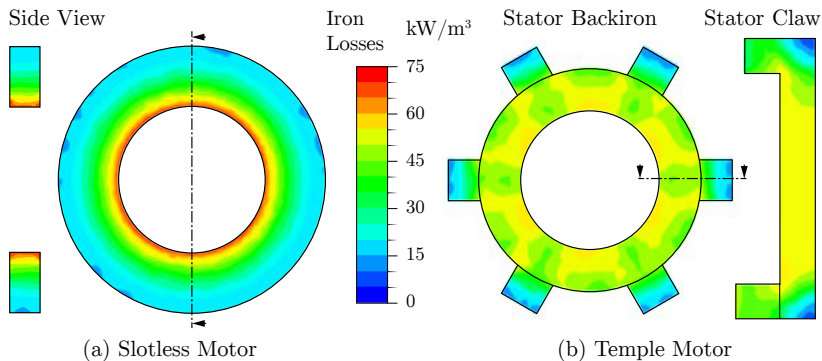


Figure 2.7: Distribution of the stator losses caused by the rotating rotor field for the slotless (a) and slotted topology (b). Both topologies feature the same rotor diameter, magnetic air gap length, and stator outer diameter.

In the slotless machine, the stator losses occur mainly on the inside of the stator ring. This is due to a slightly higher flux density at the inner radius of the stator. The difference between the inside and outside strongly depends on the cross-sectional area. With smaller surfaces, the losses are distributed more homogeneously along the radius.

The temple motor has high flux densities in the stator back iron, especially between the individual claws. Field concentrations also occur at sharp-edged transitions. The stator losses are correspondingly higher in these regions.

2.5 Topology Comparison for Pump Applications

Without going into the functionality and design guidelines of a centrifugal pump in more detail, the following section compares the two motor topologies for different operating points typical for medical applications. The exact flow conditions in the pump do not have to be known. Based on scaling considerations and empirical data, impeller diameter, speed, and pump type can be linked. For this purpose, the so-called Cordier diagram is used. This diagram provides the radius, speed, and design required to achieve the best pump efficiency for a given operating point. With this information and an estimate of the

pump efficiency, the motor efficiency can be determined. It can also be estimated whether a particular motor design provides the necessary axial stiffness to compensate for the axial thrust. A detailed description of the centrifugal pump follows in Chapter 3.

2.5.1 The Cordier-Diagram

Otto Cordier carried out an empirical study of industrial turbomachinery in the 1950s. He was able to relate the optimum impeller diameter in terms of efficiency to the operating conditions of the machines [38]. The results were summarized in the so-called Cordier diagram.

In order to make the diagram generally valid, both the impeller diameter d_a as well as the rotation speed ω are normalized using the volume flow Q and the total pressure difference Δp_{tot} .

By using the specific work

$$Y = \frac{\Delta p_{\text{tot}}}{\rho_{\text{fl}}}, \quad (2.34)$$

where ρ_{fl} stands for the density of the fluid, the two dimensionless parameters,

$$\text{diameter number} \quad \delta_{\text{C}} = d_a \frac{\sqrt{\pi}}{2} \frac{(2Y)^{1/4}}{Q^{1/2}} \quad (2.35)$$

and

$$\text{specific speed} \quad \sigma_{\text{C}} = \frac{\omega}{\sqrt{\pi}} \frac{Q^{1/2}}{(2Y)^{3/4}}, \quad (2.36)$$

can be defined.

Fig. 2.8 shows the resulting diagram. High-efficiency pumps are located in the upper Cordier range (marked with "compressors"). For turbines, the dimensions should be selected to fall within the lower Cordier-band.

For pumps, the Cordier diagram is divided along the specific speed into three areas, which provide information about the design of the pump impeller. For low specific speeds $\sigma_{\text{C}} < 0.3$, radial centrifugal pumps, which deflect the mass flow by 90° , are best suited. In the range of higher specific speeds $\sigma_{\text{C}} > 0.7$, axial centrifugal pumps, which do not change the flow direction, are preferred. The transition between the

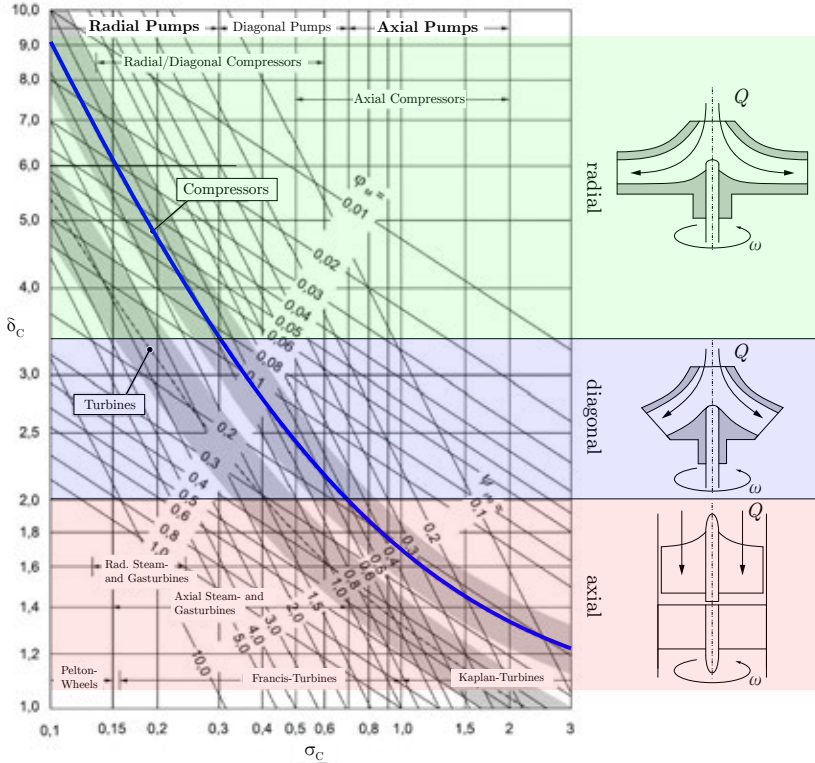


Figure 2.8: The Cordier diagram describes the optimum operating ranges of different turbomachines using the specific speed σ_C and the diameter number δ_C . The valid range for centrifugal pumps is highlighted in blue. Figure adapted from [39].

two areas is continuous and is formed by so-called diagonal pumps. On the right side of Fig. 2.8, the three pump types are exemplarily shown in a sectional view.

In general, for higher specific speed, mass flow should be less diverted and the more axial should the impeller be designed.

Torque and Efficiency

For a given operating point of the pump (Q and Δp_{tot}) and rotor diameter, Fig. 2.8 shows how fast the rotor has to turn.

The following applies as a good approximation:

$$\sigma_C = \left(\frac{\delta_C - 1.061}{0.6018} \right)^{-0.896} . \quad (2.37)$$

If the rotation speed is known, the power balance

$$P_{\text{mech}} = T_{\text{mot}}\omega = \frac{P_{\text{hyd}}}{\eta_P} = \frac{Q\Delta p_{\text{tot}}}{\eta_P} \quad (2.38)$$

can be used to calculate the required torque T_{mot} .

The efficiency of the pump η_P must be estimated using empirical data or experimental results. For bearingless radial pumps, an efficiency of approx. 40% is to be expected.

For the industrial pumps investigated by Cordier, axial pumps tend to be less efficient than radial ones [38]. The extent, to which these findings can be applied to such low volume flows that are common in medical applications, is not known. The unique flow conditions caused by the magnetic bearing also make it difficult to predict the efficiency. It is, however, certain that pumps with low flow rates achieve lower efficiencies than those with high flow rates. This is due to the higher relative roughness [40].

Therefore, it can be assumed that bearingless axial pumps do not achieve any significant increase in efficiency compared to radial pumps. For this reason, an efficiency of 40% is estimated, regardless of the pump type.

2.5.2 Axial Thrust

Due to the flow differences at the top and the bottom of the impeller, an axial thrust acts on the rotor. For radial impellers, these axial forces can be largely compensated by suitable design measures. For axial pumps, however, this is only possible at the optimum operating point. The axial thrust cannot be compensated in cases of underload or overload. It must be assumed that the entire pressure difference Δp applies to the impeller surface A_{imp} [40].

The resulting axial force

$$F_{\text{ax}} = \Delta p A_{\text{imp}} \quad (2.39)$$

must be compensated entirely by the passive magnetic bearing.

In the following considerations, a maximum deflection $\delta z_{\max} = h_{\text{rot}}/2$ is defined, which must not be exceeded for the compensation of the axis thrust so that the bearing remains stable. For the maximum achievable pressure difference, this means

$$\Delta p_{\max} \leq \frac{h_{\text{rot}} k_z}{2A_{\text{imp}}}. \quad (2.40)$$

2.5.3 Simplified Thermal Model

To estimate the motor efficiency, loss models from Section 2.4 are considered. A simplified thermal model is used to determine copper losses. It is assumed that all stator losses P_{stat} lead to homogeneous heating of the motor. Cooling takes place completely passively by convection via the external motor surface A_{sur} .

For a stationary operating point, the motor temperature ϑ will settle to a steady value and a convective flow forms on its outside. At this temperature, the heat convection is equal to the entire stator losses,

$$P_{\text{stat}} = \alpha_{\text{th}} A_{\text{sur}} (\vartheta - \vartheta_{\text{amb}}). \quad (2.41)$$

Here, ϑ_{amb} represents the ambient temperature, which is assumed to be constant.

In order to determine the heat transfer coefficient α_{th} , the motor is modelled as a vertically aligned cylinder of height h and diameter d . A convection flow is formed on its outside.

The Nusselt number Nu and the thermal conductivity λ of the ambient air can be used to determine the temperature coefficient according to

$$\alpha_{\text{th}} = Nu \frac{\lambda}{h}. \quad (2.42)$$

For the considered case of the upright cylinder, the Nusselt number

is given by [41]

$$Nu = \left[0.825 + 0.387 \cdot (Ra \cdot F_3)^{1/6} \right]^2 + 0.87 \frac{h}{d}, \quad (2.43)$$

$$F_3 = \left[1 + \left(\frac{0.492}{Pr} \right)^{9/16} \right]^{-16/9}, \quad (2.44)$$

$$Pr = \frac{\nu_{\text{air}}}{a} = \frac{\mu_{\text{air}} c_p}{\lambda} = 0.6559, \quad (2.45)$$

$$Ra = h^3 g \Delta \vartheta \frac{\gamma}{\nu_{\text{air}} a}, \quad (2.46)$$

where the parameters for air are given in Tab. 2.2.

Table 2.2: The material values used for convective cooling with air at room temperature.

Parameter	Character	Value	Unit
dynamic viscosity	μ	17.1	kPas
spec. heat capacity	c_p	1.005	kJ/(kg · K)
thermal conductivity	λ	26.2	mW/(m · K)
spatial expansion factor	γ	$3.41 \cdot 10^3$	1/K
kinematic viscosity	ν	$14.9 \cdot 10^{-6}$	m/s ²
temperature coefficient	a	$20 \cdot 10^{-6}$	m/s ²
gravitational constant	g	9.81	m/s ²

The Nusselt number Nu must be determined iteratively since the Rayleigh number Ra depends on the temperature. Also, an iterative solution for the copper losses P_{cu} is necessary, since they are also dependent on the temperature and contribute to the total losses P_{stat} .

2.5.4 Design Process

To compare the two motor topologies at different operating points, 3D FEM simulations are performed. The most critical parameters of motors are varied and the passive stiffness, the torque constant, and the losses are determined. A flowchart of the process is illustrated in Fig. 2.9.

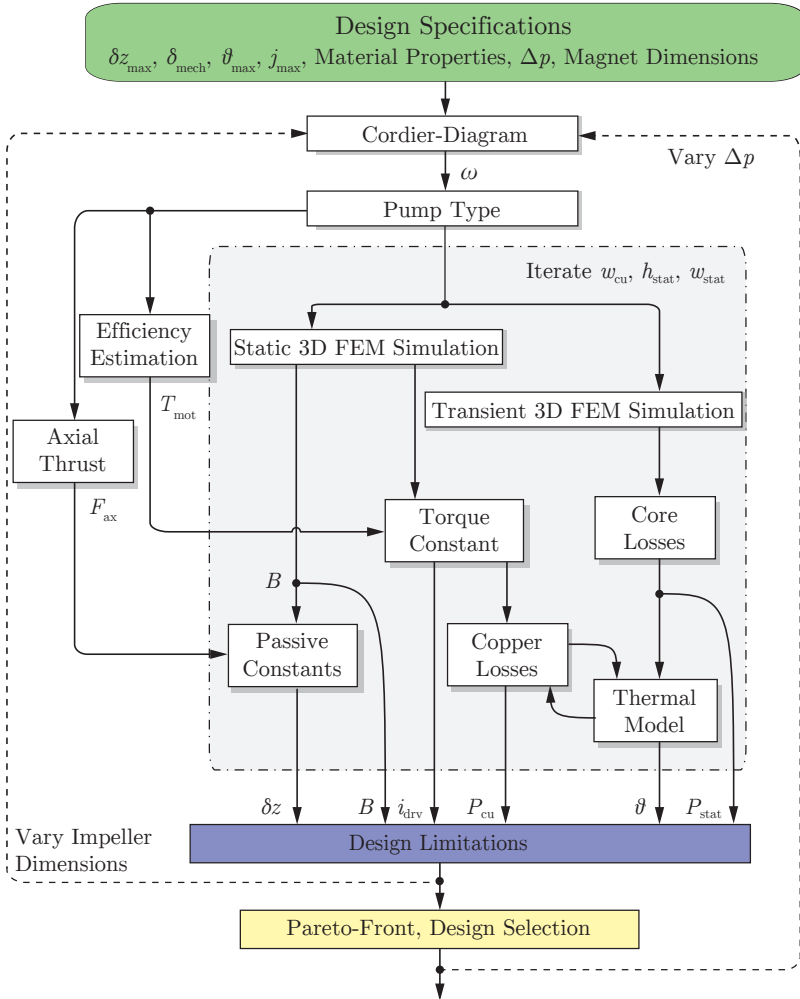


Figure 2.9: Flow diagram of the design process for determining optimal stator designs for given hydraulic operating points.

The design process begins with the specification of the impeller dimensions and the required mechanical air gap length δ_{mech} . For desired operating points (Q and Δp), the required rotation speed ω and pump

type are determined from the Cordier diagram. For axial pumps, the axis thrust F_{ax} can now be estimated using equation (2.39). The torque T_{mot} is determined under the assumption of a constant pump efficiency of $\eta_{\text{P}} = 40\%$.

Static FEM simulations can be used to determine passive stiffness and torque constant for a wide range of stator geometries. As a result, the required drive current i_{drv} and the initialization value for the copper losses P_{cu} can be calculated. The iron losses P_{stat} are estimated using transient simulations and the Steinmetz formula from equation (2.33).

If the initial values of the losses are known, the motor temperature and losses can be determined iteratively.

In addition to the above specified limitation by the axial stiffness, a maximum temperature of $\vartheta_{\text{max}} = 60\text{ }^{\circ}\text{C}$ and a maximum current density of $j_{\text{max}} = 5\text{ A/mm}^2$ are predefined. The material chosen for stator is M330-35A electrical sheet.

Design Space

For the temple motor, both the winding width w_{cu} and the stator height h_{stat} are varied. For the slotless topology, the corresponding parameters are the winding width w_{cu} and the stator width w_{stat} , respectively. For both topologies, the inner and outer radius of the rotor is also varied.

To limit the number of parameters, the claw height (or the stator height in the case of the slotless motor) is fixed to be the same as the rotor height.

A list of the considered parameter space is given in Tab. 2.3.

Table 2.3: The parameter space used for the design process.

Parameter	Variable	Temple (mm)	Slotless (mm)
rotor inner radius	r_{i}	2.5 – 7.5	2.5 – 7.5
rotor outer radius	r_{a}	{5, 10}	{5, 10}
rotor height	h_{rot}	2.5 – 5	2.5 – 5
mechanical airgap	δ_{mech}	0.5	0.5
copper width	w_{cu}	0.6 – 5	0.2 – 7.5
stator height	h_{stat}	h_{rot}	10 – 65
tooth height	h_{tooth}	–	h_{rot}

Pressure differences of 10 mmHg to 400 mmHg at a flow rate of 5 l/min are considered as operating points.

Evaluation

Pareto fronts between the motor efficiency η_{mot} and the hydraulic power density ρ_{hyd} are calculated from the results of the design process. An exemplary comparison of these Pareto fronts for the two pump types and a slotless motor for the operating point of 5 l/min and 20 mmHg is shown in Fig. 2.10.

Due to the limited axial stiffness of the magnetic bearing, the most efficient designs cannot be implemented as axial pumps. This is because the coil windings have to be wound through the air gap. A reduction in the copper losses is only possible if the magnetic air gap δ_{mag} is increased. However, this reduces the axial stiffness k_z . In addition to the axial stiffness, stator saturation also has a limiting effect. Therefore, a minimum stator width must be maintained. This mainly limits the achievable hydraulic power.

For the design space under consideration, the hydraulic power density is mainly limited by the saturation induction.

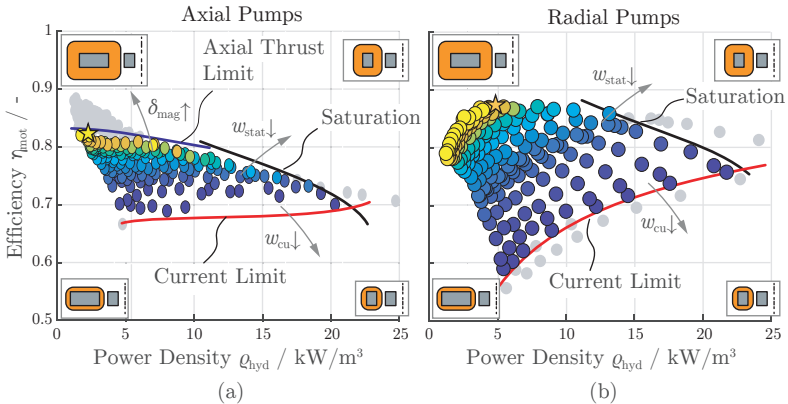


Figure 2.10: A comparison of the Pareto fronts of the slotless motor, designed as an axial pump (a) and as a radial pump (b) for the operating point of 20 mmHg at a flow rate of 5 l/min. The colour coding reflects the copper volume.

2.5.5 Classification

To assess which motor topologies and pump types are best suited for medical applications, the most efficient designs are compared. Fig. 2.11 illustrates the results for pressure differences between 10 and 400 mmHg at a flow rate of 5 l/min.

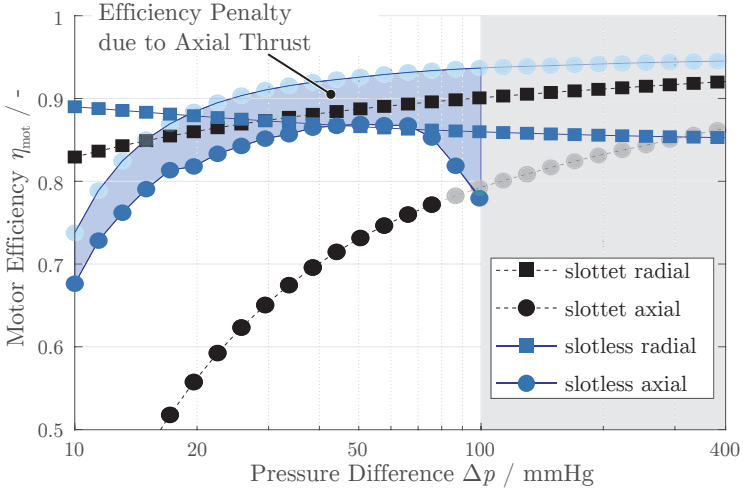


Figure 2.11: The achievable motor efficiency of the slotted (black) and slotless (blue) topology for operating pressures of 10 – 400 mmHg at a flow rate of 5 l/min. The markers give the distinction between an axial and a radial pump design.

A radial pump, driven by a slotless motor, is best suited for small pressure differences. For the axial pump, the achievable efficiency is limited by the axial thrust. No designs can be found for the dimensions and materials investigated for which the efficiency of the axial pump would exceed that of a radial pump.

With increasing pressure difference, the necessary torque increases. Copper losses are rising accordingly. Already from a pressure difference of approx. 30 mmHg, the slotted radial pump exceeds the efficiency of the slotless topologies. Especially for pressure differences above 100 mmHg (typical operating point for VAD applications), the axial stiffness of the bearingless motors is no longer sufficient to compensate for the axial thrust. Accordingly, only radial pumps are suitable for

extracorporeal applications.

Due to the higher motor efficiency, the expected higher hydraulic efficiency, and the larger construction space above the rotor, a radial pump with a slotted stator is designed for the following investigations.

2.6 Summary

The bearingless slice motor is a motor with a magnetically levitated rotor. Due to the flat rotor design, three of the six degrees of freedom are passively stable. For the considered motor topologies, the rotor is diametrically magnetized and features a pole pair number of $p_{\text{rot}} = 1$. The bearing takes place via six electromagnets, which generate a magnetic field with a pole pair number of $p_{\text{stat}} = 2$. The phase angle of the bearing current can be used to control the direction of the bearing force. The drive is realized in the same magnetic iron circuit. A single-pole-pair drive field generates the torque.

The examined topologies, namely the slotless and the slotted motor, differ in the design of the stator. While the slotless stator consists of a simple ring-shaped iron sheet stack, the slotted stator has L-shaped stator claws. Due to its design, the slotless topology is better suited for applications demanding high rotation speeds. The temple motor allows the increase in winding space without reducing the axial stiffness and is best suited for applications requiring higher torque.

The Cordier diagram was used to estimate the motor efficiency and limits due to the limited axial stiffness, stator saturation, and current density. Based on 3D FEM simulations and a simplified thermal model, the most efficient design was determined for pumping applications. For operating points with a volume flow of 5 l/min and a pressure difference of more than 100 mmHg, the bearingless slice motor in temple design, in combination with a radial impeller, is best suited.

3

The Bearingless Centrifugal Pump

This chapter outlines the functioning principle of a bearingless centrifugal pump. Starting with an overview of the individual system components in Section 3.1, the functioning principle is then described in Section 3.2. It is followed by a description of the most critical design parameters and their influence on the characteristic curves of the pump (Section 3.2.5).

The hydraulic forces acting on the rotor are of particular importance for the bearingless centrifugal pump. Their origin and relationships are explained in Section 3.4. Finally, the essential loss mechanisms are pointed out and the hydraulic efficiencies are defined.

References [42] and [43], on which the following descriptions are based, are recommended to the interested reader.

3.1 Structure and Components

Fig. 3.1 shows a cross-section of a bearingless centrifugal pump with a temple motor. It consists of three main components: stator, impeller, and pump casing. The stator, together with the rotor embedded in the impeller, forms the bearingless slice motor. The rotor bearing and drive take place through the wall of the pump head, as described in Section 2.3. Therefore, the impeller can be positioned contact-free in the centre of the pump, whereby it is completely surrounded by fluid.

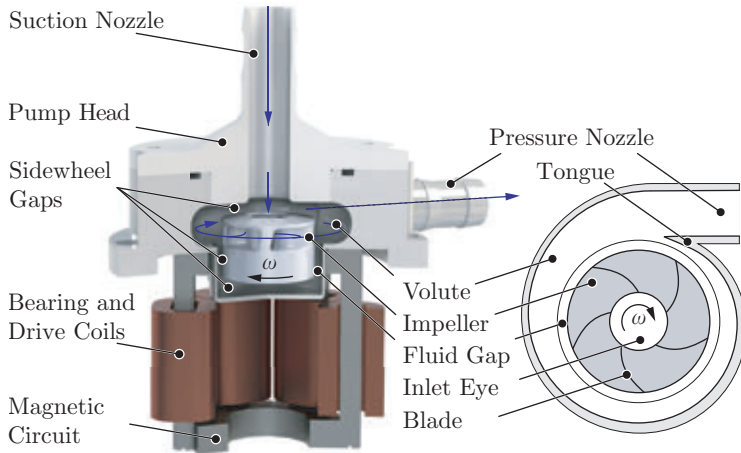


Figure 3.1: Sectional view of a bearingless centrifugal pump. Arrows indicate the main flow directions. The pump consists of the pump head, the impeller, and the bearingless stator. Additionally, there is a top view of the open impeller.

3.1.1 Flow Path

The approximate flow directions inside the pump head are illustrated in Fig. 3.1. The working fluid enters the pump head through the inlet nozzle and then flows through the suction nozzle into the impeller blade channel. The blades transfer the mechanical power to the fluid and increase its total pressure.

The fluid finally flows out of the blade channel and into the volute. The increased pressure causes the fluid to exit the pump head along the outlet nozzle.

3.1.2 Components of the Pump Head

The tubular inlet area of the pump is called the suction nozzle. It feeds the fluid to the impeller. After leaving the blade channel, the majority of the volume flows into the volute and leaves the pump through the pressure nozzle. The edge at the transition from the volute to the pressure nozzle is called the tongue or spur.

The remaining volumes, which do not contribute to the actual pump-

ing effect, are referred to as impeller sidewall gaps. These sidewall gaps are of particular importance for the bearingless pump. Due to the contactless positioning of the rotor, large gaps can occur, which cause a high leakage flow. Usually, such leakage flows should be kept as low as possible as they reduce the hydraulic efficiency of the pump. For conveying shear-sensitive fluids, however, large bearing gaps result in smaller shear forces. Thus, the increase in leakage has the desired side effect of a gentler pumping.

In the following, a distinction is made between the individual impeller sidewall gaps. The circular area above the impeller, between the impeller and the housing, is known as the shroud gap and the one below the impeller as the hub gap. The narrow space between the rotor casing and the housing cup is called the radial gap.

3.1.3 Components of the Impeller

Two sectional views of the impeller, in top and side view, are shown in Fig. 3.2. The fluid enters the impeller axially through the inlet eye. It is subsequently deflected in the radial direction and flows over the leading edge into the blade channel. The blade surfaces are divided into the pressure side and the suction side. The pressure surface faces the direction of rotation. It is responsible for pressure generation and power transmission from the impeller to the fluid. The suction side is the surface facing away from the direction of rotation.

The fluid exits the blade channel at the trailing edge of the impeller.

The upper side of the blade channel is called the front shroud and the underside is called the rear shroud. The cylinder encapsulating the rotor magnet is called the hub.

For the bearingless pump considered below, there is a bore through the supporting disc along the axis of rotation. It enables a pressure equalization between the upper and lower side of the impeller. This reduces the axial thrust. Furthermore, it increases the leakage through the radial gap, thus increasing the washout of the bottom volume.

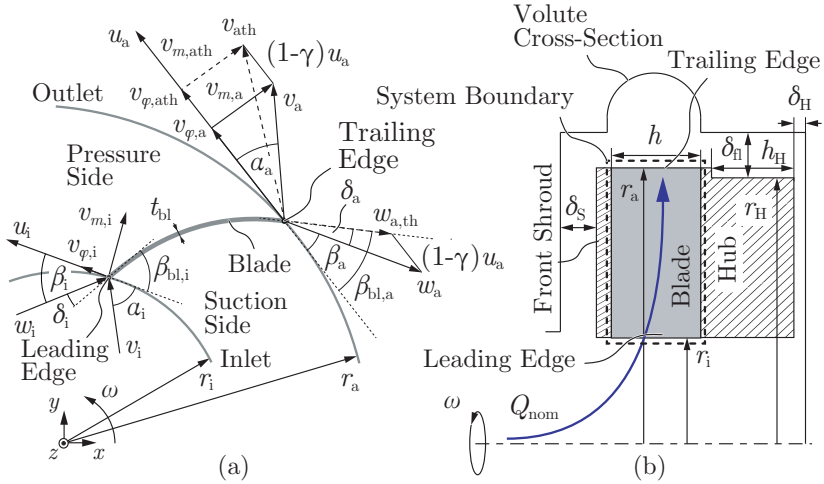


Figure 3.2: Top (a) and side view (b) of the impeller. The speed triangles are depicted at the inlet (subscript i) and the outlet (subscript a) of the blade channel. Figure (a) is adapted from [40].

3.2 Operating Principle of the Centrifugal Pump

The conversion from mechanical to hydraulic work takes place largely in the blade channel of the impeller, which is schematically shown in Fig. 3.2. In order to establish the connections between the impeller design and energy transfer, in the following, the power balance is first set up on the impeller and then linked to its geometric conditions using the principle of angular momentum.

3.2.1 Power Balance

If a control volume consisting of the blade channel with the system boundaries on the leading and trailing edges is observed (see Fig. 3.2), then it has the internal energy E . This energy forms a state variable of the control volume and consists of the movement and binding energies of the molecules and nucleons. The internal energy can be changed by supplying mechanical work W , heat Q , and mass flows \dot{m} across the system boundary. According to the first law of thermodynamics, the

following applies

$$\frac{dE}{dt} = \int_{\partial V} (\dot{Q} + \dot{W} + \dot{m}_i h_{\text{tot},i} - \dot{m}_a h_{\text{tot},a}) dA. \quad (3.1)$$

Here, h_{tot} is the specific enthalpy bound to the mass flow \dot{m} , flowing across the system boundary into the control volume (index i), or out of it (index a).

$$h_{\text{tot}} = e + \frac{p}{\rho} + \frac{1}{2} \bar{v}^2 + gz. \quad (3.2)$$

For centrifugal pumps, $\dot{Q} = 0$ can be assumed to be a good approximation, since the exchange of heat is mostly by advection and not by heat conduction. A stationary process $dE/dt = 0$ is also assumed.

Under these conditions, the energy balance (3.1) simplifies to

$$\Delta h_{\text{tot}} = \frac{P_{\text{mech}}}{\dot{m}} = e_a - e_i + \frac{p_a - p_i}{\rho_{\text{fl}}} + \frac{\bar{v}_a^2 - \bar{v}_i^2}{2} + g(z_a - z_i), \quad (3.3)$$

where the mass conservation $\dot{m}_i = \dot{m}_a = \dot{m}$ was applied.

The change in internal energy $e_2 - e_1$ of the fluid flowing across the boundaries is caused by its heating due to friction losses in the blade channel. These losses are considered as specific pressure losses $\Delta p_V / \rho_{\text{fl}}$.

The usable mechanical work at the system outlet is designated as specific work

$$Y = \frac{\Delta p}{\rho_{\text{fl}}} + \frac{\Delta \bar{v}^2}{2} + g\Delta z. \quad (3.4)$$

It is lower than the theoretical specific work by the amount of heat losses

$$Y_{\text{th}} = Y + \frac{\Delta p_V}{\rho_{\text{fl}}} = \Delta h_{\text{tot}}. \quad (3.5)$$

3.2.2 Angular Momentum

A mass particle m , which moves in the blade channel at position \vec{r} with the absolute velocity \vec{v} , has the angular momentum

$$\vec{L} = \vec{r} \times m\vec{v}. \quad (3.6)$$

Here, the conservation of the angular momentum applies

$$\frac{d\vec{L}}{dt} = \vec{r} \times \dot{m}\vec{v} = \vec{T}. \quad (3.7)$$

In the equation above, \vec{T} contains all torques acting on the mass particle m . Therefore, the following applies to the entire blade channel

$$\vec{T}_{\text{bl}} = \dot{m}_{\text{bl}} (\vec{r}_{\text{a}} \times \vec{v}_{\text{a}} - \vec{r}_{\text{i}} \times \vec{v}_{\text{i}}), \quad (3.8)$$

whereby the total amount of mass flow passing through the blade channel must be entered for \dot{m}_{bl} .

If the velocity vector is divided into a tangential and a meridional component $\vec{v} = v_{\varphi} \vec{e}_{\varphi} + v_m \vec{e}_m$, the Euler turbine equation

$$Y_{\text{th}} = \frac{T_{\text{bl}} \omega}{\dot{m}_{\text{bl}}} = (r_{\text{a}} v_{\varphi, \text{a}} - r_{\text{i}} v_{\varphi, \text{i}}) \omega \quad (3.9)$$

is obtained. It must be mentioned that the torque T_{bl} acting on the blade channel does not correspond to the total torque transmitted onto the impeller. It is reduced by the sum of shear forces acting on the impeller sidewalls.

The absolute velocities of the fluid \vec{v} at the blade inlet and outlet can be divided into a circumferential velocity \vec{u} of the impeller and a relative component \vec{w} . The speed triangle applies

$$\vec{v} = \vec{u} + \vec{w}. \quad (3.10)$$

When inserted into equation (3.9), it results in

$$Y_{\text{th}} = u_{\text{a}} v_{\varphi, \text{a}} - u_{\text{i}} v_{\varphi, \text{i}}. \quad (3.11)$$

If equations (3.11) and (3.5) are combined, while neglecting the friction losses and without increasing the position potential, it results in

$$\frac{\Delta v^2}{2} + \frac{\Delta u^2}{2} - \frac{\Delta w^2}{2} = \frac{\Delta v^2}{2} + \frac{\Delta p}{\rho_{\text{fl}}}. \quad (3.12)$$

Consequently, the static pressure is generated by increasing the centrifugal force and reducing the relative velocity.

This is applicable for any type of rotary pump. For centrifugal pumps, both u and v_{φ} are usually increased from inlet to outlet. For axial pumps, u remains almost unchanged. Energy is transmitted exclusively by increasing the peripheral speed. The static pressure on the outlet is generated solely by the deceleration of the fluid.

3.2.3 Blade Blockage

If the flow in the blade channel follows the blade shape, the following applies according to the velocity triangle

$$v_{\varphi, \text{th}} = u - \frac{v_m}{\tan(\beta_{\text{bl}})} = \omega r - \frac{Q_{\text{bl}}}{2\pi r h_{\text{bl}} \tan(\beta_{\text{bl}})}, \quad (3.13)$$

where h_{bl} is the blade height, Q_{bl} the volume flow through the blade channel, and β_{bl} the blade angle. The volume flow Q_{bl} consists of the net flow and leakage

$$Q_{\text{bl}} = Q_{\text{net}} + Q_{\text{leak}} = \frac{Q_{\text{net}}}{\eta_{\text{vol}}}. \quad (3.14)$$

Therefore, the specific blade work depending on the impeller geometries can be described as

$$Y_{\text{th}} = (\omega r_a)^2 - \frac{\omega \epsilon_a}{2\pi h_a \tan(\beta_{\text{bl}, a})} \cdot Q_{\text{bl}}. \quad (3.15)$$

It was simplistically assumed that the entering fluid has no swirl ($v_{\varphi, 1} = 0$) and that the blade channel is blocked by n_{bl} blades, each with the blade thickness t_{bl} . This blockage is then taken into account by

$$\epsilon_a = \frac{2\pi r_a}{2\pi r_a - n_{\text{bl}} t_{\text{bl}} \csc(\beta_{\text{bl}, a})} > 1. \quad (3.16)$$

Blade blockage always leads to a reduction of the cross-section in the blade channel and, therefore, to an increase of the meridional velocity component.

3.2.4 Flow Deflection

Due to the pressure difference between the suction and pressure sides of the impeller blade, the fluid does not leave the impeller congruently with the blades. It is deflected against the rotational speed of the impeller u_a . This leads to a reduction of the tangential component $v_{\varphi, a}$ according to

$$v_{\varphi, \text{ath}} - v_{\varphi, a} = (1 - \gamma) u_a, \quad (3.17)$$

where the slip coefficient γ can be estimated by

$$\gamma = f_1 \left(1 - \sqrt{\sin(\beta_{\text{bl}, a}) n_{\text{bl}}^{-0.7}} \right) k_W > 0 \quad (3.18)$$

if the number of blades is $n_{\text{bl}} > 3$. For radial pumps, $k_{\text{W}} = 1$ and $f_1 = 0.98$ can be assumed [40].

Since the flow deflection reduces the tangential speed $v_{\varphi,a}$ of the fluid, the achievable specific work is also reduced.

Consequently, the maximum specific work can be estimated by

$$Y_{\text{th}} = \gamma(\omega r_a)^2 - \frac{\omega \epsilon_a}{2\pi h_a \tan(\beta_{\text{bl},a})} \cdot \frac{Q_{\text{net}}}{\eta_{\text{vol}}}. \quad (3.19)$$

3.2.5 Relationship between the Design Parameters

It is now possible to determine how the pump characteristic curve changes by adjusting the impeller geometry. The following considerations are based on equation (3.19) and thus neglect any friction losses in the blade channel. Also, only blade angles $\beta_{\text{bl},a} \leq \pi/2$ are considered, because otherwise, the characteristic curve shows a positive gradient, which can lead to unstable operating points.

Under these conditions, equation (3.19) represents a linear equation with the ordinate and abscissa intercepts

$$Y_{\text{th,max}} = \gamma(\omega r_a)^2 \quad \text{and} \quad (3.20)$$

$$Q_{\text{net,max}} = 2\pi\eta_{\text{vol}} \frac{\gamma}{\epsilon_a} \tan(\beta_{\text{bl},a}) h_a \omega r_a^2. \quad (3.21)$$

From this, the following conclusions can be drawn:

1. The maximum pressure head can only be influenced by the circumferential speed ωr_a and the slip. It scales quadratically with the circumferential speed and linearly with the slip coefficient γ .
2. For $\beta_{\text{bl},a} = 90^\circ$, the pressure head is independent of the flow rate.
3. For $\beta_{\text{bl},a} < 90^\circ$ the pressure head drops linearly with the flow rate.
4. Greater blade heights h_a lead to a flatter characteristic curve and increase the maximum achievable flow rate.
5. Without slip, h_a and $\tan(\beta_{\text{bl},a})$ have the same effect on the characteristic curve. However, the slip is only influenced by $\beta_{\text{bl},a}$.
6. With increasing the outlet angle $\beta_{\text{bl},a}$, the slip increases. This reduces the specific work. At the same time, the maximum flow rate increases and the characteristic curve becomes flatter.

7. The increase in the rotational speed ω leads to steeper characteristic curves. Both pressure and flow are increased.
8. An increase in the blade radius r_a leads to a parallel shift of the characteristic curve, towards higher output powers.
9. The slip coefficient γ has the same impact as r_a^2 .
10. Higher blade numbers n_{bl} lead to an increase in the slip coefficient γ and therefore less slip. If the blockage is kept constant, the deliverable pressure head increases and the characteristic curve is shifted parallel. If the blade thickness t_{bl} is kept constant, the characteristic curve becomes steeper.
11. A higher blockage (smaller ϵ_a) increases the gradient of the characteristic curve and reduces the maximum flow rate.
12. With increasing volumetric efficiency η_{vol} , the gradient of the characteristic curve decreases.

3.3 Losses

The previous considerations were based on a flow without losses. However, due to viscosity of the fluid, losses that cannot be neglected occur in the boundary layers. The fluid flowing back via the impeller sidewall gaps also leads to a reduction in the usable nozzle work, since the blade channel has to convey a larger volume flow than the one arriving at the nozzle.

The essential loss mechanisms and their influence on the characteristic curve are schematically depicted in Fig. 3.3 and described in the following.

3.3.1 Loss Components

Since no mechanical bearing losses occur in the bearingless pump, the entire mechanical work P_{mech} is transferred directly to the impeller. The impeller rotates in a viscous fluid. As a result, friction losses $P_{V,R}$ occur on the impeller sidewalls. The remaining power $P_{bl} = \eta_R P_{mech}$ is transferred to the blade channel. In the blade channel, this power is transferred to the mass flow $\dot{m}_{bl} = \rho Q_{bl}$.

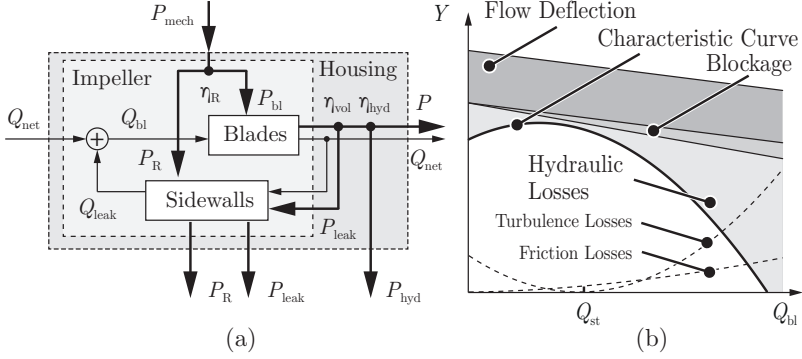


Figure 3.3: Schematic representation of the pump losses (a) and the characteristic curve (b).

A part of the fluid, conveyed by the impeller blades, flows through the impeller sidewall gaps back to the inlet eye. Specific blade work is also transferred to this leakage flow Q_{leak} , which, however, does not reach the pressure nozzle. Such losses are taken into account by the volumetric efficiency

$$\eta_{\text{vol}} = \frac{Q_{\text{net}}}{Q_{\text{bl}}} = \frac{Q_{\text{net}}}{Q_{\text{net}} + Q_{\text{leak}}}. \quad (3.22)$$

All friction and turbulence losses that occur between the inlet and discharge nozzles lead to the reduction in the implemented hydraulic power and are taken into account via the hydraulic efficiency η_{hyd} . For the usable nozzle work, it follows

$$P = \rho Q_{\text{net}} \eta_{\text{hyd}} Y_{\text{th}} = \eta_{\text{hyd}} \eta_{\text{vol}} \eta_{\text{R}} P_{\text{mech}}. \quad (3.23)$$

The losses lead to the heating of the fluid. Due to the usually high throughput of the pump, a large part of the heat is dissipated by convection via the useful volume flow. The walls of the pump head can thus be assumed to be adiabatic.

In the following, the loss mechanisms are described in more detail.

3.3.2 Impeller Sidewall Losses

Losses on the impeller sidewalls occur due to viscous friction both on the hub and shroud discs, as well as on the lateral surface. The total impeller sidewall losses can be obtained as a sum of the individual surfaces

$$P_{V,R} = P_{R,M} + P_{R,H} + P_{R,S}. \quad (3.24)$$

For very low rotational speeds, the flows are directed in the circumferential direction and shear forces acting on the impeller sidewalls can be calculated analytically. However, for bearingless centrifugal pumps, the rotational speeds are significantly higher and the wall shear stresses must be estimated using the empirically determined loss coefficient c_v .

The losses on the two cover surfaces and on the lateral surface are calculated according to (valid for $Re > 10$, [38])

$$P_{R,M} = c_{v,M} \rho_{fl} \omega^3 r_a^4 h_M, \quad (3.25)$$

$$P_{R,SH} = c_{v,SH} \rho_{fl} \omega^3 (r_a^5 - r_i^5), \quad (3.26)$$

where h_M is the height of the lateral surface.

The loss coefficient c_v strongly depends on the dominant Reynolds number $Re = \rho_{fl} \omega r_a^2 / \mu_{fl}$. For hydraulically smooth surfaces, it can be estimated according to [40] as follows.

The friction coefficient for the lateral surface is given by

$$c_{v,M} = \frac{2\pi r_a}{Re \delta_{fl}} + \frac{0.075}{Re^{0.2}} \cdot \frac{2(r_a + \delta_{fl})}{2r_a + \delta_{fl}}. \quad (3.27)$$

For $\delta_{fl} \ll r_a$, the losses on the lateral surface A_M can be approximated by

$$P_{R,M} \approx \frac{\mu_{fl}}{\delta_{fl}} u_a^2 A_M. \quad (3.28)$$

For the losses caused by the disc surfaces, a distinction must be made between laminar and turbulent flows. Turbulent flow conditions are to be expected for the bearingless centrifugal pump. Furthermore, it must be distinguished whether the two boundary layers on the housing and on the impeller are combined or formed separately (with a viscosity-free core flow in between them).

The following applies to the corresponding friction coefficients:

$$c_{v,\text{SH}} = \frac{0.02}{Re^{0.25}} \left(\frac{r_a}{\delta_{\text{ax}}} \right)^{1/6} \quad \text{combined boundary layers,} \quad (3.29)$$

$$c_{v,\text{SH}} = \frac{0.0255}{Re^{0.2}} \left(\frac{\delta_{\text{ax}}}{r_a} \right)^{1/10} \quad \text{separated boundary layers.} \quad (3.30)$$

As long as the boundary layers are separated, the friction losses are reduced if the axial distance δ_{ax} is reduced. As soon as the boundary layers are unified, the friction is increased with decreasing distance.

3.3.3 Leakage Losses

The leakage flow circulates through the impeller sidewall gaps between the blade outlet and the blade inlet. The specific blade work Y_{bl} that is transferred to the leakage flow dissipates along the trajectory due to friction and turbulence. The following applies to the losses

$$P_{V,\text{leak}} = \rho_{\text{fl}} Q_{\text{leak}} Y_{\text{bl}} = \rho_{\text{fl}} \left(\frac{1}{\eta_{\text{vol}}} - 1 \right) Q_{\text{net}} Y_{\text{bl}}. \quad (3.31)$$

Measurements or simulations must be used to determine the leakage flow Q_{leak} .

To obtain an estimation of the influence of the operating point on the leakage losses, the flow through a ring gap is considered. The relation between the leakage flow and the pressure drop across the gap is given by [44]

$$Q_{\text{leak,sp}} = \mu_{\text{fl}} A_{\text{sp}} \sqrt{\frac{2\Delta p}{\rho_{\text{fl}}}}, \quad (3.32)$$

where Δp is the pressure drop over the considered route and A_{sp} the cross-section of its area.

In the bearingless centrifugal pump, the leakage flow always takes place between the outlet and inlet of the blade channel. The driving pressure difference thus corresponds to the pressure difference across the impeller channel Δp_{bl} . According to equation (3.19), this can be described as a linear function of the blade flow rate Q_{bl} . For the ratio of leakage losses to blade power, the following applies approximately

$$\frac{P_{V,\text{leak}}}{P_{\text{bl}}} \approx \mu_{\text{fl}} A_{\text{sp}} \sqrt{\frac{2}{\rho_{\text{fl}}}} \frac{\sqrt{c_1 - c_2 Q_{\text{bl}}}}{Q_{\text{bl}}}. \quad (3.33)$$

Thus the leakage losses are particularly significant at low flow rates. For a blade angle of $\beta_{a,bl} = 90^\circ$, the pressure difference across the impeller channel is independent of the flow rate and $c_2 = 0$ applies. This means that the leakage losses along the characteristic curve remain constant for a 90° blade angle, at least theoretically.

3.3.4 Hydraulic Losses

The hydraulic losses include all friction and turbulence losses, which are attributable to the useful volume flow Q_{net} .

The friction losses lead to a reduction of the specific blade work by

$$Y_{hyd,R} = \frac{1}{2}\xi w^2, \quad (3.34)$$

where the loss coefficient ξ is to be determined by measurements.

The turbulence losses are caused by the incorrect inflow to the impeller blades at underload and overload. The misalignment between the incoming flow and the blade angle causes a shock. If Q_{st} is the volume flow leading to a shock-free stream, the reduction in specific blade work can be described as [44, 45]

$$Y_{hyd,st} \propto \left(1 - \frac{Q_{bl}}{Q_{st}}\right)^2. \quad (3.35)$$

These losses are increased quadratically with the increase in distance to the shock-free flow rate Q_{st} . The curves of these two loss components are drawn as dashed lines in Fig. 3.3(b).

Due to the complex flow conditions inside the bearingless pump, simulations are used in this work.

3.4 Hydraulic Forces

As a result of uneven pressure distribution within the pump, forces on the impeller occur, which must be compensated by the bearing. These forces can be partially balanced or at least reduced by suitable design measures. Radial and axial forces are of particular importance here.

The magnetic bearing can actively compensate for the radial forces if the magnitude and frequency of these forces are limited to controllable values. As a result of the uneven pressure distribution along the volute circumference, only increased bearing losses are to be expected.

The passive axial bearing, on the other hand, requires that the maximum bearing force $F_{\max, \text{bng}, z}$ and thus the permitted deflection δz_{\max} are not exceeded. Since the axial bearing force cannot be controlled, special attention must be paid to the axial thrust during the impeller design.

3.4.1 Radial Forces

The radial forces acting on the impeller originate from two sources. On one hand, the pressure distribution in the volute has a minimum of static pressure near the discharge nozzle, as the fluid flows out of the pump housing there. The maximum pressure usually occurs near the volute tongue. The distribution can be described by the Fourier series

$$p_{\text{stat}}(\varphi) = \sum_k \hat{p}_{\text{stat}, k} \cos(k\varphi - \theta_{\text{stat}, k}). \quad (3.36)$$

On the other hand, the rotating impeller causes pressure maxima at the trailing edges. This generates an n_{bl} -pole pressure distribution in the stator, which rotates at the rotor frequency ω (blade resonance)

$$p_{\text{rot}}(\varphi, t) = \sum_k \hat{p}_{\text{rot}, k} \cos(kn_{\text{bl}}(\varphi - \omega t) - \theta_{\text{bl}, k}). \quad (3.37)$$

Static Radial Forces

The pressure field in the volute has a static component, which at the same time corresponds to the pressure distribution caused by the volute shape $p_{\text{stat}}(\varphi)$. If pressure is integrated along the rotor circumference, the stationary radial force acting on the impeller is obtained. It is strongly dependent on the flow coefficient

$$\phi = \frac{Q}{2\pi r_a h_a u_a} \quad (3.38)$$

and the volute design.

According to [40], the following applies

$$F_r = k_r(\phi) \rho_{\text{fl}} \omega_a^2 r_a^3 h_a, \quad (3.39)$$

where the force coefficient k_r is to be determined from experiments. Fig. 3.4(a) depicts the radial force as a function of the flow rate Q for the tests from [46].

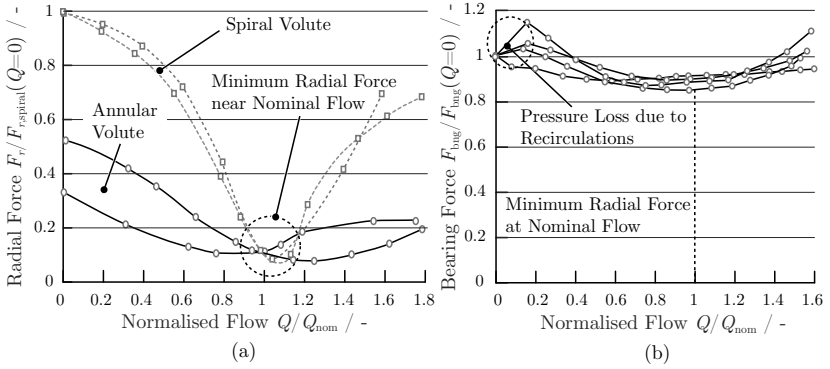


Figure 3.4: Flow rate dependence of the static radial force for different volute shapes (a) and the verification of the bearing force in bearingless radial pumps with annular housing (b). Graphic (a) adapted from [43].

For spiral shaped volutes (dashed lines), the minimum coefficient is reached in the area of the optimum flow rate. However, if the flow deviates from the ideal conditions, the coefficient rises rapidly due to flow disturbances at the tongue.

A simple annular housing (solid lines) causes a higher radial force at the nominal operating point, but exhibits lower dependency on the operating point. Especially when operating against a closed valve ($Q = 0$), it causes a significantly lower radial force, since the fluid can circulate freely in the volute.

The typical radial force curve for annular housings could be confirmed for the bearingless centrifugal pump (see Fig. 3.4(b)).

Impeller-Volute Interaction

The pressure pulsations of the impeller act as a source of a pressure wave that moves into the volute and reflects on its walls. This leads to the interference between volute and impeller [42]. The resulting pressure distribution can be described as

$$p(\varphi, t) = \sum_k \hat{p}_k \underbrace{\cos(kn_{\text{bl}}(\varphi - \omega t) - \theta_{\text{stat},k})}_{\text{Blade Shape}} \underbrace{\cos(k\varphi - \theta_{\text{stat},k})}_{\text{Volute Shape}}. \quad (3.40)$$

The amplitude depends strongly on the distance between the impeller outlet and the interference object (in this case, the volute wall).

The higher the spacing, the more the pressure waves are damped, and the smaller the acting forces become [42].

The resulting force can excite tilt movements of the impeller. An annular volute is better suited to avoid this. Except for the discharge area, the annular volute has no geometric deviation from a circle. The pressure distribution, according to equation (3.40), thus rotates with the rotor frequency and generates hardly any harmonics. From a rotor-oriented coordinate system, forces that act on the impeller are almost stationary. Tilting movements are thus only slightly induced.

Due to occurrence of turbulence, the true pressure distribution deviates somewhat from previous considerations. Therefore, the stability against tilting movements must be tested experimentally.

3.4.2 Axial Forces

There are fluid-filled side chambers above and below the impeller shroud and hub, respectively. Normally, the flows in these spaces are turbulent and the boundary layers of the rotor and the housing wall can be assumed to be separate. If the leakage flow is neglected, fluid particles in these side spaces move on circular paths due to the rotation of the impeller. Accordingly, a pressure gradient is formed in the radial direction.

$$\rho_{\text{fl}} \frac{u_{\varphi}^2}{r} = \frac{\partial p}{\partial r} \quad (3.41)$$

For constant rotational speeds, the pressure at the inner radius r_i is smallest and increases quadratically with the radius. According to [42], the pressure distribution can be described by

$$p(r) = \rho_{\text{fl}} (k\omega)^2 \frac{x^2}{2} \Big|_{x=r_i}^r + p(r_i), \quad (3.42)$$

where the relative velocity between the core flow and the circumferential speed of the impeller is taken into account via the factor $k = v_{\varphi}/u$.

Through the integration of the pressure profile on the shroud and hub discs, the acting force is finally obtained by

$$F_{\text{ax,SH}} = \int_{r=r_i}^{r_a} 2\pi r p(r) dr. \quad (3.43)$$

However, if a leakage flow is present, it conveys a constant angular momentum into the control volume thus influencing the pressure

distribution. Due to the pressure gradient pointing radially outwards, the mass flow moves from the trailing edges back to the centre of the impeller. The angular momentum of each mass particle is conserved. Therefore, the tangential velocity of the sidewall flow increases with decreasing radius. According to energy conservation, the radial pressure gradient decreases. Since usually the leakage flow through the front shroud gap is larger than the flow along the hub sidewall gap, the axial force tends to point towards the inlet nozzle.

In addition to the described force, the rotor experiences a force in opposite direction of the incoming flow, due to the impulse deflection

$$\dot{p} = \frac{dm}{dt} v_z + m \frac{dv_z}{dt}. \quad (3.44)$$

For a stationary flow and complete redirection, the following applies

$$F_{\text{ax, in}} = -\dot{m} v_{z, i}. \quad (3.45)$$

To be able to fully compensate the axial thrust, the front shroud and hub disc surfaces should be designed in such a way that

$$F_{\text{ax, in}} + F_{\text{ax, H}} + F_{\text{ax, S}} = 0. \quad (3.46)$$

With the same leakage flow across the front shroud gap and along the hub gaps, the washout hole in the impeller centre should be slightly smaller than the inlet eye diameter. However, for the bearingless centrifugal pump the leakage across the shroud disc is larger than the one along the hub disc. For the same shroud and hub disc areas, the resulting force caused by the pressure distribution is directed towards the shroud. Thus, it partly compensates the impulse force.

However, as real pressure distribution varies along the circumference within the impeller sidewall gaps, the above considerations apply only approximately. Therefore, the dimension of the washout hole must be determined experimentally. For the prototypes examined later, equally large disc surfaces proved to be suitable.

4

Blood Damage

This chapter provides the knowledge necessary to understand the damage mechanisms of blood in centrifugal pumps. In addition to the fluid-mechanical properties of blood, results from in vitro investigations are gathered, and the most critical factors influencing blood damage are highlighted (Section 4.1 and Section 4.2). Based on the in vitro experiments, mathematical models which were developed by different authors, are used to simulate haemolysis in medical devices. Implementation possibilities of such models in CFD simulations and the encountered difficulties are presented in Section 4.3.

4.1 Blood as Fluid

4.1.1 Components

Human blood consists of 55 %_{vol} of an aqueous solution (blood plasma) and 45 %_{vol} of cellular components, by volume. About 98 %_{vol} of the solid components by volume are taken up by the red blood cells (RBC) or erythrocytes. The thrombocytes and leukocytes make up only 1 – 2 %_{vol}.

The volume fraction of RBC related to the total blood volume is called haematocrit (H_t). It can be determined by centrifugation, with RBCs settling on the ground.

RBCs, in turn, consist of a cell membrane and are filled with a solution saturated with haemoglobin (H_b). This solution contains 32 % haemoglobin and 65 % water by weight, as well as inorganic elements such as potassium, sodium, magnesium, and calcium [47]. Haemoglobin plays a vital role in gas transportation within the bloodstream.

A detailed list of the components is given in Tab. 4.1.

Table 4.1: Summary of blood components and their indicators according to [47]. Here, σ is the volume concentration related to whole blood, V is the volume, and C is the particle density related to whole blood.

Component	Erythrocytes	Leucocytes	Thrombocytes
Function	gas transport	immune system	hemostasis
Shape	biconcave disc	spheric	oval
σ (%vol) [48]	36-50	< 1	< 1
Mass (μm)	$8 \times 1 - 3$	7 - 22	2-4
V (μm^3)	98	180-5600	6
C ($10^3/\mu\text{l}$)	$4 - 6 \cdot 10^3$	4 - 11	250 - 500
Life Time (d)	100 - 120	≈ 10 [49]	5 - 11
Content	water 65% hemoglobin 32% K, Na, Mg, Ca		

Erythrocytes

Due to their size and quantity, RBCs have a large influence on the fluidic behaviour of blood [47]. As will be explained later, RBCs are also suitable for determining the degree of blood damage. Therefore, the erythrocytes are here described in more detail.

Fig. 4.1(a) depicts a human RBC with its typical dimensions. It has a biconcave disc shape with a diameter in the range of $7 - 9 \mu\text{m}$. The height is between $2.3 - 2.9 \mu\text{m}$.

The biconcave shape creates a high surface to volume ratio, which is essential for gas transport. This ensures high deformability, allowing the RBC to pass through capillaries of $6 \mu\text{m}$ in diameter [50].

The mass density of RBCs is $\rho_{\text{RBC}} = 1.085 - 1.115 \text{ g/cm}^3$. They are thus only slightly heavier than blood plasma ($\rho_{\text{P}} = 1.03 \text{ g/cm}^3$) [47]. The haemoglobin content of a blood cell is about $3.45 \cdot 10^{-8} \text{ mg}$. The haemoglobin concentration in whole blood of a healthy human is between $14.0 - 17.5 \text{ g/dl}$ for men and $12.3 - 15.3 \text{ g/dl}$ for women [48].

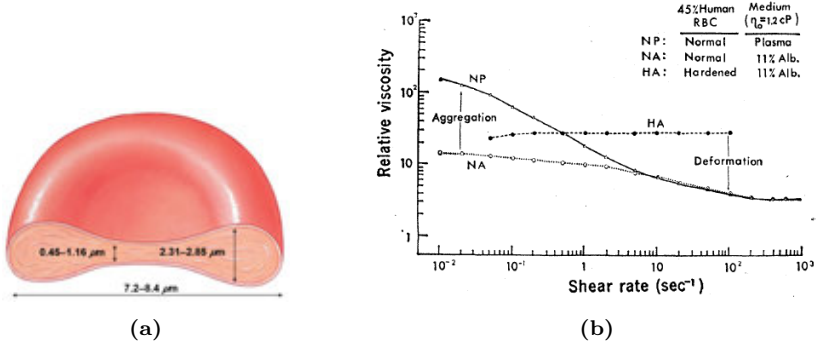


Figure 4.1: Representation of a human RBC with the main dimensions (a). Dependence of viscosity on the effective shear rate (b). The difference between NP and NA is due to the formation of rouleaux. Images taken from [51] and [52].

4.1.2 Fluidic Properties

As described above, blood is a suspension in which the fluid (plasma) exhibits a Newtonian behaviour. The non-Newtonian properties of blood are caused by RBCs [53, 54]. Since RBCs form stacks when at rest (rouleaux formation), which separate when the shear rate $\dot{\gamma}$ increases (see Fig. 4.2), blood has a shear-thinning property [47].

The relative viscosity μ can be described by the Carreau-Yasuda model [53]

$$\mu(\dot{\gamma}) = \mu_{\infty} + \frac{\mu_0 - \mu_{\infty}}{(1 + (\lambda\dot{\gamma})^b)^a}, \quad (4.1)$$

with the parameter values

$$\mu_0 = 1.6 \cdot 10^{-1} \text{ Pa} \cdot \text{s} \quad (4.2)$$

$$\mu_{\infty} = 3.5 \cdot 10^{-3} \text{ Pa} \cdot \text{s} \quad (4.3)$$

$$a = 1.23, \quad b = 0.64, \quad \lambda = 8.2 \text{ s}. \quad (4.4)$$

The viscosity has the highest value μ_0 at an unloaded state, decreases towards higher shear rates, and converges to μ_{∞} . As illustrated in Fig. 4.1(b), this behaviour is due to rouleaux formation and the deformability of RBC.

Blood can, therefore, be considered as a Newtonian fluid if the shear rate is sufficiently high. However, the threshold above which this assumption is justified varies widely in the literature. Thus, values between 50 s^{-1} and 5000 s^{-1} are mentioned [55, 56].

For the flow in turbomachinery, the assumption of a constant viscosity is permissible. Typical values are $\mu \approx 3.5\text{ mPas}$ and a density of 1060 kg/m^3 [55, 56].

4.2 Haemolysis

Haemolysis is a disaggregation of RBCs whereby the hemoglobin (H_b) contained in the cells leaks from the membrane and is diluted in the surrounding plasma. Hemoglobin dissolved in the plasma is called the plasma-free haemoglobin $H_{b,\text{pf}}$.

The degree of haemolysis is also measured via the $H_{b,\text{pf}}$. For this purpose, the haemolysis index HI is usually defined as

$$HI = \frac{H_{b,\text{pf}}}{H_b}, \quad (4.5)$$

which represents the number of destroyed RBCs related to the total count.

Haemolysis can be caused by aging of red blood cells, high osmotic pressure differences, and mechanical effects on the RBC membranes. Certain cell destruction is always present in the bloodstream since the lifespan of RBC is only about 120 days. They are then decomposed in bone marrow, liver, and spleen [49].

During the mechanical circulation of blood, RBCs are exposed to higher stress, which partly results in a greatly increased cell damage.

A plasma-free haemoglobin value above $H_b > 20\text{ mg/dl}$ is referred to as haemolysis [57]. An anaemia ensues if the haemolysis exceeds the bodys formation of new RBCs. The average new formation (erythropoiesis) is $160 \cdot 10^6\text{ RBC/min}$ [49].

For the development of a cell-preserving pump, the dependence of the cell damage on the shear forces, the surface quality, and the pressure are of particular importance. These influential parameters will be discussed in more detail below.

4.2.1 Shear Forces

As displayed in Fig. 4.3, the shear forces influence the shape of the RBC membrane. At low shear rates, the rouleaux break apart into separate RBCs. With a further increase of the shear rate to $\dot{\gamma} = 1.15 \text{ s}^{-1}$, RBCs start to wobble and from 2.3 s^{-1} to align themselves in the stream direction. From 11.5 s^{-1} on, they finally deform elliptically. With a further increase in the shear rate, the membrane begins to rotate around the haemoglobin inside (tank-treading) [54]. Finally, the membrane is damaged, and haemoglobin leaks into the plasma (haemolysis).

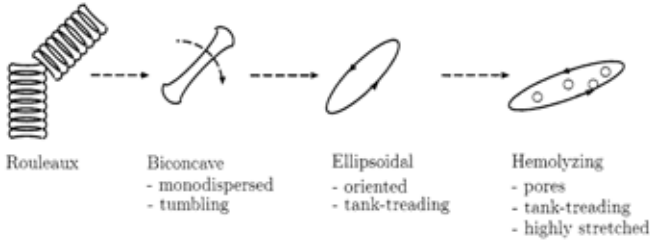


Figure 4.2: Change of the shape of RBC as a function of the shear rate. Image taken from [53].

The extent to which haemolysis occurs depends not only on the shear force, but also on the time during which the RBCs are exposed to these forces.

Shear Threshold

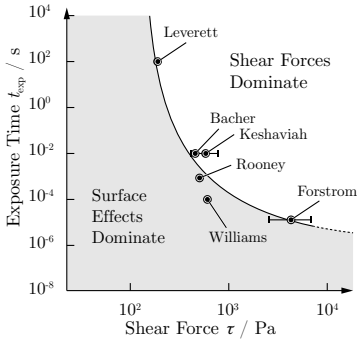
Similar to the tensile strength in mechanical tensile tests, there is also a threshold value of the shear stress τ_{th} , up to which the RBC membrane deformation is reversible. If this value is exceeded, the cell membrane gets irreversibly damaged or destroyed.

Many authors have conducted studies under constant shear loads to determine this value [58–66]. It turns out that the threshold value is time-dependent according to [67, 68]

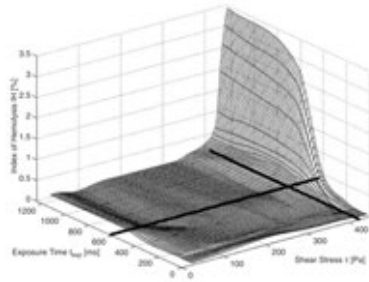
$$\tau_{\text{th}}[\text{Pa}] = 88.905 \cdot t_{\text{exp}}[\text{s}]^{-0.3372}. \quad (4.6)$$

Here, t_{exp} is the residence time of RBC under the constant shear stresses.

Leverett suspected that haemolysis at $\tau > \tau_{th}$ was due to shear stress and at $\tau < \tau_{th}$ was due to interactions between RBC and surfaces (see Fig. 4.3(a)). He already determined a time dependence of haemolysis in the range of high shear forces [64].



(a) Leverett’s theory that the process of cell damage can be divided into two areas.



(b) Dependence of the shear-induced haemolysis on the shear stress τ and residence time t_{exp} .

Figure 4.3: Threshold values of the shear stress that leads to cell destruction and its time dependence. Illustrations adapted from [64] and [65].

Further studies with residence times in the range of 25 – 1250 ms were conducted by Paul [65]. Experiments with constant shear forces were carried out in the range of $\tau \in [30, 450]$ Pa. As pointed out in Fig. 4.3(b), threshold values of $\tau_{th} = 425$ Pa and $t_{exp} = 620$ ms were determined.

At an exposure time of 620 ms, according to equation (4.6), the occurrence of haemolysis would already be expected at approx. 100 Pa. This illustrates that the prediction of the threshold is inaccurate and should only be used to estimate the threshold value in orders of magnitude.

Shear-Induced Haemolysis

For the haemolysis caused by shear forces, based on experimental data of Wurzinger et al. [69], the power law model was finally derived by

Giersiepen et al. [70]

$$\frac{\Delta H_{b,\text{pf}}}{H_b} = c_{\text{chem}} t_{\text{exp}} [\text{s}]^\alpha \tau [\text{Pa}]^\beta = 3.62 \cdot 10^{-7} \cdot t_{\text{exp}} [\text{s}]^{0.785} \tau [\text{Pa}]^{2.416}. \quad (4.7)$$

The exponent $\alpha < 1$ is explained by a hardening of the cell membrane [71].

The experiments were all performed using a Couette viscometer in the ranges $\tau \in [57, 255]$ Pa and $t_{\text{exp}} \in [7, 700]$ ms. According to the author, the mathematical model exhibits an error of less than 5% in the range $t_{\text{exp}} < 0.1$ s and less than 12% in the range $t_{\text{exp}} > 0.1$ s.

Generalisation

Equation (4.7) only represents the observations of cell damage after t_{exp} for the case of a constant shear force τ . Therefore, for the haemolysis rate $f(\tau, t)$, the following applies

$$\frac{\Delta H_{b,\text{pf}}}{H_b}(\tau, t_{\text{exp}}) = c_{\text{chem}} t_{\text{exp}} [\text{s}]^\alpha \tau [\text{Pa}]^\beta = \int_0^{t_{\text{exp}}} f(\tau, t) dt. \quad (4.8)$$

Since the shear loads in the experiments were not time-dependent, this is fulfilled by

$$f(\tau, t) = \alpha c_{\text{chem}} t [\text{s}]^{\alpha-1} \tau [\text{Pa}]^\beta. \quad (4.9)$$

However, if the shear load is time-dependent, $\tau = \tau(t)$, as is the case with a centrifugal pump, the above equation no longer applies. The available experiment data cannot be used to determine the desired primitive function $f(\tau(t), t)$. Therefore, it cannot be assumed that the use of equation (4.9) leads to correct predictions of the haemolysis rate in complex flows with time-dependent shear loads.

Nevertheless, this model is often used in CFD simulations. Probably because of its simplicity and the lack of better alternatives.

4.2.2 Static Pressure

Another cause of cell damage is the pressure exerted on the cell membrane. Several studies conclude that cell damage occurs when exposed to negative pressure. Since this effect only appears with simultaneous air enclosure and bubble formation, it can be assumed that local cavitation is responsible for cell destruction [72–75].

Cell damage due to increased static pressure alone could not be proven [72, 73, 76]. However, if the increased static pressure occurs in combination with shear rates above $\dot{\gamma} > 500 \text{ s}^{-1}$, haemolysis is stronger than under normal atmospheric conditions [77].

Studies on centrifugal pumps show that haemolysis increases more than linearly with the pressure difference [78, 79]. However, since the pressure difference increases quadratically with the circumferential speed u and thus approximately also the shear forces τ , it is expected, according to equation (4.7), that haemolysis scales with

$$HI \propto \tau[\text{Pa}]^{2.4} \propto \Delta p[\text{Pa}]^{1.2}. \quad (4.10)$$

However, the results from [80] indicate that there is a higher dependency. Is not clear from this study to what extent the increased static pressure within the pump leads to this additional haemolysis.

4.2.3 Surface Roughness

According to Fig. 4.3(a), cell damage in the range of low shear rates is mainly caused by surface effects and can be attributed to the surface roughness of the contacting surfaces [81–84].

Investigations were carried out using rotational shear equipment to determine the threshold value of surface quality below which no measurable haemolysis takes place. However, the threshold values in literature vary widely between authors. For example, Maruyama et al. mention a value between $R_a = 0.4 \text{ }\mu\text{m}$ and $0.8 \text{ }\mu\text{m}$ [83, 84]. On the other hand, Monroe et al. assume a much higher threshold of about $R_a = 4 \text{ }\mu\text{m}$ [82]. These studies were carried out under atmospheric pressure.

Takami et al. investigated the influence of rough surfaces in centrifugal pumps. A smooth surface is particularly important for applications with increased pressure differences [85, 86]. The surface of the impeller seems to be less critical than that of the casing. Tests with additively manufactured impellers also indicate that importance of surface quality increases with increasing pressure difference [87].

4.3 CFD Simulations of Haemolysis

Based on the experimentally observed dependence of haemolysis on shear force and residence time, models that can be implemented in

CFD simulations were derived. However, the high variation of the experimental results led to the development of several models over the years. Only a few of these are presented in the following. The work of Yu et al. [88] is recommended to the interested reader.

Due to the complex process of cell damage, this is still only understood to a limited extent. Besides, the flow conditions in centrifugal pumps are far more complicated than in the experimental setups on whose data the haemolysis models were derived. Accordingly, it is not surprising that the results of such CFD simulations deviate strongly from in vitro tests [89,90].

It is by no means to be assumed that simulations lead to the correct prediction of haemolysis. Nevertheless, important aspects of cell damage can be qualitatively assessed. This can provide helpful information about the critical regions in the pump.

4.3.1 Model Approaches

The most common haemolysis models are all based on finding by Giersiepen et al. [70] that the haemolysis rate is due to shear forces and loading time. The following relation applies

$$\frac{\Delta H_{b,pf}}{H_b} = c_{chem} t_{exp} [s]^\alpha \tau [Pa]^\beta. \quad (4.11)$$

The choice of parameters depends on the blood used and shows high variance in the literature. A selection is given in Tab. 4.2.

For example, the parameter c_{chem} shows differences of more than one order of magnitude. The exponent of the exposure time is also subject to variations, but it is always $\alpha < 1$, although a linear time dependence was assumed in the original data [58].

It is known that the original model overestimated haemolysis in the range of one order of magnitude. It is, therefore, recommended to adjust the parameter c_{chem} [89].

4.3.2 Lagrangian and Eulerian Formulation

A frequently used method to incorporate the haemolysis model into a CFD simulation is based on particle tracking algorithms (Lagrangian formulation). The flow field is first calculated and the damage rate is then integrated along the particle trajectories. The advantage of

Table 4.2: Parameter selection of different authors for the power law model of Giersiepen et al. [70].

c_{chem}	α	β	Author
$1.210 \cdot 10^{-7}$	0.7470	2.0040	Taskin [56]
$3.620 \cdot 10^{-7}$	0.7850	2.4160	Giersiepen [70, 91, 92]
$1.508 \cdot 10^{-8}$	0.7850	2.4160	Goubergrits [68]
$1.800 \cdot 10^{-8}$	0.7650	1.9910	Heuser [62, 93]
$1.228 \cdot 10^{-7}$	0.6606	1.9918	Zhang [94]
$1.745 \cdot 10^{-8}$	0.7762	1.963	Fraser [95]

this approach is that cell destruction can be calculated independently of the Navier-Stokes equations in a post-processing step. The problem, however, is that a finite number of particles must be inserted. They flow only through a part of the entire flow field. Leakage flows, in particular, are hardly covered, although it is to be expected that a large part of the haemolysis takes place in the sidewall gaps.

Alternatively, an Eulerian formulation can be derived. For the power law, one such formulation is presented in [96]. It has the advantage that cell destruction is represented by a scalar field. Thus, a haemolysis rate can be assigned to each position within the flow field. The additional transport equations to be solved significantly increase the required computing power.

4.3.3 Implementation of an Eulerian Model

Several approaches have been proposed for the implementation of an Eulerian haemolysis model. The Single-Stage and Double-Stage models are presented below.

Single-Stage Model

The most frequently implemented haemolysis model is presented in [97]. The haemolysis rate is modeled with a single transport equation. The implementation effort and the required computational power are thus kept low.

To take into account the non-linear relationship of haemolysis with the residence time, a new damage variable HL is introduced as

$$HI = HL^\alpha. \quad (4.12)$$

Accordingly, the following applies to the power law model from equation (4.7)

$$HL^\alpha = \left[(c_{\text{chem}}\tau[\text{Pa}]^\beta)^{1/\alpha} t[\text{s}] \right]^\alpha. \quad (4.13)$$

The term in square brackets depends linearly on time and can be formulated as a transport equation

$$\frac{\partial HL}{\partial t} + (\vec{v} \cdot \nabla) HL = S_{\text{HL}} \quad (4.14)$$

$$S_{\text{HL}} = (c_{\text{chem}}\tau[\text{Pa}]^\beta)^{1/\alpha}. \quad (4.15)$$

When solved with a CFD solver, the haemolysis index HI can finally be calculated using equation (4.12).

Alternatively, the amount of already destroyed cells can also be considered by applying the source term S_{HL} only to the still vital cells. The result is the transport equation

$$\frac{\partial HL}{\partial t} + (\vec{v} \cdot \nabla) HL = (c_{\text{chem}}\tau[\text{Pa}]^\beta)^{1/\alpha} (1 - HL). \quad (4.16)$$

For cell-friendly pumps, as considered in this paper, the degree of damage is so low that these two equations can be regarded as identical.

The source term in equation (4.14) is not time-dependent. Consequently, the model lacks any information about the load history of the cell. Hardening of the cell membrane is simply ignored.

Double-Stage Model

An additional transport equation can be introduced to take into account the residence time or the loading history of a cell in the finite volume under consideration. For this purpose, either the total residence time ψ or a haemolysis-dose D_b can be applied, which leads to the two equations

$$\frac{\partial \psi}{\partial t} + (\vec{v} \cdot \nabla) \psi = 1 \quad \text{and} \quad (4.17)$$

$$\frac{\partial D_b}{\partial t} + (\vec{v} \cdot \nabla) D_b = \tau[\text{Pa}]^{\beta/\alpha}. \quad (4.18)$$

The formulation based on a haemolysis-dose is according to [98].

These two transport equations accumulate the residence time or load dose of a particle along its trajectory. The locally generated haemolysis can thus be weighted according to the history of the cell. The result is the transport equation

$$\frac{\partial HI}{\partial t} + (\vec{v} \cdot \nabla) HI = S_{HI}, \quad (4.19)$$

with the respective source terms

$$S_{HI,\Psi} = \alpha c_{\text{hem}} \psi^{\alpha-1} \tau [\text{Pa}]^{\beta} \quad \text{and} \quad (4.20)$$

$$S_{HI,D_b} = \alpha c_{\text{hem}} D_b^{\alpha-1} \tau [\text{Pa}]^{\beta/\alpha}. \quad (4.21)$$

In contrast to the single-stage model, membrane hardening is thereby taken into account. However, the additional transport equation increases the computing effort.

Threshold Implementation

In addition, constant threshold values for the shear force that lead to cell damage can be defined for all models. For this purpose, a weighting function for the source term of the haemolysis is added.

If the load history of the cell damage is implemented by equation (4.17), time dependence of the threshold value can be implemented according to

$$\tau_{\text{th}}[\text{Pa}] = 88.905 \cdot \psi[\text{s}]^{-0.3372}. \quad (4.22)$$

A physically more reasonable definition of the threshold value should be based on the loading dose. However, necessary studies and data are not available.

4.3.4 Equivalent Shear Stress

In the above considerations, a one-dimensional shear stress τ was always assumed. Flow condition within a pump, however, is much more complicated than for one-dimensional, directed flows. Accordingly, the stress state of the fluid must be described by a tensor $\underline{\sigma}$, which is derived from the velocity field and the viscosity.

In order to estimate the cell damage with the above models, the three-dimensional stress state must then be converted to a scalar equivalent using invariants.

In the following, the relationship between the velocity field \vec{v} and the stress tensors $\underline{\sigma}$ and $\underline{\tau}$ is described and possible equivalent stresses are presented. The following description is based on the book by Kundu et al. [99], in which the interested reader can find further and generally valid considerations.

Stress Tensor

The velocity gradient $\nabla\vec{v}$ can be used to describe the relative motion of neighbouring particles. It can be divided into a symmetric component \underline{S} and a rotational component \underline{R}

$$\nabla\vec{v} = S_{ij} + \frac{1}{2}R_{ij}, \quad (4.23)$$

where

$$S_{ij} = \frac{1}{2} (\nabla\vec{v} + (\nabla\vec{v})^T) \quad (4.24)$$

$$R_{ij} = (\nabla\vec{v} - (\nabla\vec{v})^T). \quad (4.25)$$

The symmetric strain rate tensor \underline{S} can be expressed in component notation as

$$S_{ij} = \frac{1}{2} \left(\frac{\partial v_i}{\partial x_j} + \frac{\partial v_j}{\partial x_i} \right) = S_{ji}. \quad (4.26)$$

In general, the following applies to the stress tensor of a moving, incompressible fluid

$$\sigma_{ij} = -p\delta_{ij} + \tau_{ij}, \quad (4.27)$$

where p is the fluid-static stress and τ_{ij} the fluid-dynamic stress. The shear stress tensor τ_{ij} is referred to as the deviatoric stress tensor. Only the symmetrical part of $\nabla\vec{v}$, S_{ij} , contributes to this tensor.

For a linear, isotropic material, the relationship between the shear stress tensor and the strain tensor is given by

$$\tau_{ij} = K_{ijmn}S_{mn}, \quad (4.28)$$

where the elasticity tensor (fourth order tensor) is given by

$$K_{ijmn} = \lambda\delta_{ij}\delta_{mn} + 2\mu\delta_{im}\delta_{jn}. \quad (4.29)$$

Here, λ and μ represent the Lamé constant and the shear modulus, respectively.

Therefore, the following applies to the shear stress tensor

$$\tau_{ij} = \lambda \delta_{ij} S_{mm} + 2\mu S_{ij}. \quad (4.30)$$

Since for an incompressible fluid the following applies

$$S_{mm} = \nabla \cdot \vec{v} = 0. \quad (4.31)$$

The shear stress tensor then simplifies to

$$\tau_{ij} = 2\mu S_{ij}. \quad (4.32)$$

Equivalent Shear Stress

Since the in vitro experiments to determine cell damage were carried out with one-dimensional shear loads, the tensor obtained by simulations must be converted to an equivalent, scalar shear stress. This can be done using the invariants of the deviatoric stress tensor $\underline{\tau}$.

Usually, the first,

$$I_{\underline{\tau}} = \text{tr}(\underline{\tau}) = \tau_{11} + \tau_{22} + \tau_{33}, \quad (4.33)$$

or second main invariants,

$$II_{\underline{\tau}} = \frac{1}{2} (\text{tr}(\underline{\tau})^2 - \text{tr}(\underline{\tau}^2)) \quad (4.34)$$

$$= \tau_{11}\tau_{22} + \tau_{22}\tau_{33} + \tau_{11}\tau_{33} - \tau_{12}^2 - \tau_{23}^2 - \tau_{13}^2, \quad (4.35)$$

are used. However, these can be combined, resulting in further invariants, such as

$$\text{tr}(\underline{\tau}^2) = I_{\underline{\tau}}^2 - 2II_{\underline{\tau}}. \quad (4.36)$$

Since the deviatoric stress tensor is symmetrical ($\underline{\tau} = \underline{\tau}^T$), this corresponds to the magnitude of the tensor squared,

$$\text{tr}(\underline{\tau}^2) = |\underline{\tau}|^2 = \tau_{11}^2 + \tau_{22}^2 + \tau_{33}^2 + 2\tau_{12}^2 + 2\tau_{23}^2 + 2\tau_{13}^2 = \underline{\tau} : \underline{\tau}. \quad (4.37)$$

There is no common agreement on which combination to use as equivalent stress. The problem is addressed in detail in [100]. The equivalent formulations used by different authors are listed in Tab. 4.3.

Variable $\tau_{\sqrt{3}}$ is a scaled variation of the von Mises equivalent stress τ_{VM} . The reason for the scaling is that the cell damage was examined

Table 4.3: Possible equivalent shear stresses.

Variable	Relation to Stress Tensor	Authors
τ_{vM}	$\sqrt{\frac{3}{2}(I_\tau^2 - 2II_\tau)}$	[101]
$\tau_{\sqrt{3}}$	$\sqrt{\frac{1}{2}(I_\tau^2 - 2II_\tau)}$	[92, 100, 102, 103]
τ_{II}	$\sqrt{-nII_\tau}, \quad n = 1, 2, 3\dots$	[88]
τ_B	$\sqrt{\frac{1}{6} \sum_{i \neq j} (\tau_{ii} - \tau_{jj})^2 + \sum_{i \neq j} \tau_{ij}^2}$	[104]
τ_Y	$\sqrt{\sum_{i \neq j} (\tau_{ii} - \tau_{jj})^2 + \sum_{i \neq j} \tau_{ij}^2}$	[88]

under shear stress and not under normal stress. These are excessively weighted by a factor of $\sqrt{3}$ in τ_{vM} [100, 102].

The different equivalent stress formulations clearly lead to different haemolysis predictions. If it is considered that the shear force contributes to the haemolysis index by τ^α , it becomes clear that, depending on the choice of parameters and models, predictions can differ by multiples.

4.3.5 Difficulties

The disagreement regarding the haemolysis model, its parameters, and the equivalent stress to be used, illustrate that the existing haemolysis simulations are not reliable. The disagreement can be traced back to the fact that the original experiments, from which the models were derived, caused a one-dimensional, constant shear load on RBCs. The extent to which the stress needs to be weighted in the normal direction is uncertain. Also, little is known about the time dependency.

Furthermore, interactions between cells and walls cannot be simulated. For example, the simulation of the surface structure of the pump head would be far too computationally intensive. A remedy would be an additional source term in the transport equations. However, the necessary experimental investigations are not available. The investigations from Chapter 6 will make it clear that no simple characterisation of the haemolysis caused by the surface roughness is possible.

Differences between in vitro experiments and CFD simulations are often in the range of one order of magnitude, even for simple, one-

dimensional flow conditions [88].

A precise prediction of cell damage using CFD simulations is therefore not possible. Nevertheless, such models are useful to get a better understanding of the damage mechanism.

5

Systematics

In the work at hand, investigations on cell damage in bearingless centrifugal pumps are carried out experimentally and with the aid of simulations. This chapter explains in detail the procedures employed.

Section 5.1 describes the design of the bearingless centrifugal pump for an operating point of 5 l/min at a pressure difference of 350 mmHg. This working point corresponds to the nominal operating point of a cardiopulmonary bypass. The main dimensions of the pump are determined using the Cordier diagram. After that, inlet radius, blade height, and outlet angle are determined.

The tested variations of the pump to investigate the influence of different design parameters on the hydraulic properties and the haemolysis are presented in Section 5.1.4.

The methods used to evaluate the hydraulic properties and cell compatibility are explained in Sections 5.2 and 5.3.

The chapter concludes with a detailed description of the implementation of the fluid dynamic simulation (see Section 5.4).

5.1 Centrifugal Pump

In the following section, the design of the impeller and the pump head of the base prototype is presented, following the basics from Chapter 3. The first part introduces the impeller design. Subsequently, the volute design is shortly discussed. Finally, the variations of the impeller and pump head that were manufactured for the investigation of the haemolysis are presented. The terminology used can be found in Fig. 3.2.

5.1.1 Impeller Design

The impeller is designed in the following steps:

- ▶ Selection of a suitable impeller diameter d_a
- ▶ Dimensioning of the inlet diameter d_i
- ▶ Selection of the blade angle $\beta_{bl,a}$ and the blade height h_{bl} .

These steps are described in detail below.

Diameter

The Cordier diagram from Fig. 2.8 is used to determine a suitable impeller diameter for achieving high efficiency. As shown in Section 2.5.5, only a radial pump is acceptable for the desired pressure difference of $\Delta p_{nom} = 350$ mmHg. The diameter number must, therefore, be at least $\delta_C > 3.5$.

For a fluid density of $\rho = 1060$ kg/m³, the specific work is

$$Y = \frac{\Delta p_{nom}}{\rho} = 44.02 \frac{\text{m}^2}{\text{s}^2}. \quad (5.1)$$

Using the diameter numbers from equation (2.35), a minimum impeller diameter of $d_a > 11$ mm can be determined.

To minimize the influence of manufacturing tolerances and to simplify manufacturing, a diameter of $d_a = 22$ mm, i.e. a diameter number $\delta_C = 6.54$, is selected.

The corresponding specific speed according to Cordier is

$$\sigma_C = 2\sqrt{\pi}n \frac{Q^{1/2}}{(2Y)^{3/4}} = \frac{\omega}{\sqrt{\pi}} \frac{Q^{1/2}}{(2Y)^{3/4}} \approx 0.137. \quad (5.2)$$

Thus, a rotation speed of $n \approx 7300$ rpm is expected.

Inlet Radius

The incoming fluid passes through the inlet eye towards the leading edge of the impeller blade. At this point, the swirl of the flow is relatively low and only caused by the viscosity of the fluid. Accordingly, there are high relative velocities between the impeller blade and the fluid at

the leading edge. Since this causes high shear forces and, consequently, more haemolysis, it is desirable to minimize the relative speed.

By looking at the velocity triangle at the blade inlet, the relative velocity w_i can be expressed as

$$w_i = \sqrt{v_{m,i}^2 + \left(u_i - \frac{v_{m,i}}{\tan(\alpha_i)}\right)^2}, \quad (5.3)$$

where

$$v_{m,i} = \frac{4Q_{bl}}{\pi d_i^2} \quad \text{and} \quad u_i = \frac{d_i}{2}\omega. \quad (5.4)$$

The corresponding minimum is achieved with an inlet eye diameter of

$$d_i = \sqrt[3]{\frac{2Q_{bl}}{\omega\pi} \left(\sqrt{2(17 + \cos(2\alpha_i))} \csc(\alpha_i) - 2 \cot(\alpha_i)\right)} \quad (5.5)$$

with $\csc(\alpha_i) = 1/\sin(\alpha_i)$.

Assuming a volumetric efficiency of $\eta_{vol} = 0.4$, the ideal diameter is $d_i = 9.9$ mm. Accordingly, an inlet eye radius of $r_i = 5$ mm is chosen for the prototypes.

Blade Angle and Height

Once the inlet and outlet diameters of the impeller have been determined, the design of the impeller blade follows. The aim is to identify a suitable combination of blade angle and height. As can be seen from equation (3.19), these two parameters cannot be determined separately.

Typical design procedures begin with the selection of an outlet angle of $\beta_{bl,a} = 22.5^\circ$ [40, 43]. This typically leads to a high pump efficiency. However, since efficiency is of secondary importance for a cell-friendly pump, an alternative approach is chosen below. The desired operating point is to be reached at the lowest possible rotational speed to minimize the shear forces in the sidewall gaps.

Based on equation (3.19), the theoretical rotational speed n required to reach the nominal operating point can be calculated. A larger blade height h_{bl} reduces the meridional velocity $v_{m,a}$ at the trailing edge. This makes the pump curve flatter. Accordingly, the required rotational speed decreases.

The same applies to the outlet angle $\beta_{bl,a}$. The higher it is selected, the higher the maximum flow will be. At the same time, however, slip also increases, which reduces the available pressure head.

Fig. 5.1 presents the required rotational speed as a function of the two design parameters h_{bl} and $\beta_{bl,a}$. In addition, the best and the worst outlet angles for a low-speed design are indicated by dashed lines.

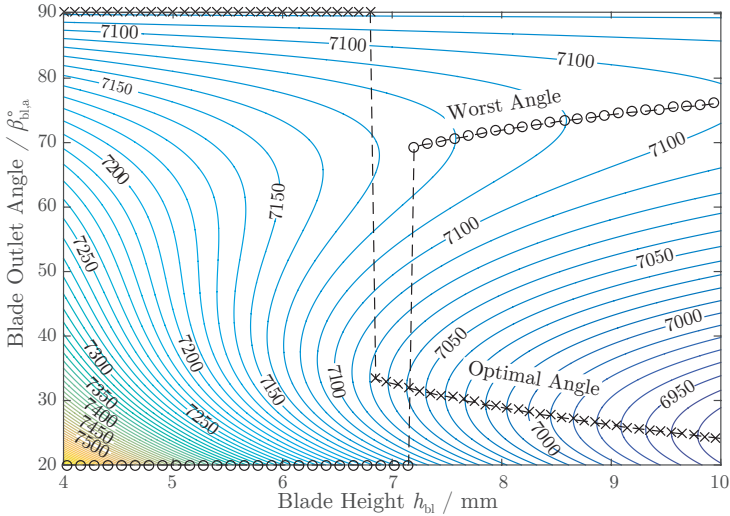


Figure 5.1: Theoretically necessary rotational speed n (in rpm) to reach the nominal operating point as a function of blade height h_{bl} and blade exit angle $\beta_{bl,a}$. The optimum and the worst combination of the two parameters for a low rotational speed are marked with crosses and circles, respectively.

The lowest rotational speed is achieved for small outlet angles $\beta_{bl,a}$ and high blades. In this range, however, rotational speed is very sensitive to changes in the blade height h_{bl} . At $h_{bl} < 6.8$ mm, a blade angle of $\beta_{bl,a} = 90^\circ$ becomes optimal, while low angles lead to high rotational speeds and are located close to the worst choice. Furthermore, the advantage of a small blade angle in the range $h_{bl} > 6.8$ mm compared to that of 90° is negligible.

To analyse the cell damage, another significant advantage of a 90° outlet angle is the decoupling of the two design parameters. In this way, the blade height h_{bl} can be varied without having any influence on the required rotational speed. In this way, the impact of the blade height on the cell damage can be investigated, at least theoretically, independent of the rotational speed.

5.1.2 Volute Design

Decisive parameters for the volute design are shear forces at the tongue as well as radial forces. As can be seen from Section 3.4.1, the irregular flow distribution in the volute causes considerable radial forces that must be compensated by the magnetic bearing. A spiral volute would be suitable for reducing forces at the nominal operating point. However, this has several disadvantages:

- ▶ The operation of the pump in underload or overload causes high radial forces. This makes it difficult or impossible to start the machine against the closed valve.
- ▶ The short distance between the impeller and the tongue causes sharp pressure fluctuations, which stimulate tilting of the impeller.
- ▶ High shear forces are to be expected in the tongue area. It is expected that they could lead to additional cell destruction.

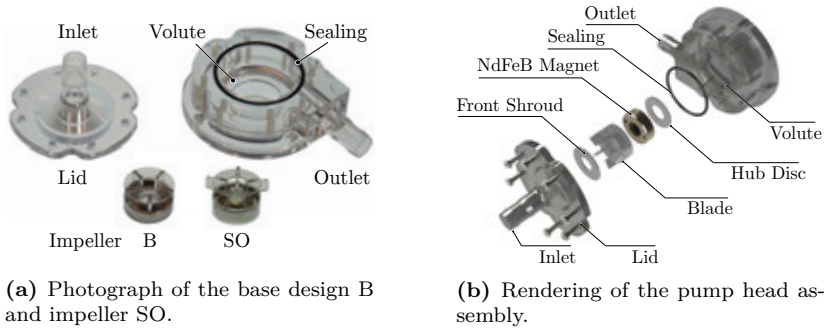
A simple annular volute is a reasonable alternative. It consists of a circular volume with a constant cross-section along the circumference. The radial forces are also lowest in the nominal flow range and increase only slightly in the event of under and overload (see Section 3.4.1).

Next, the distance between the blade outlet and the volute wall is chosen, as is usually done for conventional pump designs. The larger cross-sectional area of the volute reduces the peripheral velocity of the flow near the volute wall. The same choice is typically made for slurry pumps to keep the abrasion of the pump head low [43].

5.1.3 Resulting Design

The resulting pump is illustrated in Fig. 5.2(a). The priming volume of this design is 15.5 ml, which is about half the volume of commercially available products (see Section 9.1). At a nominal flow rate of 5 l/min, this volume is flushed within 186 ms.

For the haemolysis tests, all parts were milled from polycarbonate and then vapor-polished. This results in a smooth, transparent surface with a mean roughness value of about 0.05 μm .



(a) Photograph of the base design B and impeller SO.

(b) Rendering of the pump head assembly.

Figure 5.2: The prototypes are milled from polycarbonate. To be able to test different impellers, the housing is made of two parts and sealed with an O-ring.

5.1.4 Variations for Haemolysis Tests

In the following, the variations made to the pump design to investigate the causes of cell damage are presented. Design parameters that have little effect on the efficiency of the pump but influence the shear forces and stagnation volumes were preferred.

The parameters described can be found in Fig. 3.2.

Variations of the Pump Head

In the area of the pump inlet, there is a strong change in the flow direction. As a result, high shear forces are expected. A variation of the rounding $r_{i,st}$ at the inlet nozzle should serve to investigate this influence more closely (design R+). In order to vary the bottom gap volume, a pump head H- with a reduced distance δ_H between the impeller hub and the housing bottom is manufactured. In addition, the distance δ_S between the front shroud plate and the housing lid is varied (design S+).

A list of the different variations is presented in Tab. 5.1. The dimensions of the basic design refer to the pump head in Fig. 5.2(a).

Impeller Variations

Since the blade channel represents a significant narrowing of the flow cross-section, three different blade heights are tested (B, B+ and B-).

Table 5.1: Variations of the pump head.

Design	δ_H (mm)	δ_S (mm)	$r_{i,st}$ (mm)	Addressed Effect
B	4.5	2	1	base design
H-	2.5	2	1	bottom volume
S+	4.5	4	1	shroud volume
R+	4.5	2	6	nozzle fillet

Due to the blade angle of 90° , this should have little influence on the rotational speed and thus on the shear forces in the sidewall gaps. One exception is the fluid gap δ_S above the front shroud disc, as it directly depends on the blade height.

High shear forces prevail in the radial gap due to high relative speeds and narrow gap width. Besides, fluid particles that flow through these regions are exposed to these stresses for a long time. The influence of the radial gap width δ_H is investigated both by means of a prototype with a smaller diameter D-, as well as by a variant RG+ with a smaller diameter of the hub disc, but with the same blade diameter. Further variations are performed on the blade length (SO) and the blade angle (A60).

A list of the different variations is given in Tab. 5.2. The dimensions are listed as a percentage change from the basic design Fig. 5.2(a).

5.2 Hydraulic Experiments

Various prototypes are bench-tested to evaluate their hydraulic properties. Hydraulic efficiency, bearing stability, and characteristic pressure-flow curves can be determined based on the data obtained.

5.2.1 Experimental Setup

A schematic representation of the test bench used is illustrated in Fig. 5.3. The pump is connected to a tempered water tank with PVC pipes. The pressure difference is measured with two manometers located at a distance of approx. 30 cm upstream and downstream of the

Table 5.2: Variations of the impeller design.

Design	h_{bl} (%)	r_a (%)	δ_{fl} (mm)	$\beta_{bl,a}$ ($^\circ$)	Addressed Effect	n_{nom} (rpm)
B	100	100	0.65	90	base design	7885
B+	116	100	0.65	90	blade height	7775
B-	83	100	0.65	90	blade height	8055
A60	100	100	0.65	60	blade angle	8055
D-	100	95	1.15	90	impeller diameter	8270
RG+	100	100	1.15	90	radial gap	7825
SO	100	136	0.65	90	blade length	5635

pump nozzles. The flow measurement is carried out with a contactless flow sensor based on ultrasound. The system characteristic can be adjusted by a valve on the pressure side.

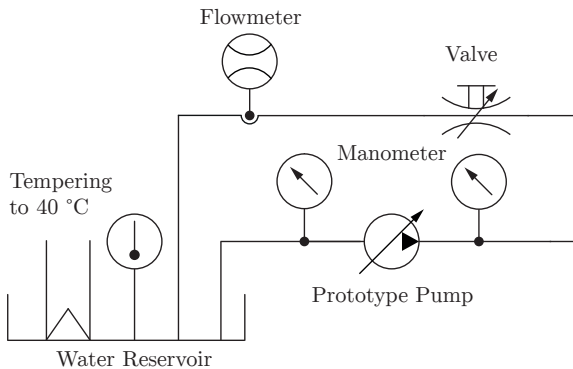


Figure 5.3: Schematic representation of the test bench used to determine the pump characteristics.

Water tempered at 40 °C is used as fluid. The viscosity of $\mu_{fl} = 0.7$ mPa is lower than that of blood. This mainly leads to lower friction losses inside the pump. Correspondingly, the power and the rotational speed required for blood will increase slightly. The efficiency will also be lower. This is exemplary illustrated for the base impeller design B

in Fig. 5.4. However, stability of the impeller increases with viscosity because the damping increases. The slight difference in fluid density ρ_{fl} can be neglected.

Tempering of the liquid prevents it from warming up due to pump losses. This guarantees a constant viscosity for the entire flow characteristics.

After the desired operating point has been reached, it is maintained for a few seconds to allow the transients to decay. The measurements of the flow and pump conditions are averaged over 10 measuring points.

5.2.2 Characteristic Curves

The characteristic curves of the impeller variations are shown in Fig. 5.4. All variations achieve the nominal operating point of 350 mmHg at 51/min. The pressure-flow curves also display a similar trend. This is due to the almost unchanged blade design between the prototypes.

The pump curves display a slightly unstable head-flow characteristic ($d(\Delta p)/dQ > 0$) in the range of low flow rates $Q < 21/\text{min}$. This, however, does not pose a problem since the process characteristic usually shows a higher flow dependency. During the conducted tests, no instabilities due to this positive slope could be detected.

Efficiency

The pump efficiency is calculated by

$$\eta_{\text{hyd}} = \frac{P_{\text{hyd}}}{P_{\text{mech}}}. \quad (5.6)$$

Here, P_{mech} is the work supplied to the rotor, which is calculated with voltage constant k_u according to

$$P_{\text{mech}} = k_u \omega \sum_{i=1}^3 I_{\text{drv},i}. \quad (5.7)$$

For the motor efficiency, two different formulations are introduced. One for the drive, η_{drv} , and the other for the entire motor including the

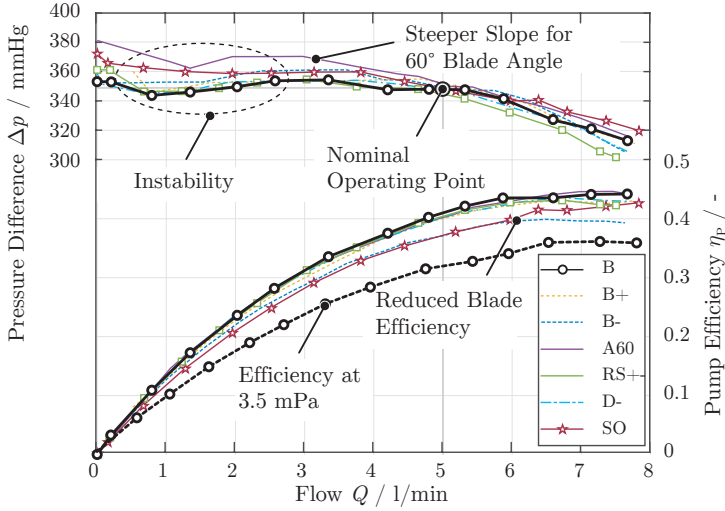


Figure 5.4: Pump characteristics and hydraulic efficiencies of all impeller variations at the nominal rotational speed. The nominal operating point is $Q = 5 \text{ l/min}$ at $\Delta p = 350 \text{ mmHg}$.

bearing, η_{mot} :

$$\eta_{\text{drv}} = \frac{P_{\text{mech}}}{P_{\text{mech}} + P_{\text{stat}} + P_{\text{cu,drv}}} \quad (5.8)$$

$$\eta_{\text{mot}} = \frac{P_{\text{mech}}}{P_{\text{mech}} + P_{\text{stat}} + P_{\text{cu,drv}} + P_{\text{cu,bng}}}. \quad (5.9)$$

The ohmic losses are calculated using the measured phase currents,

$$P_{\text{cu}} = P_{\text{cu,bng}} + P_{\text{cu,drv}} = \sum_{i=1}^3 R_{\text{bng},i} I_{\text{bng},i}^2 + \sum_{i=1}^3 R_{\text{drv},i} I_{\text{drv},i}^2, \quad (5.10)$$

where the two phase currents of each star-connected three-phase system are measured and the third is calculated with Kirchhoff's current law. The copper resistances R_{drv} and R_{bng} are measured at standstill and extrapolated to the operating temperature which is measured with a temperature sensor located inside the motor casing.

The iron losses in the stator, P_{stat} , are determined in advance. For this purpose, the losses at idling speed are determined during operation of the motor in air. It is assumed that these losses are only composed of copper and iron losses. Air friction losses are, therefore, also considered as iron losses. They are, however, negligible at the rotational speeds typical for pumping applications [105].

Since no measurements of the flow inside the pump head are possible, a breakdown of the pump losses is only possible by means of CFD simulations. Such a decomposition is listed for the basic design in Section 7.1.1.

The pump efficiency of most impellers is $\eta_P = 0.4$ and is shown in Fig. 5.4. Only the two impellers with extended blades (SO), which are only partially covered, and the one with reduced blade height (B-) display a lower efficiency ($\eta_P = 37.1\%$). For the SO design, this is due to strong turbulence at the open blade section, while for the impeller B-, higher blade channel friction and additional leakage losses occur above the front shroud disc.

Fig. 5.5 illustrates the efficiency of the motor η_{mot} and η_{drv} on the example of impellers B, RG+, and SO. The drive efficiency η_{drv} of SO is significantly lower than that of the other impellers. Due to its larger blade diameter, higher torque is required to generate the pressure difference. Since the motor has been designed for a smaller blade diameter, resulting copper losses are higher.

The difference between the drive efficiency η_{drv} and the motor efficiency η_{mot} is due to bearing losses. They are more significant at low flow rates.

Base design B achieves a motor efficiency of $\eta_{\text{mot}} = 86\%$ at the nominal operating point.

5.3 In Vitro Experiments

In vitro experiments are performed to analyse cell damage. For this purpose, bovine blood is pumped over several hours with the prototypes. The amount of the destroyed RBCs is regularly determined by red colour of the blood plasma.

The test setups and the procedures used to determine the plasma-free haemoglobin $H_{\text{b,pf}}$ are described below.

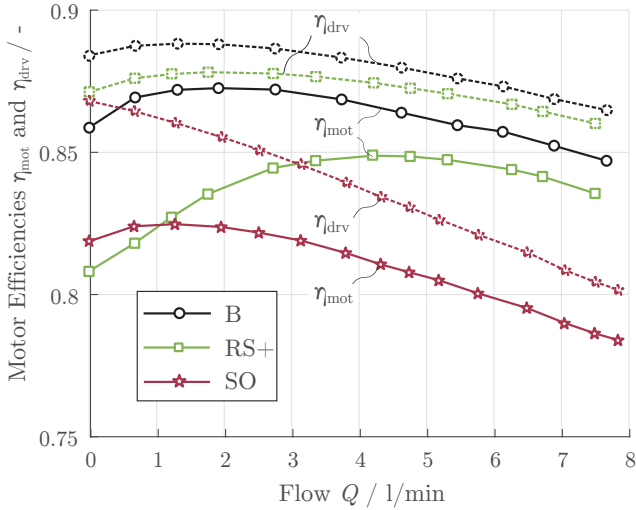


Figure 5.5: Drive and motor efficiency (drive and bearing), shown on the example of impellers B, RG+, and SO.

5.3.1 Experiment Setup

For the in vitro experiments, two different configurations are used. On the one hand, pumps are tested in a closed fluid circuit. The blood is drawn from a reservoir and pumped back into the tank, through tubes, at nominal flow and pressure. On the other hand, surface tests are carried out using a rotary shearing device consisting of a rotating ring rotor and a compressed air tank.

The two setups differ only in structure and minimally in evaluation. In particular, the procedure for determining cell damage remains unchanged.

Pump Circuit

The circuit illustrated in Fig. 5.7 is used to determine cell damage in the pump prototypes. It consists of a PVC blood reservoir with an inlet and an outlet socket. The pump is connected to the sockets with 3/8" soft PVC tubes. The pressure difference across the pump is measured with two manometers, 20 cm before and after the nozzles. The necessary

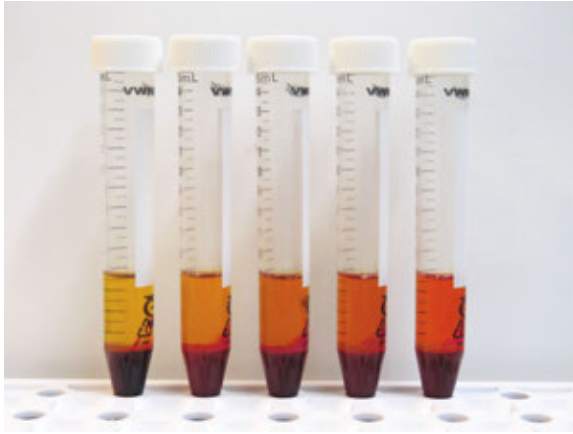


Figure 5.6: Discolouration of blood plasma with progressive haemolysis.

hydraulic resistance is set by a long PVC tube with 1/4" inner diameter and a manual clamp on the pressure side. The clamp is used for fine adjustment. Most of the pressure drop is caused by the PVC tube. The flow rate is measured with a contactless flow sensor. It is placed on the pressure side, 10 cm away from the reservoir inlet.

Both the flow rate and the pressure difference are checked regularly and kept within the ASTM tolerances ($Q = 5 \pm 0.25$ l/min, $\Delta p = 350 \pm 10$ mmHg) [106].

The circuits are constantly filled with a total circulation volume of $V = 700$ ml, and the circulating blood is tempered to 30°C by means of a heating spiral. The heating coil is immersed directly into the blood reservoir. The blood temperature is checked hourly.

The suction side tubing path is short (40 cm of a 3/8" tube) to avoid cavitation inside the pump. The average pressure drop at the pump inlet is -17 mmHg.

The setup is rebuilt for each experiment. Tubes and connectors are discarded after each test. The pump heads, reservoirs, and nozzles are cleaned and disinfected with hydrogen peroxide.

Haemolysis caused by the Circuit

The haemolysis caused by the circuit itself (tubes, clamps, connectors, reservoir, and nozzles) cannot be determined because a pump is always

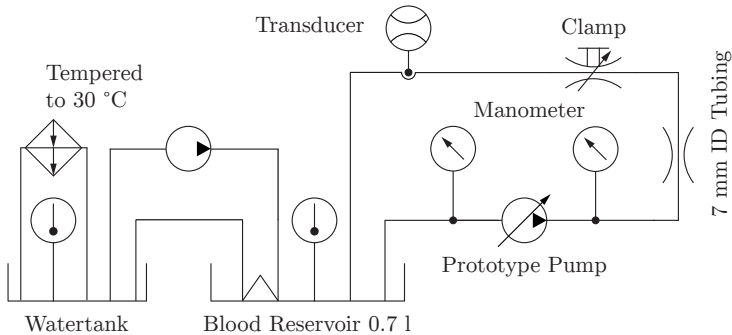


Figure 5.7: The fluid circuit used to determine blood damage in centrifugal pumps.

required to maintain the flow. In order to keep the bias small, investigations were carried out on modified circuits to identify and eliminate potential faults. This includes changes to the reservoir, tubes, and clamp.

Several tests with a pressure drop across clamps or long tubes were performed in parallel, and no significant difference was detected. The same conclusions are presented in [107]. Also, no difference could be established between attempts with an open PVC reservoir and with a closed blood bag. Only scratches and impurities on the reservoir inlet and outlet nozzles had adverse effects on haemolysis. The final blood reservoir used has two nozzles with 11 mm inner diameter. The nozzles are made of free-cutting stainless steel to prevent scratches.

Surface and Pressure Tests

Another setup is used to investigate the pressure and surface dependence of haemolysis. It consists of a reservoir tank that is placed directly on the bearingless motor. At the bottom of the tank, a surface-treated, disc-shaped rotor is magnetically levitated and driven. The shear forces create a vortex in the centre of the cup, which continuously mixes the blood volume.

Each container can be hermetically sealed and pressurized. A compressed air line supplies the tanks for this purpose. The blood temperature is controlled with immersed heating coils. A schematic diagram and a picture of the compressed air tank are shown in Fig. 5.8.

The desired roughness of the impellers is achieved by sandblasting.

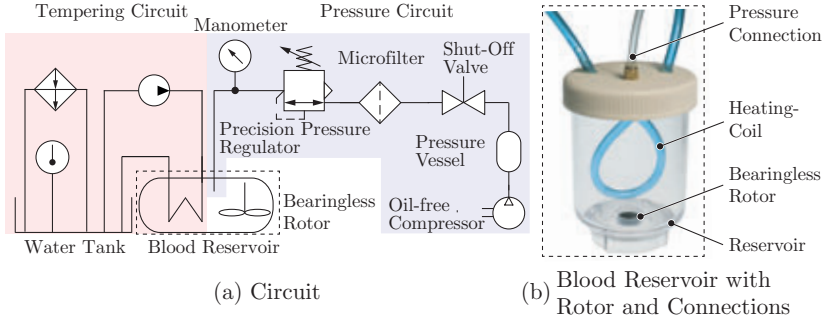


Figure 5.8: The setup used for surface and pressure tests.

Control Container

In addition to the actual test setups, a control container is filled with bovine blood and tempered. This blood is not exposed to any mechanical stress and serves to monitor spontaneous cell damage. Changes of $H_{b,pf}$ in this control sample indicate irregularities in the blood used. The results of such tests must be considered invalid.

5.3.2 Blood Collection and Preparation

The in vitro studies are performed with bovine blood. It has similar haemolytic properties to human blood [108] and it is easier to handle and procure.

The blood is obtained from a local slaughterhouse and mixed with 8000 IU/l anticoagulant immediately after slaughter to inhibit blood clotting. Less than an hour elapses between collection and the start of the experiments.

To keep the hydraulic properties of the blood constant across several experiments, it is diluted with phosphate-buffered saline solution (PBS) to an H_t of 30% and then filtered with a 38 μm filter.

Any equipment that comes into contact with blood is rinsed out with PBS beforehand.

5.3.3 Measurement of Plasma-Free Hemoglobin

To determine the progress of cell damage, samples of 5 ml are taken from the reservoir every hour and then centrifuged at 3000 g. The plasma is centrifuged a second time to ensure that no RBCs remain in the sample. Finally, 170 μ l are mixed with 2 ml of Drabkin's solution. This is a reagent containing potassium ferricyanide. It oxidizes haemoglobin to methaemoglobin and ultimately converts it to cyanhaemoglobin [109]. This forms a highly stable haemoglobin derivative and is therefore suitable for a reliable determination of H_b in whole blood [110, 111]. The method can be also used to determine $H_{b,pf}$ in the range of 1 – 2000 mg/dl [112].

Spectral Analysis

The haemoglobin concentration is determined photometrically using a calibration curve. Since cyanmethaemoglobin has an absorption peak at 540 nm [112], measurement at a single frequency is sufficient.

Calibration is performed with freeze-dried bovine RBCs [113] and demineralised water. The measured values are listed in Tab. 5.3 and can be approximated linearly. The Pearson correlation coefficient is $\rho_{\text{calib}} > 0.99$.

The blood used normally already has an $H_{b,pf}$ of approx. 20 mg/dl. The relative interpolation error is thus below 1%. The spectrum of the plasma is not changed by adding of Drabkin's reagent and can be compensated by an initial measurement. This makes concentration changes of 1 mg/dl $H_{b,pf}$ reliably measurable [114].

A Thermo Scientific GENESYS 30 UV/VIS spectrophotometer is used for the measurements.

5.3.4 Evaluation

To compare the experiments of different pumps, the normalized haemolysis index

$$NIH = \frac{dH_{b,pf}}{dt} \cdot \frac{V}{Q} \cdot (1 - H_t), \quad [NIH] = \text{mg/dl}, \quad (5.11)$$

is determined [115]. V represents the total blood volume in the circuit and Q the pump flow. The NIH is a measure of cell damage caused to an RBC per pass through the pump.

Table 5.3: Calibration values and approximation errors.

H_b (mg/dl)	Absorption	Approximate H_b (mg/dl)	e_{abs} (mg/dl)	e_{rel} (%)
0	0.0005	0.097	0.097	-
5	0.0079	4.628	0.372	7.43
10	0.0159	9.526	0.474	4.74
25	0.0413	25.078	0.078	0.31
50	0.0822	50.058	0.058	0.12
75	0.1234	75.283	0.283	0.38
100	0.1644	100.386	0.386	0.39
125	0.2046	124.999	0.000	0.00
150	0.2460	150.347	0.347	0.23
200	0.3274	200.185	0.185	0.09
150	0.4078	249.412	0.588	0.24

Since no flow rate can be assigned to the setup used for pressure and surface tests (Section 5.3.1), the average residence time is not known. It is assumed that mixing takes place uniformly and that all RBCs are exposed to the same loads. To determine the degree of damage, the temporal change of the $H_{b,\text{pf}}$ is normalized to the haematocrit value, analogous to the *NIH*, according to

$$HR = \frac{dH_{b,\text{pf}}}{dt} (1 - H_t). \quad (5.12)$$

The experiments are conducted for more than six hours, with hourly sampling. Based on seven samples from the entire test sequence, the rate of $H_{b,\text{pf}}$ is determined using the least-squares method.

Normalization to a Reference Pump

Because of the high variation of the bovine blood used, the prototypes are always tested parallel to a commercial pump, which serves as a reference. The *NIH* can be normalized with the aid of this pump,

$$RIH = \frac{NIH}{NIH_{\text{ref}}}, \quad (5.13)$$

where NIH_{ref} represents the NIH of the reference pump.

5.3.5 Variance

The results from various blood tests display a high variance. This is mainly due to the lipid content and the temperature of the blood used [116].

An empirical coefficient of variance $\hat{c}_{v,\text{CM}} = 0.485$ was determined for all experiments carried out in this thesis with the clinical pump CentriMag under identical conditions ($N = 28$). A value of $\hat{c}_{v,\text{B}} = 0.448$ was determined for the base prototype ($N = 16$).

However, if the RIH is used, the empirical coefficient of variance of the base design can be reduced to $\hat{c}_{v,\text{B},\text{RIH}} = 0.258$. Since the RIH is always formed within the same measurement series, i.e. with the same blood, the haemoglobin content H_b is thus normalized too.

By using a reference pump, the experimental effort can be significantly reduced.

5.4 CFD Implementation

The software CFX from ANSYS is used for the CFD calculations. In the following, the implementation, convergence criteria, evaluation methods, and the selection of the most suitable haemolysis model are presented.

5.4.1 Fluid Properties

For the simulations, it is assumed that blood is permanently in the range of constant viscosity. This simplifies the simulation and is justified by the high shear rates within the pump. Even if not all areas manifest such high shear rates, it can be assumed that the relaxation time of erythrocytes is relatively long compared to the rapid flushing and that the fluid cannot recover.

Therefore, a constant viscosity of $\mu_{\text{fl}} = 3.5 \text{ mPa}$ and a density of $\rho_{\text{fl}} = 1060 \text{ kg/m}^3$ is assumed.

Temperature changes are neglected for the simulation since the high-volume flow dissipates the heat loss advectively, and no heat conduction across the pump wall has to be considered.

5.4.2 Turbulence Model

The turbulent flow in the pump is described with the Reynolds-averaged Navier–Stokes equations (RANS equations). Fluctuations in density and viscosity are ignored.

The equations of the Reynolds stress tensor are closed by the $k - \omega$ SST model since this combines the advantages of the $k - \omega$ model in areas close to walls with those of the $k - \epsilon$ model [117].

The RANS equations are used only for the flow field. The additionally implemented transport equations for the haemolysis models are not averaged.

5.4.3 Meshing

Global Mesh Size

In order to determine the required number of nodes, a mesh independence study is carried out for the hydraulic properties of the pump and various haemolysis models. Stationary simulation of the base design B has been performed with different element sizes. Pressure difference and haemolysis index are averaged over the last 100 iteration steps. The resulting deviation from a simulation with a refined mesh of 15 million elements is listed in Fig. 5.9.

The pressure difference for a mesh size of 7 million cells deviates by less than 1% from a refined simulation with 15 million cells. Dependence of the different haemolysis models (single-stage and both double-stage models) on the mesh size can be similarly determined (see Fig. 5.9(b)). With a further refinement above 7 million elements, an error reduction of only 2% can be achieved. For haemolysis models that consider a threshold value of $\tau_{\text{th}} = 150 \text{ Pa}$ (Fig. 5.9(c)), an error of 3–4% occurs when 8 million cells are selected.

The independence of the mesh is accepted at 8 million cells, since further refinement leads to increased computing times, especially for transient simulations.

Inflation Layers

The velocity within the turbulent boundary layer can be divided into four zones. These are the viscous sublayer, in which the velocity changes linearly with the distance to the wall, the buffer region, the logarithmic layer, and the outer layer.

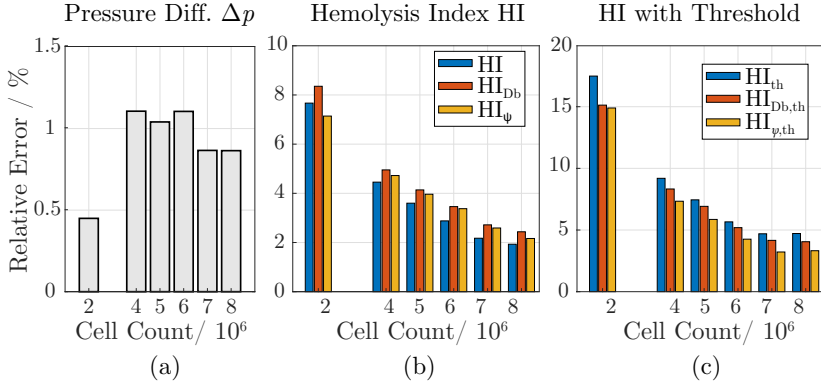


Figure 5.9: Error of the simulated pressure difference and haemolysis depending on the mesh size compared to a refined simulation with 15 million cells. (a) pressure difference, (b) haemolysis index of the single-stage and the two double-stage models, (c) haemolysis index of the threshold models.

As shown in Fig. 5.10, the velocity profile can be described by the dimensionless parameters

$$u^+ = \frac{u}{u_\tau} \quad \text{and} \quad y^+ = \frac{\rho y u_\tau}{\mu}. \quad (5.14)$$

Here,

$$u_\tau = \sqrt{\frac{\tau_w}{\rho}} \quad (5.15)$$

represents a reference velocity formed from the wall shear force τ_w and y measures the distance of the first cell to the next wall.

According to Schlichting and Gersten [118], the following applies to layers close to walls

$$u^+ = y^+ \quad \text{if} \quad 0 \leq y^+ < 5 \quad \text{viscous sublayer,} \quad (5.16)$$

$$u^+ = f(y^+) \quad \text{if} \quad 5 < y^+ < 70 \quad \text{buffer region,} \quad (5.17)$$

$$u^+ = \frac{1}{\kappa} \ln(y^+) + C \quad \text{if} \quad 70 < y^+ \quad \text{log-layer,} \quad (5.18)$$

where the following applies for the buffer layer and the parameters

$$f(y^+) = \frac{1}{\Lambda} \left[\frac{1}{3} \ln \frac{\Lambda y^+ + 1}{\sqrt{(\Lambda y^+)^2 - \Lambda y^+ + 1}} + \frac{1}{\sqrt{3}} \left(\arctan \frac{2\Lambda y^+ - 1}{\sqrt{3}} + \frac{\pi}{6} \right) \right] + \frac{1}{4\kappa} \ln(1 + \kappa B y^{+4}) \quad (5.19)$$

$$\Lambda = 0.127, \quad \kappa = 0.41, \quad C = 5. \quad (5.20)$$

The change from the buffer region to the logarithmic layer is often already set at $y^+ = 30$ [119].

To capture the velocity profile within the boundary layer, it must be resolved in detail or the so called wall functions must be used to model the behaviour of the boundary layer. For this purpose, inflation layers consisting of prisms are placed at all surfaces. If wall functions are used, the first node should be selected at $30 < y^+ < 200$, while it is aimed for $y^+ \approx 1$ if the boundary layer is to be resolved entirely.

In the present work, the boundary layer is resolved with $y^+ \approx 1$ to be able to calculate the shear forces close to wall more precisely. For the base design B, at the nominal operating point, this requires a first inflation layer of $5 \mu\text{m}$ thickness. The histogram in Fig. 5.10 depicts the distribution of the inflation prisms along the dimensionless wall distance y^+ .

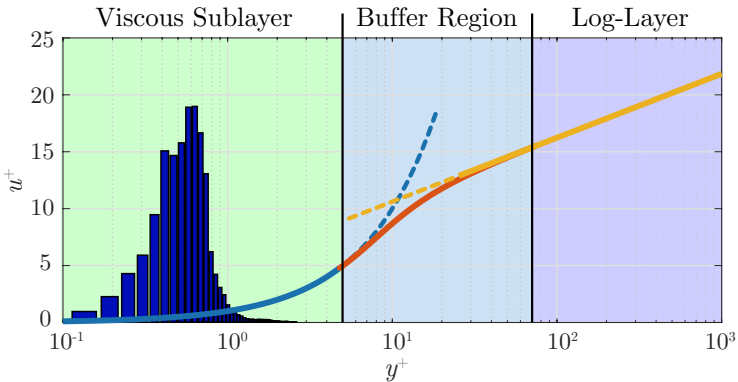
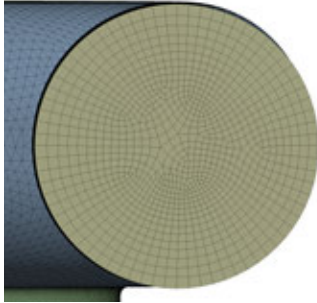
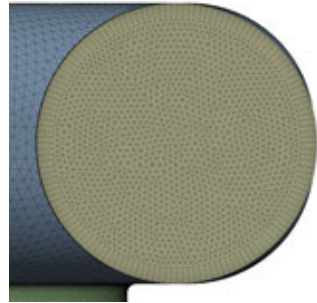


Figure 5.10: Distribution of the first inflation layer along the turbulent boundary layer.

All surfaces are meshed with 15 inflation layers. This ensures that the boundary layer is resolved with sufficient accuracy, especially since high shear forces and thus high haemolysis rates occur there. Fig. 5.11 illustrates the difference between the meshes with and without inflation layers (for reasons of clarity, only eight inflation layers are depicted).



(a) Automatic meshing without an inflation layer.



(b) Meshing with eight inflation layers in regions close to walls.

Figure 5.11: Mesh comparison of the pressure nozzle without (a) and with eight inflation layers (b) in the boundary layer.

5.4.4 Convergence Criteria

For simulations of the hydraulic properties, residuals of the momentum equation and mass conservation of $< 1 \cdot 10^{-4}$ are aimed for. The solution is considered to have converged as soon as the residual condition is met, and the change in pressure difference averaged over 1 impeller rotation is less than 1%.

For the simulation of haemolysis, a residual of $< 10_{\text{rms}}^{-4}$ is aimed at for the corresponding transport equations.

5.4.5 Initialisation

In this thesis, transient simulations are initialized with the help of two stationary simulations. First, a stationary simulation (frozen rotor) without haemolysis model is performed to obtain an estimate of the velocity and shear stress field. The solution serves to initialize a second stationary simulation, with implemented haemolysis models. The

results of this second simulation ultimately serve as an initialization for the transient simulation.

In this way, it can be prevented that unrealistically high shear forces, caused by incorrect initial conditions, lead to high source terms of the haemolysis transport equation. As a result, a significant increase of the convergence can be achieved.

5.4.6 Comparison of Haemolysis with Measurements

To compare the simulation results with in vitro experiments, the mass averaged haemolysis index \overline{HI} at the pump outlet is compared with the *NIH*. The following applies:

$$\overline{HI} = \frac{\int HI \cdot \dot{m} \, dA}{\int \dot{m} \, dA} = \frac{NIH}{H_b} \cdot \frac{1}{1 - H_t}, \quad (5.21)$$

where the integral is to be evaluated at the outlet cross-sectional area.

To evaluate the prototypes, however, the entire scalar field must be considered.

5.4.7 Implemented Haemolysis Model

To detect the critical points within the pump, only an Eulerian haemolysis model is suitable, which can be used to calculate a scalar field and find local maxima of cell damage.

For the implementation as well as for the parameter selection and the equivalent shear stress, a multitude of different data can be found. For this reason, the most suitable combination for the present work is determined based on a stationary CFD simulation of the base design B.

In order to assess the simulation accuracy, in the following it must often be referred to the results from Section 8.1.1 in advance.

Parameter Selection and Equivalent Shear

Since the parameters of the power law (4.11) vary greatly, four different parameter sets are implemented and compared with each other. The values are based on the works of Fraser et al. [95], Giersiepen et al. [70], Goubergrits and Affeld [68], and Heuser and Opitz [62]. These values can be found in Tab. 4.2.

As described in Section 4.3.4, there is also a great uncertainty about the equivalent stress to be used. In the following, the equivalent shear stresses proposed by Blutzweit τ_B are compared with the scaled von Mises stress $\tau_{\sqrt{3}}$,

$$\tau_B = \sqrt{\frac{1}{6} \sum_{i \neq j} (\tau_{ii} - \tau_{jj})^2 + \sum_{i \neq j} \tau_{ij}^2}, \quad \tau_{\sqrt{3}} = \sqrt{\frac{1}{3} (I_{\underline{T}}^2 - II_{\underline{T}})}. \quad (5.22)$$

All combinations are implemented in a stationary simulation with the single-stage haemolysis model from Section 4.3.3.

A comparison of the measured haemolysis values with simulated results shows that all combinations significantly overestimate haemolysis. The individual values of relative error are listed in Tab. 5.12.

Relative Error	Parameter Set			
	FR	HE	GG	GS
τ_B	2.3	3.1	25.4	633.4
$\tau_{\sqrt{3}}$	2.0	2.7	22.7	569.0

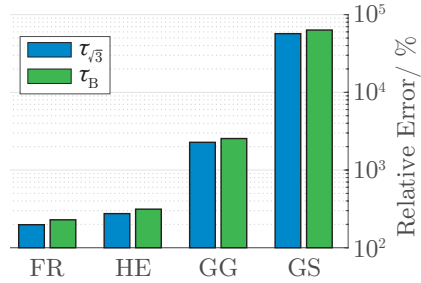


Table 5.4 & Figure 5.12: Relative error versus in vitro measurements of the different parameter sets for the single-stage model. Parameter sets: Fraser (FR), Heuser (HE), Goubergrits (GG), Giersiepen (GS).

While the parameters of Giersiepen combined with the equivalent stress τ_B are too high by a factor of 634, the deviation with parameters of Fraser and the equivalent stress $\tau_{\sqrt{3}}$ is only 197%. This is why, for further considerations, only this combination is pursued.

Implemented Models

Both the two double-stage models (Section 4.3.3) and the single-stage model (Section 4.3.3) are implemented and compared using a stationary simulation. It is shown that the single-stage implementation converges faster and therefore requires less computing power since only one transport equation must be solved instead of two.

Simultaneously, all variants are additionally assigned a threshold value of $\tau_{\text{th}} = 150 \text{ Pa}$ using the weighting function

$$w(\tau) = \frac{1}{2} \left(\tanh \left(k \frac{\tau - \tau_{\text{th}}}{\tau_{\text{th}}} \right) + 1 \right). \quad (5.23)$$

This means that only shear forces above the threshold lead to haemolysis. The haemolysis prediction is reduced accordingly. The weighting function implemented, with $k = 5$, is illustrated in Fig. 5.13.

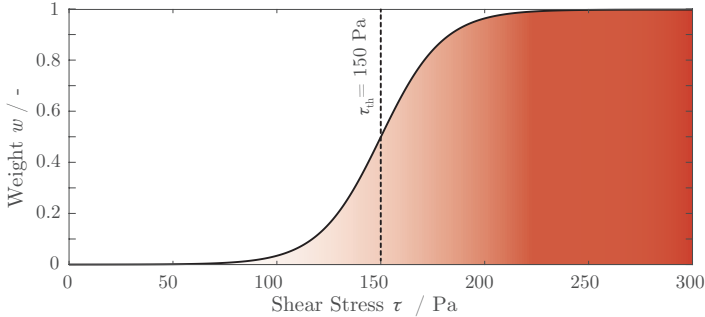


Figure 5.13: The implemented weighting function of the haemolysis rate according to equation (5.23) with a threshold value of $\tau_{\text{th}} = 150 \text{ Pa}$ and $k = 5$.

For the double-stage models, each haemolysis transport equation (equations (4.20) and (4.21)) is weighted, and not the dose or residence time. The implemented models are illustrated schematically in Fig. 5.14.

The deviations of the individual models from the mean value of 16 in vitro experiments are summarized in Tab. 5.5.

Since both double-stage models are able to account for cell hardening via the nonlinear time dependence of haemolysis, the simulated haemolysis rate is lower than predicted by the single-stage model. The double-stage model with time-dependent source term (DSR) exhibits the smallest deviation. Compared to the measured values, haemolysis is only overestimated by about 10%. However, the physical significance of this model is questionable, since cell hardening is only due to exposure time and not due to load on the cell. The double-stage model (DSD) based on a damaging dose with a threshold value of $\tau_{\text{th}} = 150 \text{ Pa}$ also delivers good results. It underestimates haemolysis by 18% in the considered simulation.

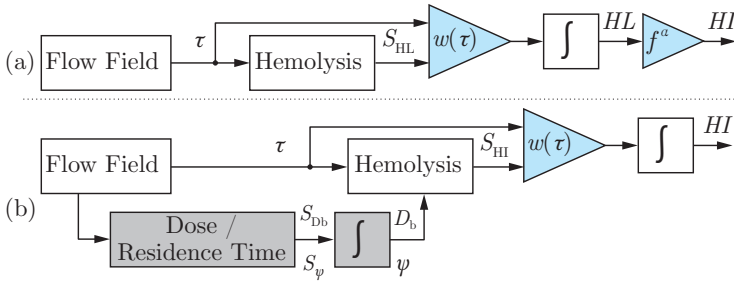


Figure 5.14: Schematic representation of the implemented haemolysis models. (a) single-stage model, (b) double-stage model. Each integrator represents a transport equation.

Table 5.5: Simulation results of haemolysis and its deviation from in vitro experiments. TH: Threshold value.

Implementation	Equations	$HI / 10^{-6}$	$e_{rel} / \%$
Experiment	(5.21)	1.37	0
Single-Stage (SS)	(4.14)	4.08	+197
Dose (DSD)	(4.21)	2.63	+92
Residence Time (DSR)	(4.20)	1.49	+9
SS with TH	(4.14)+(5.23)	2.23	+63
DSD with TH	(4.21)+(5.23)	1.12	-18
DSV with TH	(4.21)+(5.23)	4.76	-65
DSV with variable TH	(4.21)+(4.22)	0.49	-64

Sensitivity to Geometry Variations

The sensitivity of haemolysis models to changes in design parameters is of particular importance. To find the most suitable haemolysis model, the prediction must be checked by means of modified geometries. Even if the forecast of the absolute value is wrong, a model can be applied for optimization procedures if at least its trend matches with the measurements.

In the following, the relative haemolysis rate RIH of the impeller variations from Section 5.1.4 is determined by simulations in relation

to the base design B and compared with the measurement results. The results are listed in Fig. 5.15 for the various implementation models and impeller variations. Above the in vitro measurements, the p -value of a two-sided t -test is indicated between the individual variations and the base design B. The correlation coefficient between the simulation results and the measurements is displayed above the simulation results.

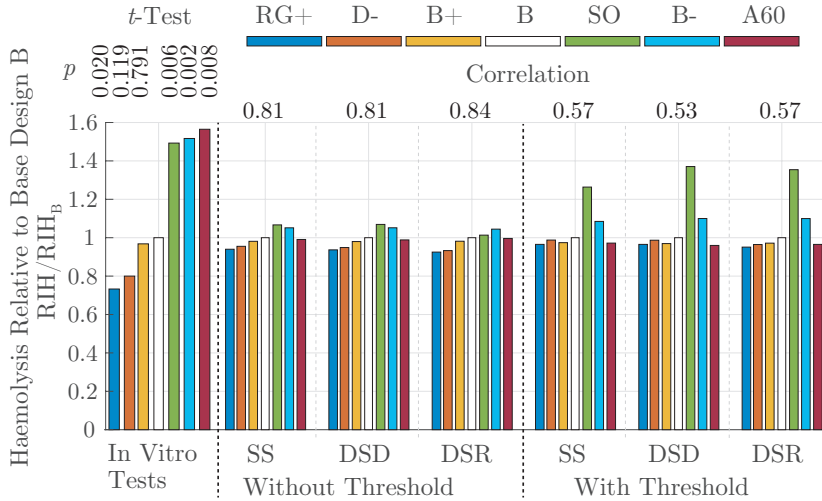


Figure 5.15: Sensitivity analysis of different haemolysis models based on the in vitro results of impeller variations. The results are sorted by ascending haemolysis rate of the in vitro measurements. The correlation values between the simulation results and the measurements are listed above the bars. The respective p -value is also given for the measurements in relation to the base design B.

A comparison of the in vitro experiments with the various simulation models shows that models without threshold values, in particular, display a high correlation of over 80%. For all models, the impeller with an outlet angle of 60° inflicts less cell damage than the base design. However, with a p -value below 1%, the credibility of the in vitro results is high. The clear difference between the simulation and the measurements is thus due to unmodeled effects, such as the adhesive seam between the impeller blade and the front shroud plate, tilting of the rotor, or damage to the impeller.

For all other designs, the simulation trends match well with in vitro measurements. However, the sensitivity of the simulations is considerably lower than that of the experiments.

Evaluation

With a suitable choice of the implementation model and the parameter set, haemolysis simulations can achieve predictions with deviations of only a few percent. The sensitivity of the haemolysis models also correlates with measurements but not all outcomes coincide. This is only conditionally satisfactory since one cannot solely rely on the simulations. Important effects such as surface roughness or unclean seams cannot be considered in the simulation.

Considering the above sensitivity analysis, the double-stage model based on a residence time performs best. The same applies for the absolute accuracy of the haemolysis prediction. For these reasons, further investigations are carried out with this model.

The values suggested by Fraser et al. [95] are used as parameters. The equivalent stress is formed with $\tau\sqrt{3}$.

5.4.8 Effects not taken into Account

Due to the complexity of the flow, the increased computational effort, and the low reliability of the haemolysis models, some effects cannot be considered by simulations. These are in particular:

- ▶ surface roughness,
- ▶ pressure-dependent influences,
- ▶ manufacturing tolerances,
- ▶ displacements of the rotor,
- ▶ tilting of the rotor,
- ▶ possible contacts between the rotor and the housing wall.

Accordingly, the simulations can only be used to explain and better understand certain effects.

6

Influence of the Surface on Haemolysis

In addition to the frequently investigated cell damage caused by shear stress, it is reasonable to assume that cell damage also depends on other factors. In this chapter, an estimation of individual influencing factors is carried out. It is assumed that cell damage is a function of the shear rate τ , the static pressure p , and the surface quality R_a ,

$$HR = HR(\tau, p, R_a). \quad (6.1)$$

In the following, the influences and the coupling between the individual parameters are to be determined.

Section 6.1 examines the dependence of the haemolysis rate on surface quality.

Dependency on the shear force is investigated in Section 6.2.

Dependence of the haemolysis rate on the static pressure and the coupling with the surface quality is presented in Section 6.3.

The test bench described in Section 5.3.1 is used for examinations. A rotor covered with plastic is magnetically suspended and rotates in the reservoir. The relative speed between the rotor and the housing walls causes shear forces, which lead to cell damage. The influence of the surface on haemolysis can be determined using rotors of different surface qualities. Besides, the test bench allows the static pressure in the vessel to be adjusted, and consequently the pressure dependence of haemolysis to be investigated as well.

In the following studies, experiments with the same blood are compared in order to reduce the variance.

The surface quality is subsequently characterized by the arithmetical mean deviation R_a . To give an impression of the surface profile at different R_a values, three microscopy images are given in Fig. 6.1. The images were recorded with a Zeiss LSM 880 confocal microscope.

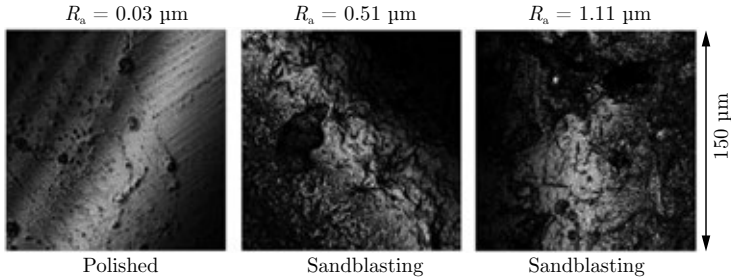


Figure 6.1: Microscope images of different surface qualities.

6.1 Influence of Surface Quality

In order to check the influence of surface quality on cell damage, in vitro experiments are carried out under atmospheric pressure. The shear rate in the radial gap is maintained at $\dot{\gamma} = 20\,900\text{ s}^{-1}$. Therefore, the Taylor number in the radial gap is $Ta \approx 1.25 \cdot 10^5$. Rotors with surface qualities between $R_a = 0.2 - 2.3\ \mu\text{m}$ are examined.

Thus, haemolysis is investigated as a function of surface roughness R_a at a given pressure and shear force,

$$S_{\text{HR},R_a} = \left. \frac{\partial \text{HR}}{\partial R_a} \right|_{p,\tau}. \quad (6.2)$$

The results are illustrated in Fig. 7.3.

The shear forces cause a base cell damage of $\text{HR} = 4.4\ \text{mg}/(\text{dl} \cdot \text{h})$. Up to a relatively rough surface of $R_a > 0.6\ \mu\text{m}$, the surface quality has little effect on haemolysis. For more irregular surfaces, however, cell damage increases rapidly. A roughness of $R_a = 1.22\ \mu\text{m}$ already leads to 1.3-fold haemolysis. At $R_a = 2.35\ \mu\text{m}$, a 2.6-fold haemolysis already takes place. With such a rough surface, surface effects dominate the base damage caused solely by shear forces.

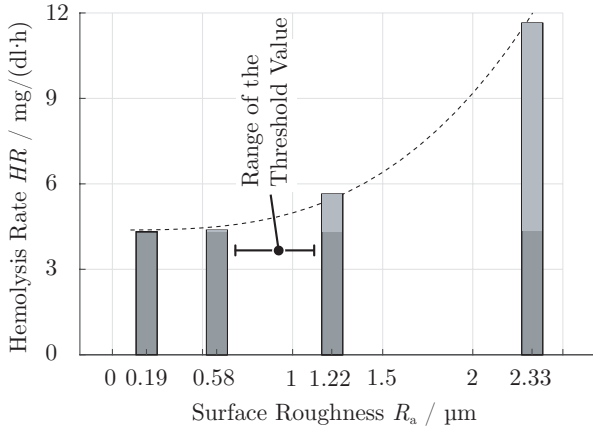


Figure 6.2: Influence of the surface quality on cell damage under atmospheric pressure and for the same manufacturing method.

Under atmospheric pressure, a rough surface of $R_a \approx 0.6 \mu\text{m}$ can be tolerated. Similar results for a shear rate of $\dot{\gamma} = 3750 \text{s}^{-1}$ were already obtained in [83].

The threshold value, above which cell damage increases significantly, is in the range $R_{a,\text{th}} = 0.6 - 1.2 \mu\text{m}$.

6.1.1 Influence of the Surface Structure

Although the R_a value is the most common parameter to describe a surface in the technical field, it is reasonable to assume that a simple value is not sufficient to characterise cell compatibility.

To emphasize the importance of the surface structure, further investigations are carried out under atmospheric pressure. For this purpose, two rotors are each processed differently so that they have similar R_a values. While the rotors R1 and R2 are sanded, R3 and R4 are sandblasted. The microscope images of these rotors are displayed in Fig. 6.3.

The rotors R1 and R3 have a mean roughness value of $R_a \approx 1.3 \mu\text{m}$ ($1.07 \mu\text{m}$ and $1.59 \mu\text{m}$, respectively). R2 and R4 are manufactured with $R_a \approx 3.76 \mu\text{m}$ ($3.75 \mu\text{m}$ and $3.61 \mu\text{m}$, respectively). The average maximum height of the profile, R_z , is also in a comparable range.

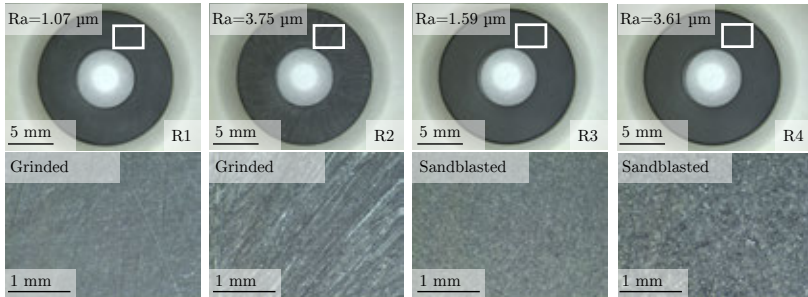


Figure 6.3: Influence of the processing method on haemolysis.

The results of the in vitro tests are listed in Tab. 6.1.

Table 6.1: Roughness values of the investigated rotors for determining the dependence on the machining method.

Rotor	Treatment	R_a (μm)	R_z (μm)	HR ($\text{mg}/(\text{dl} \cdot \text{h})$)
R1	grinding	1.07	5.79	6.28
R2	grinding	3.76	18.70	19.00
R3	sandblasting	1.59	8.33	3.39
R4	sandblasting	3.61	15.85	11.40

The sandblasted surfaces perform better than the sanded ones (despite a higher R_a value in some cases). Neither the R_a value nor the R_z value provide sufficient information about how much a surface contributes to cell damage. Even with almost identical R_a and R_z values, differences in haemolysis of more than 65% can be observed.

The course of the surface profile in Fig. 6.4 also shows no significant differences. The profile peaks are in the order of magnitude of the thickness of an RBC.

The methods used to assess surface quality are not sufficient to predict cell compatibility. With the help of detailed three-dimensional surface analyses, it might be possible to identify structures that indicate increased cell destruction. To do so, however, a considerably more extensive database is required.

For the following considerations, rotors with the same machining

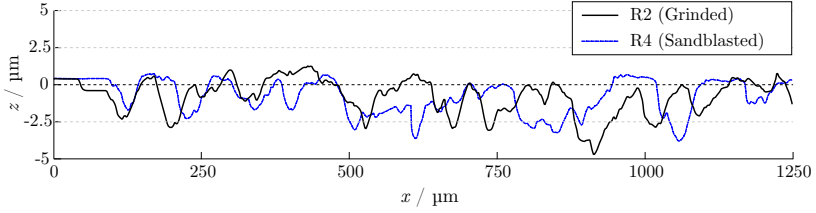


Figure 6.4: Surface profile along the circumferential direction of the rotors. Measured with a Mahr M 300 C.

process are used in order to draw conclusions about the influence of the surface.

6.2 Dependence on the Shear Rate

To investigate the influence of the shear rate, different rotors are tested at different pressure conditions for three hours at $\dot{\gamma}_1 = 24\,500\text{ s}^{-1}$ each, then for three hours at $\dot{\gamma}_2 = 26\,700\text{ s}^{-1}$. The sensitivity to the shear rate can be determined by the ratio of the two haemolysis rates

$$R_{\text{HR},\tau} = \frac{\text{HR}(\dot{\gamma}_2)}{\text{HR}(\dot{\gamma}_1)}. \quad (6.3)$$

Since the surface quality and the static pressure are also varied, the dependency of the haemolysis rate on these parameters can be determined.

The results of ten experiments are shown in Fig. 6.5. For all impellers, the sensitivity to the shear rate is positive ($R_{\text{HR},\tau} > 0$). On average, haemolysis increases by a factor of 2.26 with a 9% increase in rotational speed.

The sensitivity $R_{\text{HR},\tau}$ seems to be independent of the surface quality and the static pressure. At least their dependence is negligible in the area under consideration.

6.3 Dependence on the Static Pressure

As already shown in Section 4.2.2, an increased static pressure does not lead to haemolysis if blood is at rest, and no shear forces or relative

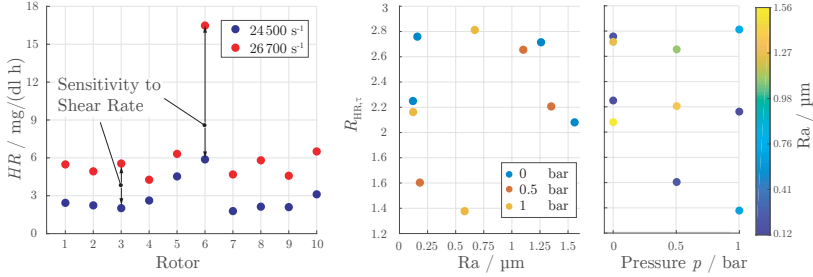


Figure 6.5: Dependence of the haemolysis rate on the shear rate. Cell damage increases with the increased shear rate.

velocities occur,

$$HR(\tau = 0, p, R_a) = 0. \quad (6.4)$$

Since the static pressure acts uniformly on the membrane of RBC from all sides, no resulting force arises. Thus, the membrane cannot be destroyed by such mechanical loads.

If a relative speed exists, higher pressure should, intuitively, lead to a higher mechanical load (analogue to static friction). It is expected that the sensitivity of the haemolysis rate with respect to pressure is positive,

$$S_{HR,p} = \left. \frac{\partial HR}{\partial p} \right|_{\tau, R_a} > 0. \quad (6.5)$$

To investigate this sensitivity, ten rotors with different surface qualities are tested at atmospheric pressure for three hours each, followed by another three hours at 1 bar. The shear rate is kept constant at $\dot{\gamma} = 26\,100\text{ s}^{-1}$.

The results are given in Fig. 6.6(a).

The haemolysis rate grows with increasing static pressure. For a smooth polished rotor, haemolysis increases by about 15% if the static pressure is increased by 1 bar. On rough surfaces ($R_a \approx 1.6\ \mu\text{m}$), haemolysis is 50% stronger for the same change in pressure.

6.3.1 Pressure Dependence of the Surface Effects

In Fig. 6.6(b), the ratio

$$R_{HR,p} = \frac{HR(p_2)}{HR(p_1)} \quad (6.6)$$

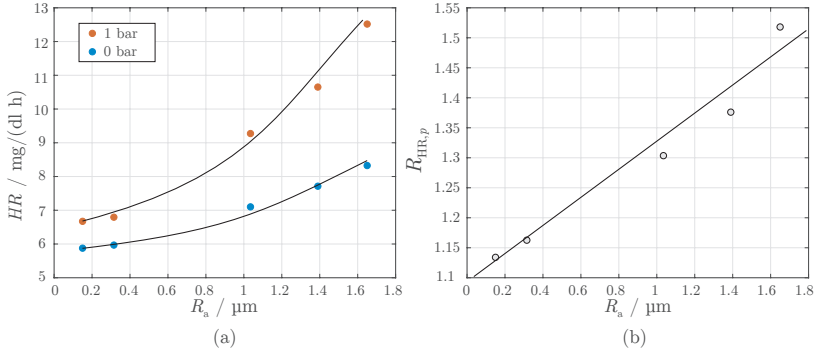


Figure 6.6: Dependence of the haemolysis rate on the surface quality and static pressure. (a) increase in cell damage with increasing pressure. (b) increasing influence of the surface effects with increased pressure.

is presented as a function of the surface quality R_a .

It is evident that the influence of the static pressure gains importance for rougher surfaces.

The higher cell damage due to surface quality with increasing pressure is because the blood cells in contact with the surfaces are pressed harder against them. Accordingly, the friction of the membrane increases.

The ratio $R_{HR,p}$ scales approximately linearly with the surface quality in the range considered. Therefore, a smooth surface is especially important in regions of high static pressure.

The increased haemolysis at a pressure of 1 bar and an R_a value of $0.2 \mu\text{m}$ shows that a mean roughness of $R_a \approx 0.4 \mu\text{m}$ is not sufficient for pumping applications at high pressure. This confirms the assumption by Takami et al. [85,86] (see Section 4.2.2).

6.4 Influence of the Surface Quality in Pumping Applications

The extent to which these findings play a role in the manufacture of a centrifugal pump for extracorporeal applications will be demonstrated through several in vitro experiments. Geometrically identical impellers and housings with different surface treatments are compared.

Fig. 6.7 shows the results of several haemolysis tests with vapor polished, milled, sanded, and roughened surfaces. For the investigated operating point with a pressure difference of 350 mmHg, the surface quality has a decisive influence on cell compatibility.

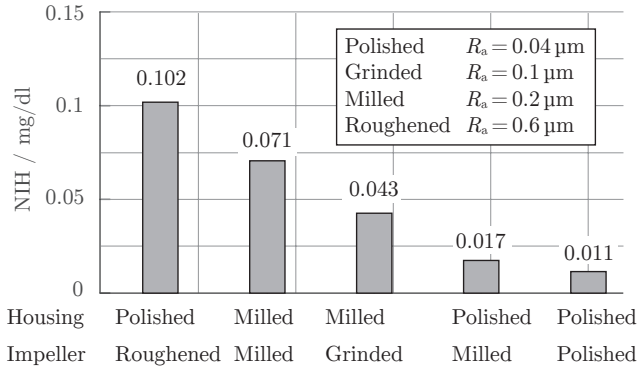


Figure 6.7: Influence of surface quality on cell damage during pump tests.

In particular, the surface of the housing tolerates hardly any roughness. Experiments with vapor-polished housings, for example, perform much better than merely milled versions. The difference between milled and polished impellers is less significant. This can be explained by the larger surface of the casing compared to the impeller (5000 mm^2 zu 2200 mm^2).

An exception to this is the test with vapor-polished housing and roughened impeller. This impeller exhibits a mean roughness of $R_a = 0.6 \mu\text{m}$. Such severe irregularities in the surface lead to a strongly increased cell destruction even on small surfaces.

The example of an impeller with a damaged blade on the pressure side illustrates the importance of a continuously smooth surface quality (see Fig. 6.8). Under the same test conditions, the impeller with a slightly eroded blade leads to an almost threefold increase in haemolysis.

6.5 Summary

The influence of the surface quality on cell damage was investigated based on in vitro studies. Under atmospheric pressure, no measurably

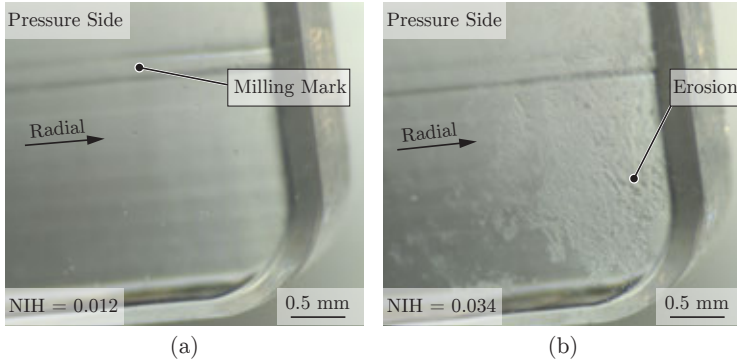


Figure 6.8: Microscopic image of the pressure side of two impellers (SO). (a) an undamaged, vapor polished blade. (b) a blade damaged by abrasion.

increased cell damage occurs if the surface has a mean roughness index below approximately $R_a = 0.6 \mu\text{m}$. Above this value, haemolysis increases rapidly.

If the threshold value is exceeded, the damage rate depends strongly on the surface structure. Simple measured values, such as the average roughness value R_a or the maximum height of the profile R_z , are not sufficient to characterise the relationship between haemolysis and surface roughness.

As already described in detail, cell damage also depends on the shear rate. For the investigated range of surface quality in the range of $R_a = 0.2 - 1.6 \mu\text{m}$ and a static pressure between 0 and 1 bar, no dependence of cell damage on the shear rate could be determined.

At an increased static pressure of 1 bar, the surface roughness causes more haemolysis. The influence grows with increase in surface roughness.

7

Flow Conditions

To gain a better understanding of the flow conditions within the pump, the hydraulic results from the CFD simulations are presented in the following chapter.

Section 7.1 gives an overview of the flow conditions and the shear force distribution within the pump. Some local properties of the flow are described in detail on the example of the base design B.

Building on this, the causes of haemolysis are determined in the next chapter based on geometric variations.

7.1 Overview

The results of a transient CFD simulation of the base design B are displayed in Fig. 7.1. The absolute velocity of the flow is color-coded. Arrows mark the approximate flow directions. For a more detailed description of the flow profile, the velocity field is also shown. In the top view of the blade channel, the relative velocity \vec{w} is illustrated instead of \vec{v} for this purpose. This makes the vortices around the blades better visible.

A large part of the mass flows from the inlet passes directly through the inlet eye into the blade channel of the impeller. Within the blade channel, the total pressure increases with radial distance. The fluid then flows over into the volute, where the velocity is significantly reduced. Here the fluid circulates and finally flows out through the discharge nozzle.

In addition to the main flow direction, significant leakage and secondary flow profiles can be identified. At the nominal operating point,

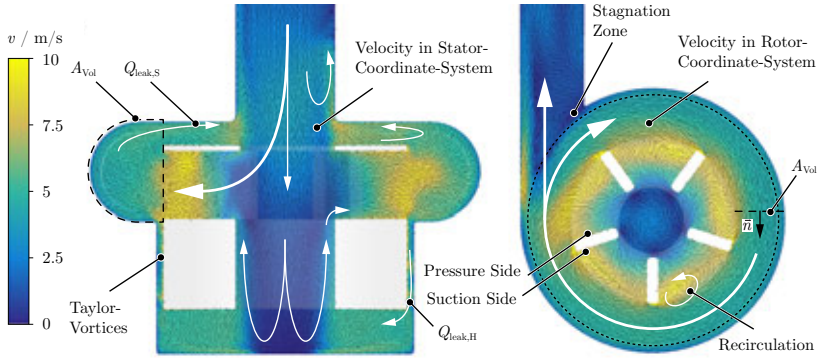


Figure 7.1: Overview of the flow conditions in the bearingless centrifugal pump.

the leakage Q_{leak} accounts for almost 60% of the nominal volume flow Q_{net} . It can be divided into a leakage along the front shroud disc $Q_{\text{leak,S}}$, and along the hub $Q_{\text{leak,H}}$.

The large fluid gap above the front shroud, in conjunction with the pressure difference across the blade passage, causes the leakage flow $Q_{\text{leak,S}}$. It amounts to 36.4% of the nominal flow rate. The leakage flow through the bearing gap $Q_{\text{leak,H}}$ amounts to 22.9%.

Due to the high blade angle, strong turbulences occur at the trailing edge. The vortices are flushed into the volute and decay there. The reduced pressure at the suction surface additionally leads to recirculations of the outflowing fluid back into the blade channel,

About 71% of the flow inside the volute,

$$Q_{\text{Vol}} = \int_{A_{\text{Vol}}} \vec{v} \cdot \vec{n} \, dA, \quad (7.1)$$

exits as nominal flow through the discharge nozzle. A fluid particle thus circulates on average 1.4 times around the volute until it reaches the outlet.

Due to the volute tongue, there is a stagnation zone in which the rotational speed of the fluid is divided, and the static pressure increases. This region is mainly responsible for the radial force acting on the impeller.

In the centre of the impeller, a weak vortex flow is formed, which

continues through the washout hole to the bottom of the housing.

7.1.1 Efficiencies

According to the above section, the volumetric efficiency is

$$\eta_{\text{vol}} = \frac{Q_{\text{net}}}{Q_{\text{bl}}} = \frac{Q_{\text{bl}} - Q_{\text{leak}}}{Q_{\text{bl}}} = 0.622. \quad (7.2)$$

In addition to the volumetric losses, losses in the form of friction occur at the sidewall gaps. They can be calculated by performing an energy balance on the impeller. The mechanical power supplied to the entire impeller can be calculated with

$$P_{\text{mech}} = \omega T = \omega \cdot \int_{\partial A_{\text{imp}}} f_{\varphi} r \, dA = 11.75 \text{ W}. \quad (7.3)$$

Thereof, only the portion

$$P_{\text{bl}} = Q_{\text{bl}} \Delta p_{\text{bl}} = 7.7 \text{ W} \quad (7.4)$$

is supplied, in the form of a pressure increase, to the fluid along the blade channel. The remaining power is dissipated as friction losses. The efficiency considering the sidewall losses can be determined by

$$\eta_{\text{R}} = \frac{P_{\text{bl}}}{P_{\text{mech}}} = 0.656. \quad (7.5)$$

The nominal flow rate Q_{nom} is supplied with the power $\eta_{\text{vol}} P_{\text{bl}}$. However, the directional changes, turbulences and accelerations happening between the blade outlet and the discharge nozzle lead to additional losses. The corresponding hydraulic efficiency can be calculated with

$$\eta_{\text{hyd}} = \frac{P_{\text{nom}}}{\eta_{\text{vol}} P_{\text{bl}}} = \frac{Q_{\text{nom}} \Delta p}{\eta_{\text{vol}} P_{\text{bl}}} = 0.882. \quad (7.6)$$

The overall efficiency of the pump can thus be determined as

$$\eta_{\text{P}} = \eta_{\text{R}} \eta_{\text{vol}} \eta_{\text{hyd}} = 0.36. \quad (7.7)$$

7.1.2 Shear Forces

Shear forces acting on the fluid can be roughly divided into two groups. On the one hand, the turbulence and directional changes of the external flow lead to shear forces between adjacent fluid layers. On the other hand, the strong speed reduction in the boundary layers also leads to high shear forces. Since the velocity gradient within the viscous lower layer is constant, these shear forces can be best described by means of wall shear forces. They are illustrated in Fig. 7.2 on the housing and impeller.

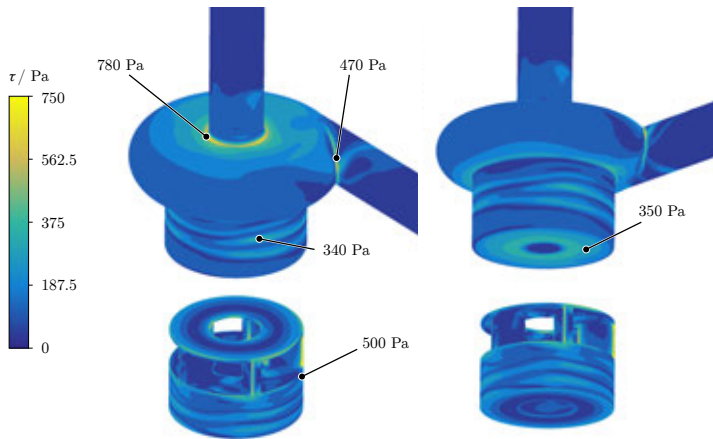


Figure 7.2: Wall shear forces on the housing and impeller walls.

On the housing, the highest shear stresses occur at the volute tongue and at the inlet nozzle. Furthermore, there are particularly high shear forces on the bottom surface and in the radial gap.

On the impeller, the shear forces are increased at the leading and trailing edges. High shear forces also occur at the outer corners of the shroud plate.

Local maxima at the inlet nozzle reach values of 780 Pa. On the impeller, the maximum is located at the trailing edge and reaches 500 Pa. The average value across the entire impeller surface is 110 Pa. The average value on the housing surfaces is 150 Pa (excluding the extension of the suction and discharge nozzles, introduced for the simulation). Additionally, Fig. 7.3 displays a histogram of the shear force distribution on the impeller and housing walls as well as in the fluid volume.

From Fig. 7.3 it becomes clear that the layers further away from the wall cause significantly lower shear loads.

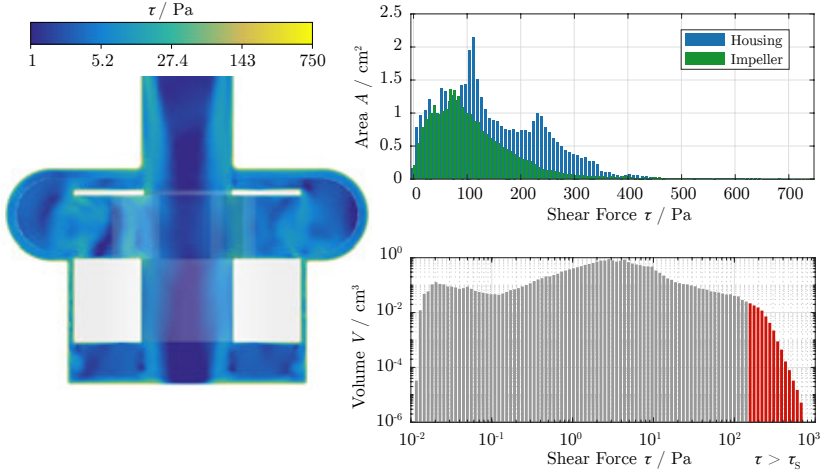


Figure 7.3: Overview of the shear force distribution in the bearingless centrifugal pump with logarithmic colour coding. The histograms show the shear force distribution on the pump surfaces and inside the fluid volume.

7.2 Separation into Control Volumes

The fluid volume of the pump is divided for the subsequent assessment of individual regions. For the sake of simplicity, the areas are subdivided coarsely. The terminology used can be found in Fig. 7.4.

7.3 Blade Channel

The total pressure of the fluid along the blade channel is increased from the leading to the trailing edge. As expected, strong turbulences occur at the blade inlet and outlet edges that lead to a reduction in pump efficiency (see Fig. 7.5). They come as a result of poorly designed blade geometry concerning fluid-dynamic efficiency.

Due to the radially increasing cross-sectional area in the blade channel, the fluid is rapidly decelerated, which leads to flow separation and

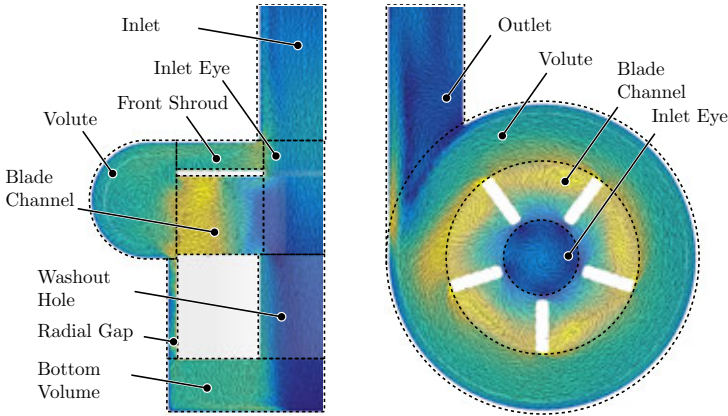


Figure 7.4: Division of the fluid volume into separate control volumes.

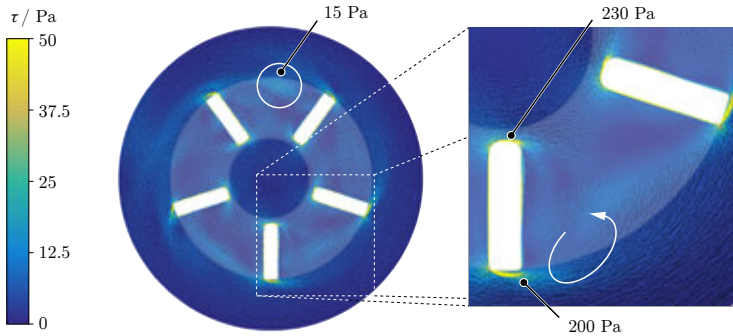


Figure 7.5: Top view of the shear forces in the blade channel. The relative velocity of the fluid is shown as a vector field.

backflows. This results in turbulence within the blade channel, which leads to a reduction of efficiency. The advantage of the high deceleration, however, is that a large part of the kinetic energy is converted into static pressure, thus avoiding high relative velocities within the impeller and downstream components.

High shear forces are limited to regions around the leading and trailing edges of the impeller. In the area of leading edge, the average shear stress is $\tau \approx 230$ Pa. At the trailing edge, it is about $\tau \approx 200$ Pa. Shear forces due to turbulence are significantly lower. The area marked in

Fig. 7.5 displays a maximum sheer force of only $\tau \approx 15$ Pa.

7.4 Radial Gap

A Taylor–Couette flow forms in the radial gap between the vertical housing wall and the rotating surface of the impeller. For the base design B at nominal rotational speed, the Taylor number

$$Ta = 4 \left(\frac{\omega^2 r_i^2}{r_a^2 - r_i^2} \right) \frac{(r_a - r_i)^4}{\nu^2} = 3.7 \cdot 10^5 > Ta_{\text{crit}} = 3416, \quad (7.8)$$

is dominant, where ν represents the kinematic viscosity.

Consequently, Taylor vortices are clearly formed [120]. They can be identified in Fig. 7.6 from the relative speed w .

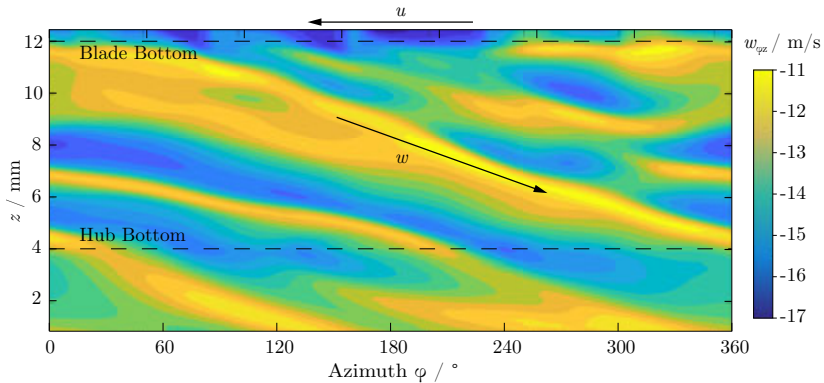


Figure 7.6: The formation of Taylor vortices in the radial gap and their effect on the shear forces.

In contrast to a pure Taylor–Couette flow, the radial flow is superimposed by an axial velocity component caused by the leakage. The detailed view from Fig. 7.7(a) shows that this leakage flow meanders around the Taylor vortices. The Taylor vortices are thus carried along with the flow. Therefore, the eddies do not run parallel to the circumferential direction, but diagonally along the radial gap (see the circumferential view in Fig. 7.6).

The Taylor vortices cause the fluid speed to increase relative to the impeller and housing walls. Accordingly, higher shear stresses occur around the eddies. The corresponding locations are marked in

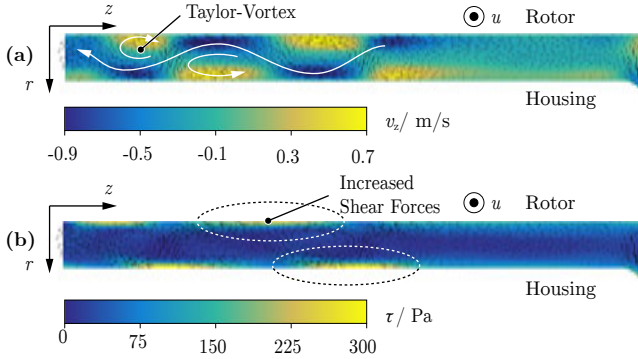


Figure 7.7: The formation of Taylor vortices in the radial gap and their effect on the shear forces.

Fig. 7.7(b). Compared to regions without vortices, shear stresses can be up to six times higher.

7.5 Bottom Volume

The flow conditions in the hub disc gap are illustrated in a cross-sectional view in Fig. 7.8. In the centre, below the washout hole, the velocity exhibits almost no circumferential component. With the increase in radial distance, however, the circumferential speed increases and reaches its maximum shortly before the inner radius of the hub disc, where $r \approx r_i$. Depending on the axial position, the tangential speed partly exceeds the circumferential speed of the rotor.

Close to the bottom of the housing, the tangential velocity profile corresponds approximately to a Rankine vortex, which, however, reduces strongly below the wash-out hole. The closer the observed layer is located to the rotating hub disc, the more the flow corresponds to that of a rigid body rotation.

A radially directed flow superimposes the tangential flow. Due to the pumping effect of the rotating hub disc, the fluid in the bottom clearance gap flows over wide areas radially outwards. Only in a thin layer at the bottom of the housing, the flow is directed inwards. In this area, in addition to the leakage flow $Q_{\text{leak,H}}$, the flow generated by the hub disc also flows back.

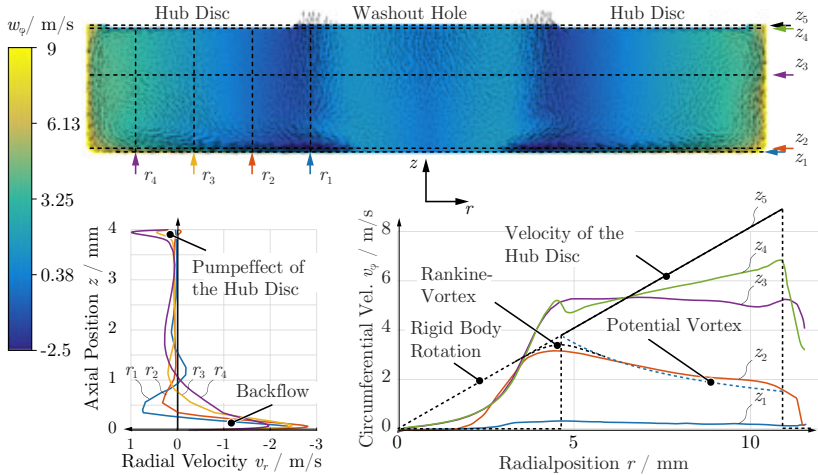


Figure 7.8: Flow conditions in bottom volume. The relative tangential speed is color-coded with respect to the hub disc.

7.6 Front Shroud Gap

The volume above the impeller differs from the bottom volume in that the leakage is significantly higher. The flow conditions are displayed in Fig. 7.9. The radial flow component is colour-coded.

Here, the rotating front shroud disc forces the fluid to flow radially outwards as well. The return flow takes place in a thin layer just below the housing lid.

Due to the different flow directions on the outside of the impeller, vortices are created in the volute.

The suction effect of the blade channel also causes turbulence in the inlet eye. In the area of the suction nozzle, there are partial backflows towards the pump inlet.

7.7 Washout Hole

The washout hole alone would correspond to a border case of a Taylor–Couette flow, with an infinitesimally small inner cylinder and rotating outer wall. Accordingly, a velocity profile that is distinctive in the

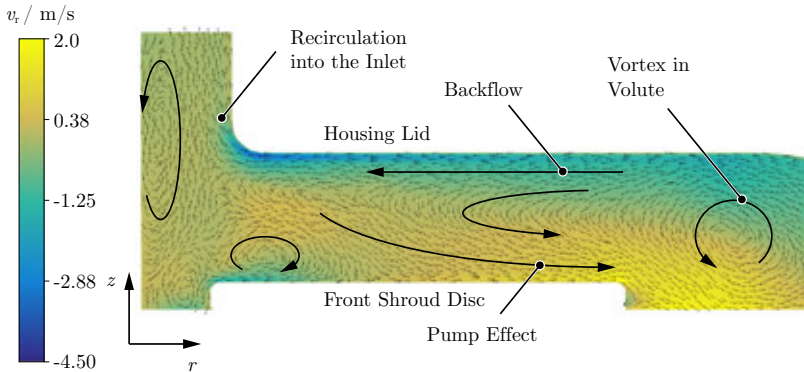


Figure 7.9: Flow in the front shroud gap.

circumferential direction and rotation-free would be expected,

$$\vec{v}_\varphi = \omega r \vec{e}_\varphi. \quad (7.9)$$

Such a rigid body rotation does not lead to any shear forces within the fluid.

As can be seen in Fig. 7.10, the actual flow differs significantly from these idealized considerations.

Due to the turbulent flow conditions, the increase in circumferential velocity happens in a narrow layer near the rotating wall (see Fig. 7.10(a)). The deviation from a rigid-body rotation is highest near the mean radius.

In addition, the leakage flow $Q_{\text{leak,H}}$ leads to a superposition of the axial flow in the washout hole. The impulse of the inflowing axial flow pushes the backflowing leakage to the outer walls. The prevailing axial velocity profile deviates significantly from a pure pipe flow. In particular, the backflowing fluid leads to high relative velocities on the impeller wall.

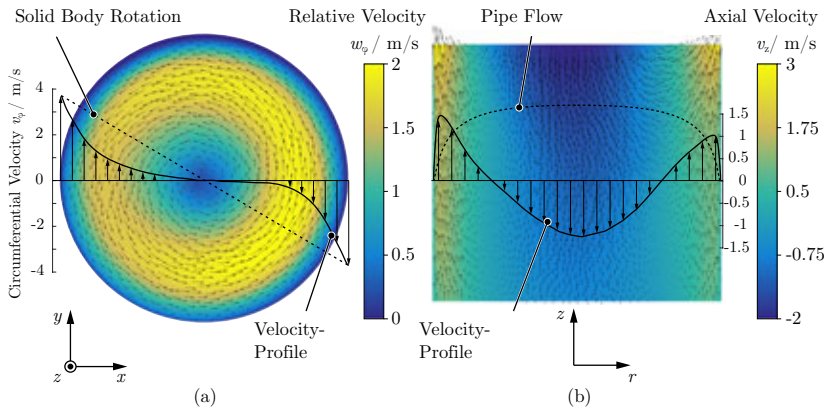


Figure 7.10: Velocity distribution in the washout hole. (a) top view with the colour-coded relative velocity in the circumferential direction and the velocity profile of the tangential flow. (b) sectional view with the colour-coded axial velocity and the velocity profile.

8

Haemolysis in the Bearingless Pump

In the following chapter, the cell damage that is induced by shear forces in the bearingless pump is examined. For this purpose, the implemented CFD simulations are evaluated in detail and compared with in vitro experiments. The correlation between the different haemolysis models and in vitro experiments has already been demonstrated in Section 5.4.7.

The results of all in vitro experiments are presented in Section 8.1 to provide an overview.

Section 8.2 shows the distribution of haemolysis within the pump and regions of critical shear stress on the example of the base design B.

Finally, Section 8.3 deals with the examined parameters individually. These are, namely, the radial gap, the bottom volume, the blade height, the blade angle, the blade length, and the rounding at the inlet nozzle. Simulations are illustrating how the flow and cell damage change due to geometry variation.

8.1 Overview of the In Vitro Experiments

Before the damage mechanisms in the pump are discussed in detail, the in vitro results of the individual prototypes are presented below. This illustrates how significant the influence of individual parameters is on cell damage. In the following sections, the reasons are determined with the help of CFD simulations.

8.1.1 Cell Damage

For all designs from Section 5.1.4, in vitro experiments with bovine blood were conducted. The exact experimental conditions can be found in Section 5.3. The results are listed in Fig. 8.1.

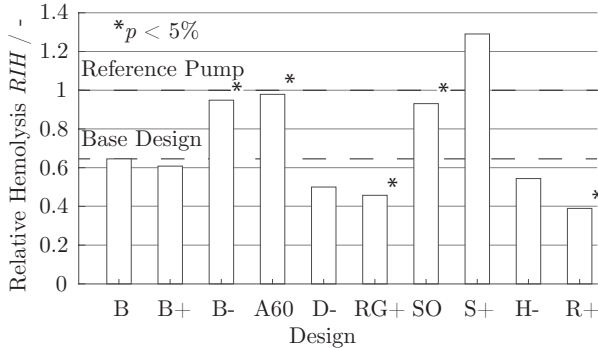


Figure 8.1: Results from the in vitro experiments for all manufactured prototypes. Results with a p -value below 5%, compared to the base design B, are marked with an asterisk.

Compared to the base design B - which already shows a 35% reduction in cell damage with respect to the reference pump - cell damage can be further reduced by

- ▶ increasing the blade height (B+),
- ▶ widening the radial gap (D- and RG+),
- ▶ reducing the bottom volume (H-),
- ▶ or enlarging the inlet fillet radius (R+).

Cell damage worsens when: the blade height (B-) is reduced, the outlet angle is reduced to 60° , a semi-shrouded impeller with blades protruding into the volute (SO) is used, and the fluid gap above the front shroud disk (S+) is increased.

The best results are achieved with a widened radial gap (RG+) and a rounded inlet port (R+). These pumps cause half as much haemolysis as the reference pump.

8.2 Cell Damage Distribution

A snapshot of the haemolysis distribution within the pump is given in Fig. 8.2. Haemolysed blood accumulates primarily in the bottom volume. At the same time, new, undamaged blood flows in from the inlet. The vortex in the centre of the pump causes the two regions to mix in the washout hole.

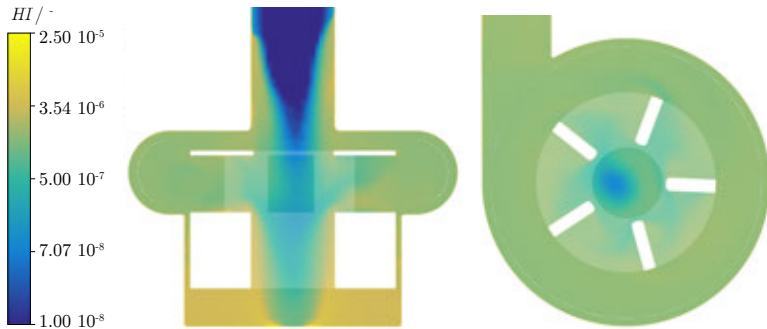


Figure 8.2: Distribution of the haemolysis index HI in the bearingless centrifugal pump. Logarithmic scale.

The haemolysis index HI increases as the blood flows through the blade channel. On the one hand, this is due to the destruction of cells in the blade channel and, on the other hand, due to the haemolysed blood flushed back through the washout hole.

For the further investigation of cell damage, however, it is not the degree of haemolysis that is of interest, but its temporal change. The change provides information on how quickly the RBCs are destroyed in the affected regions. A cross-sectional view of these damage sources S_{HI} is illustrated in Fig. 8.3.

About 50% of the haemolysis sources are located in the main flow path, such as the blade channel, suction nozzle, outlet, and the volute. The remaining haemolysis takes place in the sidewall gaps.

This illustrates how important the design of the sidewall gaps is compared to the main path. Especially since the main flow cannot be significantly influenced without changing the characteristic of the pump.

Table 8.1 lists the distribution of the haemolysis rate S_{HI} related to the individual fluid volumes from Section 7.2.

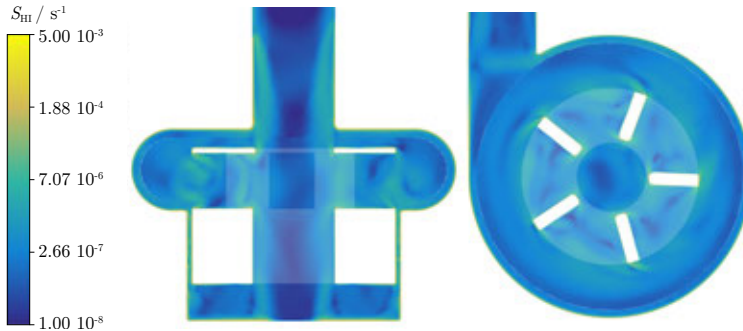


Figure 8.3: Distribution of the source term SHI. Logarithmic scale.

Table 8.1: Proportion of total cell destruction and destruction density of the individual regions.

Region	Volume cm ³	Damage Rate m ³ /s · 10 ⁻¹²	Damage Density 1/s · 10 ⁻⁶
Inlet	2.58	7.78	3.02
Outlet	2.51	5.71	2.27
Washout Hole	0.48	0.93	1.93
Inlet Eye	0.50	0.82	1.62
Radial Gap	0.37	28.17	76.76
Bottom Volume	1.69	23.11	13.68
Blade Channel	1.55	8.35	5.39
Front Shroud	0.65	18.59	28.69
Volute	4.65	44.25	9.51

8.2.1 Critical Shear Stress Regions

Locations exceeding the critical shear stress of $\tau_{th} = 150$ Pa are highlighted in Fig. 9.1. They are limited to regions close to walls.

Significantly increased shear forces occur at the transition of the inlet nozzle into the suction mouth, and at the leading and trailing edges of blades. Further such regions are located in the radial gap, at the bottom of the housing and on the volute wall.

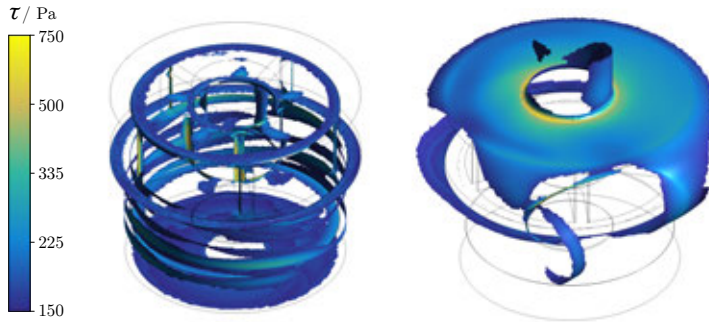


Figure 8.4: Areas with critical shear stresses ($\tau > \tau_{th}$). Logarithmic scale.

Relative to the priming volume of the prototype, only 0.5% of the fluid volume is exposed to critical shear loads (cf. Fig. 7.3).

8.3 Influence of the Geometry

In the following section, the influence of the investigated impeller and housing variations will be discussed in detail. Their influence is shown on both the flow and cell damage.

8.3.1 Radial Gap

As already explained in Section 7.4, the flow in the radial gap has distinct Taylor vortices. In addition to higher shear stress on the walls, they lead to higher source terms of haemolysis. The distribution of the S_{HI} is illustrated in Fig. 8.5(a). Here, haemolysis also takes place almost exclusively in regions close to the wall.

Despite the small volume, approx. 20% of the total cell damage takes place in the radial gap. It is the area with the highest damage density. This is due to the high shear rates and the comparatively long residence time. The occurrence of Taylor vortices increases, in addition to the shear forces, the residence time and thus complicates the evaluation.

In order to reduce the cell destruction in the radial gap, it can either be enlarged or reduced in size. The consequences of this will be considered below.

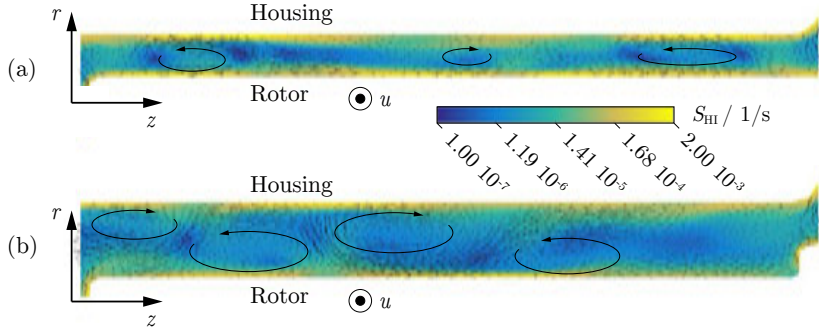


Figure 8.5: Distribution of haemolysis sources in the radial gap for the base design B and the widened radial gap (RG+).

Neglecting the Taylor vortices and the leakage flow, the following applies to the velocity distribution in the radial gap [99]

$$v_\varphi = Ar + \frac{B}{r}, \quad A = \omega \frac{-\eta^2}{1 - \eta^2}, \quad B = \omega r_{\text{rot}}^2 \frac{1}{1 - \eta^2}, \quad (8.1)$$

with

$$\eta = \frac{r_{\text{rot}}}{r_{\text{stat}}}, \quad (8.2)$$

where r_{rot} and r_{stat} represent the rotor and housing radius, respectively.

Accordingly, the shear forces are given by

$$\tau_{r\varphi} = \mu_{fl} r \frac{\partial}{\partial r} \left(\frac{v_\varphi}{r} \right) = -2\mu_{fl}\omega \frac{r_{\text{rot}}^2 r_{\text{stat}}^2}{r_{\text{stat}}^2 - r_{\text{rot}}^2} \frac{1}{r^2}. \quad (8.3)$$

The maximum

$$\tau_{\text{max}} = \tau_{r\varphi}(r = r_1) = -2\mu_{fl}\omega \frac{1}{1 - \eta^2} \quad (8.4)$$

occurs on the impeller surface.

The radial gap would have to be reduced from $650 \mu\text{m}$ to approx. $130 \mu\text{m}$ to avoid Taylor vortices. According to equation (8.4), this increases the maximum shear force by a factor of 4.7. With a haemolysis dependence on $\tau^{2.4}$, this results in an approximately 40-fold increase of the damage density. Although the radial gap volume decreases by a factor of about 5, it does not justify the increased source terms. The already high cell destruction would thus be significantly intensified.

The only option left is to expand the radial gap. According to equation (7.8), this increases the Taylor number. As a result, Taylor vortices cannot be avoided.

To investigate the actual influence, prototypes with a radial gap twice as large as the base design B were produced. The radial gap volume is thus increased by a factor of 1.7. At the same time, the theoretical shear forces (while neglecting Taylor vortices) are reduced to 56%.

The different distribution of haemolysis sources for both variants is shown in Fig. 8.5. As expected, the Taylor vortices increase. Due to the wider radial gap, the leakage flow $Q_{\text{leak,H}}$ also increases by about 55%, which shortens the residence time. The boundary layer thickness remains virtually unchanged, which means that a smaller proportion of the leakage flow is exposed to the high shear forces near the wall.

In the in vitro experiments, a widened radial gap leads to a strong reduction of cell destruction. The reduced rotor diameter (D-) reduced haemolysis by 20%. The widening of the radial gap, with constant blade diameter (RG+), reduced it even by 25%.

8.3.2 Bottom Volume

A large part of the haemolysis in the bottom volume is generated at the bottom of the housing, below the hub disk (see Fig. 8.6(a)). In this area, the circumferential speed v_φ increases rapidly with increasing distance z from the wall. The shear forces are correspondingly high. Since most of the flow is directed in the circumferential direction, the residence time is also long.

In the centre of the impeller, the axial flow of the washout hole hits the bottom of the housing. The peripheral speed of the fluid is correspondingly low (see Section 7.5). This means that almost no haemolysis takes place below the washout hole.

Two variations were manufactured, tested, and simulated to investigate the influence of the axial gap underneath the hub disk. For the variation H-, the axial gap was reduced by half, Fig. 8.6(b). This reduced the bottom volume to 0.836 cm^3 .

The total damage rate in the bottom volume,

$$S_{\text{BV,tot}} = \int_{\text{V,BV}} S_{\text{HI}} dV, \quad (8.5)$$

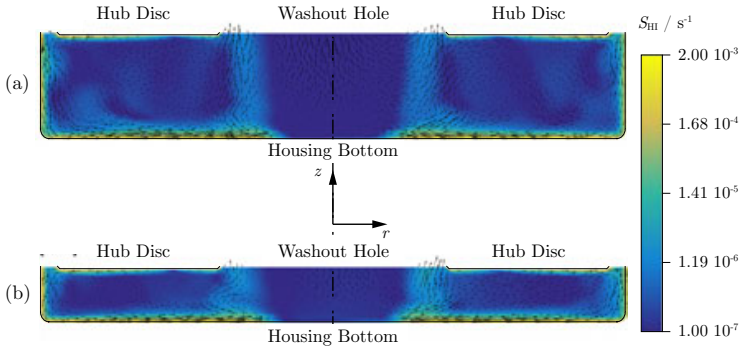


Figure 8.6: Distribution of the haemolysis sources in the bottom volume for the base design B and for the design with reduced bottom volume (H-).

remains almost unchanged ($23.34 \cdot 10^{-12} \text{ m}^3/\text{s}$ to $22.44 \cdot 10^{-12} \text{ m}^3/\text{s}$). The damage density doubles accordingly.

The leakage flow $Q_{\text{leak,H}}$ also remains almost unchanged (1.16 l/min), since a large part of the pressure drop takes place across the radial gap and along the washout hole. Accordingly, the residence time spent in the bottom area is reduced from 87.6 ms to about half (43.2 ms). By reducing the hub gap, haemolysis in the bottom volume should thus be reduced to about 60% ($HI \propto t_{\text{exp}}^{0.7762}$).

In the in vitro experiments, the reduced bottom volume achieved 25% less haemolysis than the base design B. It can be assumed that the axial movement due to the axial thrust leads to disturbances of the boundary layers in the bottom volume, generating more haemolysis.

8.3.3 Blade Height

Velocity triangles of the flow can be influenced by changing the blade height. For example, an increase in blade height leads to lower meridional velocities, which in turn leads to a large proportion of the kinetic energy to be converted into static pressure inside the blade channel. Accordingly, the relative speeds and thus also the wall forces in the blade channel can be reduced. The lower meridional velocity, however, increases the residence time. The reduced distance between front shroud plate and the housing lid also has a negative effect on haemolysis. If the size is too small, this will cause the boundary layers on the cas-

ing and the impeller to unify and to cause increased shear forces (see Section 3.3.2).

Since the change of the blade height is coupled with the change of the shroud gap, a prediction of the haemolysis property cannot be derived easily. For example, a larger gap generally leads to lower shear loads for the same rotational speed. However, as the leakage flow increases, the volumetric efficiency of the pump is reduced simultaneously, which would call for an increased rotational speed. This would, in turn, lead to higher shear forces, especially in the radial gap, and thus to more serious cell damage.

The strong coupling of shear forces, residence time, and rotational speed does not allow a simple prediction of the cell compatibility. It is imperative to resort to simulations and experiments.

In order to better understand and present the relations, three different blade heights (prototypes B, B+, and B-) are examined in the following, with otherwise same geometry. The CFD results are illustrated in Fig. 8.7.

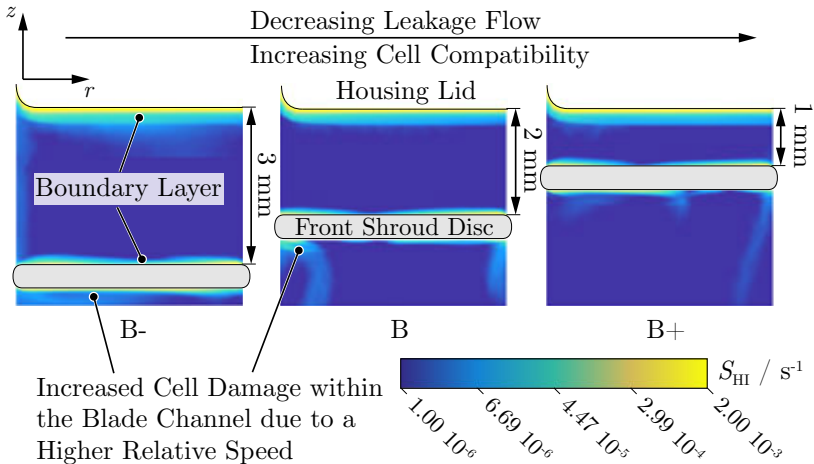


Figure 8.7: Change of the haemolysis source term with increasing blade height.

By increasing the blade height, the axial gap above the shroud is reduced. Shear forces are thus expected to increase. However, as can be seen from the simulation results of the impeller B+ (Fig. 8.7 right), the

reduced distance does not yet cause the two boundary layers to unify. At the same time, the volumetric efficiency of the pump is improved, thus requiring a lower rotational speed (7775 rpm instead of 7885 rpm).

Since *in vitro* experiments exhibit no significant improvement in haemolysis for increased blade heights, it can be assumed that the two effects mostly compensate each other.

A reduction of the blade height, however, leads to a significant increase in haemolysis (by 50% compared to the base design B). The wider axial gap increases the leakage flow, which is why a higher rotational speed is required (8055 rpm instead of 7885 rpm). The shear forces in the sidewall gaps increase as a result. Cell damage in the blade channel also increases. An increase of the cell destruction is especially visible near the leading edge (see left part of Fig. 8.7).

The *in vitro* results of the S+ design with a higher front shroud gap, but unchanged impeller, also show that haemolysis tends to increase when the gap is enlarged. The shroud gap should, therefore, be chosen as small as possible, but in such a way as to ensure that the boundary layers do not unify.

8.3.4 Blade Angle

The blade outlet angle is probably the most important parameter when designing a hydraulically efficient pump. Industrial constructions hardly deviate from the typical $20 - 25^\circ$. For the cell-friendly transportation of blood, however, the efficiency is secondary.

Although a pump with low blade angles exhibits less turbulence losses, the required circumferential speed per pressure difference is relatively high. For the pump under investigation, a curved impeller with an outlet angle of 22.5° , at the nominal operating point, requires a 5% higher circumferential speed (see Fig. 8.8).

The steeper blade angle reduces the rotational speed and thus the shear forces in the sidewall gaps. This is a crucial point to keep haemolysis to a minimum. The lower efficiency and the resulting turbulence must be tolerated.

8.3.5 Blade Length

By extending the blade beyond the shroud diameter (prototype SO), the required rotational speed can be significantly reduced. The shear

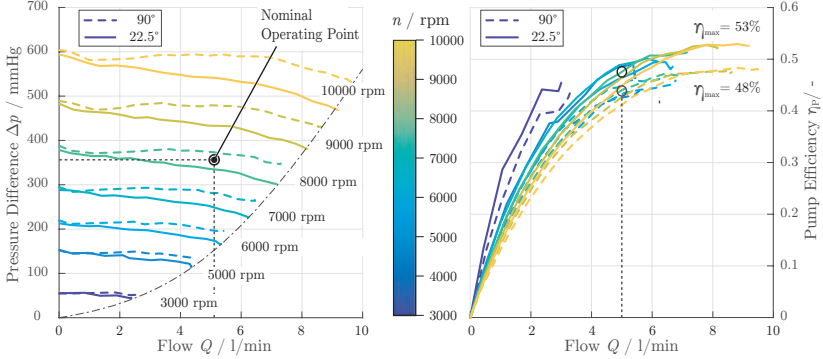


Figure 8.8: Comparison of the pressure-flow characteristic curve and the pump efficiency of two impellers with outlet angles 90° and 22.5° .

forces can be thus reduced, especially in the radial gap, which represents a high source of haemolysis for the base design B. During the in vitro experiments, the required rotational speed could be reduced from 7885 rpm to 5635 rpm. According to equation (8.4), this reduces maximum shear forces in the radial gap by 30% (while neglecting the Taylor vortices).

Accordingly, a significant reduction in cell damage would be expected. However, as additional narrow gaps are introduced around the extended blade and more considerable turbulence occurs on the trailing edges, this advantage is nullified.

Fig. 8.9 shows the haemolysis in the volute area, which is caused by the unshrouded blade section. Per rotation of the rotor, five blades pass this volute area. Since the circumferential speed of the flow considerably decreases after leaving the shrouded part of the blade, high relative velocities are created between the blade extension and the fluid in the volute. The shear forces at the blade edges are correspondingly high ($\tau \approx 700$ Pa).

The in vitro experiments also showed that the axial position of the rotor is not sufficiently stabilized. This can cause the blade edge to touch the volute wall, especially at high volumetric flows, which would lead to additional haemolysis. It could even cause scratches and abrasion, which would contaminate the blood and enhance haemolysis.

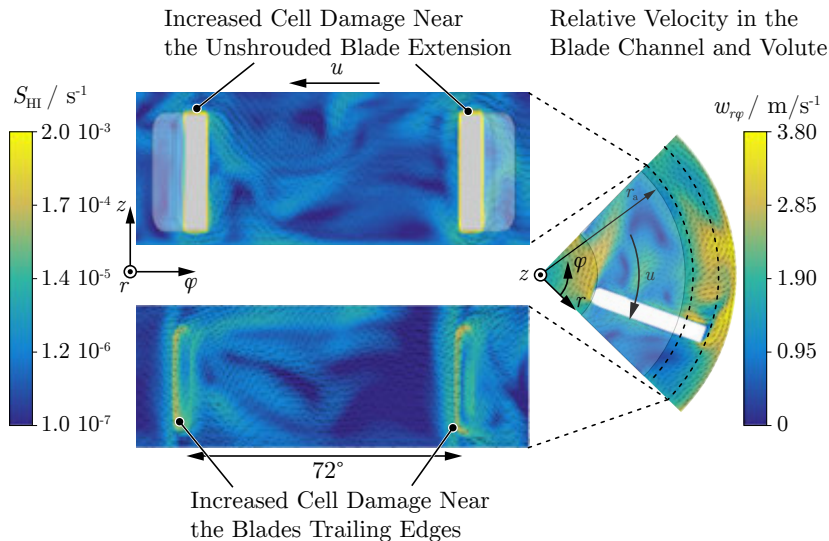


Figure 8.9: Distribution of haemolysis source term in the volute around the protruding blade portion.

8.3.6 Increase of the Inlet Nozzle Fillet

The highest shear forces occur on the transition from the suction nozzle to the suction mouth. A sharp change of direction of the housing wall and a hard unification of the leakage flow $Q_{\text{leak},S}$ with the incoming flow are causing this.

To prevent this, it is advisable to increase the inlet fillet of the suction nozzle. The fillet radius was increased from 1 mm to 6 mm for the R+ housing variation. As a result, the flow is less abruptly redirected, and a part of the front shroud gap is enlarged. In the area of the volute, the shroud gap δ_S remains unchanged, whereby the leakage flow $Q_{\text{leak},S}$ is only slightly increased.

Fig. 8.10 illustrates the damage rate on the housing surface and in the volume around the blade channel.

For the more rounded inlet nozzle, haemolysis in in vitro experiments is reduced by about 40%. The simulation also indicates a reduction in cell damage.

The better cell compatibility is mainly due to the greatly reduced

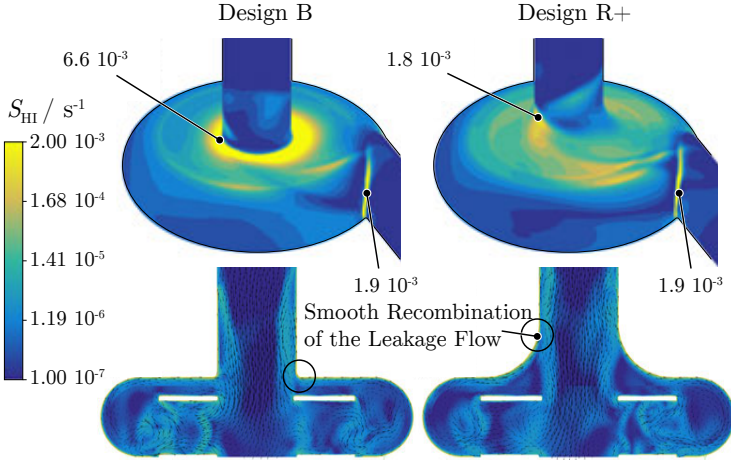


Figure 8.10: Distribution of haemolysis sources on the housing wall and in the volume around the blade head. Logarithmic scaling, cropped at $2 \cdot 10^{-3} \text{ s}^{-1}$.

shear forces on the inlet nozzle fillet. It should be noted that the scale in the figure is truncated at $S_{\text{HI}} = 2 \cdot 10^{-3} \text{ s}^{-1}$ to better illustrate the distribution. The local maximum of the cell damage in the base design B is $S_{\text{HI,B,max}} = 6.6 \cdot 10^{-3} \text{ s}^{-1}$. Due to the larger fillet radius, this value can be reduced to approximately $S_{\text{HI,R+,max}} = 1.8 \cdot 10^{-3} \text{ s}^{-1}$ in the design R+. Thus, the damage rate caused on the inlet fillet is similar to that on the volute tongue.

The results obtained from the in vitro experiments indicate 40% less haemolysis than the base design.

8.4 Summary

The different cell compatibility of individual pump variations was presented using the in vitro results and explained using CFD simulations. Significant differences compared to the base design were achieved by reducing the blade height, increasing the radial gap, extending the blades, increasing the inlet nozzle fillet, and by changing the outlet angle to 60° .

The reduction of the blade height leads to a widening of the axial

distance between the shroud plate and the housing lid thus increasing the leakage through this gap and decreasing the volumetric efficiency. As a result, a higher rotational speed is required to reach the nominal operating point. This leads to an increased cell damage in the radial gap.

Much of the same applies to the reduced blade angle. Due to the decreased meridional velocity, higher rotational speeds are required. This, in turn, causes more haemolysis in the radial gap.

Despite its small volume, the radial gap is responsible for more than 20% of the total cell damage. The damage density is highest in this area. By narrowing the radial gap, Taylor vortices could be avoided. However, the shear forces would increase sharply, which would result in increased haemolysis. The widening of the radial gap results in an enlargement of the Taylor vortices. Due to the lower relative speed, the damage rate decreases. At the same time, the leakage along the hub is increased. This reduces the residence time of the cells along the entire leakage path. Enlarging the radial gap by 75% reduces haemolysis by 25%.

By extending the impeller blades beyond the shroud disk, it is possible to reach the nominal operating point at a reduced rotational speed. This lowers the relative speed on all sidewall surfaces. Due to the additional narrow gaps between the blade extensions and the volute, the haemolysis in the volute increases significantly. High shear forces occur, especially in the vicinity of blade edges, which leads to additional cell damage. The haemolysis values achieved in the *in vitro* experiments clearly exceed those of the base design.

A further reduction of cell damage can be achieved by widening the inlet area. If the fillet radius between the inlet nozzle and the housing lid is increased from 1 mm to 6 mm, haemolysis can be reduced by 40%.

9

Benchmark Tests

Several in vitro experiments were conducted to evaluate the prototypes in comparison with commercially available products. In the following, the products used are presented, and the test conditions explained. The haemolysis results of the base design are then compared with these products to assess the quality of the prototypes.

9.1 Comparison Pumps

The range of products tested involves the BPX-80 (Medtronic), the FloPump 32¹ (International Biophysics Corporation), and the CentriMag (Abbott). Both, the BPX-80 and the FloPump are mechanically supported by a pivot bearing. The driving torque is transmitted with a magnetic coupling through the housing bottom. The CentriMag relies on the technology of the bearingless slice motor (Chapter 2).



Figure 9.1: Benchmark pumps and the prototype.

All these pumps are approved for extracorporeal applications and, in the case of the CentriMag, correspond to the current state of the art

¹equivalent to RotaFlow (Maquet)

of blood pumps.

Table 9.1 summarises the dimensions and operating points of the different products.

Table 9.1: Overview of commercial pumps used for comparison with the base design B.

Pump	d_a (mm)	V (ml)	Q_{\max} (l/min)	n_{nom} (rpm)
BPX-80*	79	80	10	3110
CentriMag**	32 (44)	31	9.9	4220
FloPump 32*	50	32	10	3835
Prototype B	22	15.5	9	7885

* FDA Approval, **Recalled by Abbott on August 22, 2019

Although the BPX-80 causes relatively high blood damage, it is often used as a reference pump in the literature. Since many results from haemolysis tests are available, it will also be tested in the following.

9.2 Test Conditions

All pumps were tested at a flow rate of 5l/min and at a pressure difference of 350 mmHg. Bovine blood was used and tempered to 30 °C. Except for the CentriMag, new and sterile packaged pump heads were used for all competitor products. The pumps were tested on the corresponding consoles.

The CentriMag was cleaned and disinfected after each use. This procedure was also used for the prototype. The Levitronix BPS-1.4 motor was used to drive the CentriMag.

The experiments were carried out according to Section 5.3.

9.3 Haemolysis Comparison

The results of several in vitro haemolysis tests are listed in Tab. 9.2. The base design B causes five times less haemolysis than the BPX-80, about 2.5 times less than the FloPump 32 and about 30% less than the CentriMag.

Table 9.2: In vitro benchmark tests of the base design B with regard to commercial products. The p -value refers to a two-sided t -test relative to the base design, assuming unequal variance.

Pump	NIH (mg/dl)	Std (mg/dl)	p	N	Volume (ml)
BPX-80	0.0502	0.0422	0.001	14	80
FloPump 32	0.0261	0.0141	0.058	5	32
CentriMag	0.0132	0.0051	0.040	24	31
B	0.0096	0.0043	-	16	15.5

As shown in Chapter 8, the cell compatibility of the base design B can be further reduced by up to 30–40% by enlarging the radial gap or rounding off the inlet nozzle. Accordingly, these designs cause about half the haemolysis as the best of the tested competitor products does.

10

Summary and Outlook

10.1 Summary

A majority of the blood pumps required in the medical field is used in extracorporeal applications. The pumps take over the heart function and maintain blood circulation during operations, or function as a bridge-to-transplant. However, the excessive mechanical stresses acting on cell membranes, when blood is pumped, lead to cell damage. This can cause renal and multi-organ failure with severe consequences.

In the present work, the cell damage mechanisms in a bearingless centrifugal pump were investigated in detail. For this purpose, two common topologies of bearingless slice motors were analysed, and their working principle derived. The slotless motor topology causes hardly any stator harmonics and is, therefore, suitable for applications requiring high rotational speed. The slotted temple motor is suitable for applications requiring high torque due to its sizeable winding space.

The Cordier diagram was used to investigate the efficiency of both topologies for pumping applications. It has been shown that the slotless topology only offers an advantage in terms of efficiency for applications demanding low pressure differences. The slotted temple motor is better suited for extracorporeal applications, which require a pressure difference of more than 100 mmHg.

After selecting a radial centrifugal pump, its function, loss mechanisms, and the hydraulic forces generated were explained. Based on a literature review, the hydraulic properties of blood and cell damage were described in detail. The most important factors influencing extracorporeal circulatory support concerning blood damage are the shear

forces, surface quality, and static pressure. In addition, possibilities for estimation of cell damage by means of simulations were presented.

Based on the findings, several prototypes were produced to investigate the damage mechanisms in bearingless centrifugal pumps. Additionally, test benches were set up to determine the influence of the surface quality, static pressure, and shear forces on cell damage.

Different methods for modeling cell damage were implemented in CFD simulations and compared with results from in vitro experiments. It was shown that results with deviations of just a few percent can be achieved with a suitable selection of the model parameters. It is also possible to estimate trends with regard to changes in geometry parameters. However, the sensitivity of the simulations to such changes is significantly lower than that of the in vitro experiments. Furthermore, essential factors such as the surface quality and the dynamics of the rotor cannot be taken into account due to the low data available and the limited computing power. In vitro examinations are therefore indispensable.

With the help of in vitro experiments, the importance of a high surface quality was emphasized. It turns out that the threshold value of $R_a \approx 0.4 \mu\text{m}$, given in the literature, is sufficient only under atmospheric conditions. At a static pressure of approx. 1 bar, surface roughness of $R_a < 0.2 \mu\text{m}$ already leads to significantly increased cell damage. The surface of the casing is decisive for the pumps considered, as it is more than twice as large as the impeller surface. The surface quality must be consistently high. Even small local defects lead to a significant increase in haemolysis.

Based on the CFD simulations, including the results obtained by in vitro experiments, the following chapters analysed the flow conditions in the pump and identified critical regions concerning the cell damage. The essential factors here are the shear forces in the radial gap, between the front shroud disk and the housing lid, as well as the fillet radius of the inlet nozzle. By taking appropriate measures at these locations, cell damage can be almost reduced by half.

Finally, the prototypes were compared in in vitro experiments with FDA-approved commercial pumps. It is shown that the haemolysis of the best prototype is 50% lower than that of the market-leading products.

10.2 Outlook

With the knowledge gained in this work and the help of the implemented simulation models, the existing designs can be further improved. The combination of the best prototypes is already expected to lead to an improvement in cell compatibility. Since the radial gap and the fillet radius of the inlet nozzle are barely coupled, haemolysis can be further halved by combining these two variations.

The axial flow, which occurs in the centre of the impeller, partly blocks the leakage flow through the washout hole. As shown, this causes large velocity gradients and, therefore, high shear forces. Alternative designs, e.g., with a baffle plate above the washout hole, should be investigated. With knowledge of the leakage volume, a baffle plate can be designed in such a way that the shear forces at the impeller inlet hardly change, and the leakage flow along the hub increases. The extent to which a surface, additionally introduced in this way, contributes to cell destruction must be investigated experimentally.

Further investigations should also be carried out on topologically different pump types. Only radial pumps were examined in this work. The extent to which this design is better or worse than, for example, diagonal pumps or double flow impellers must be investigated.

The dominant influence of surface was highlighted and substantiated in this work. Due to the high pressure difference, a further improvement of the haemolysis rate can be expected through better surface treatment. Further improvement in surface quality is possible, particularly in case of a serial production using injection moulding.

In order to improve the agreement of CFD simulations with in vitro experiments, the surface roughness should be considered in the simulations. This can be done using an additional source term for the transport equations. However, further in vitro investigations are necessary to determine the source term.

Appendices

A

Forces in Magnetic Fields

A.1 The Macroscopic Maxwell's Equations

The macroscopic Maxwell's equations represent a space average of the microscopic equations and distinguish the free current density \vec{j}_{free} from the magnetization \vec{M} bound to matter.

The magnetic induction thus is given by

$$\vec{B} = \mu_0(\vec{H} + \vec{M}). \quad (\text{A.1})$$

For a linear material, the following applies

$$\vec{B} = \mu\vec{H}. \quad (\text{A.2})$$

The Maxwell's equations then read as

$$\nabla \cdot \vec{D} = \rho_{\text{free}} \quad (\text{A.3})$$

$$\nabla \times \vec{H} = \vec{j}_{\text{free}} + \frac{\partial \vec{D}}{\partial t} \quad (\text{A.4})$$

$$\nabla \times \vec{E} = -\frac{\partial \vec{B}}{\partial t} \quad (\text{A.5})$$

$$\nabla \cdot \vec{B} = 0. \quad (\text{A.6})$$

The current density is $\vec{j}_{\text{free}} = \sigma\vec{E}$.

In the magnetostatic case, the Lorentz formulation (by eliminating \vec{D} and \vec{H}) results in

$$\nabla \times \vec{B} = \mu_0\vec{j}_{\text{free}} + \mu_0\nabla \times \vec{M}. \quad (\text{A.7})$$

In this formulation, magnetic dipoles are modeled as gyroscopic currents. They are bound to matter and do not contribute to the free current density.

A.2 Boundary Conditions

On the boundary surface between two materials with normal vector \vec{n} , boundary conditions apply

$$\vec{n} \cdot (\vec{B}_2 - \vec{B}_1) = 0, \quad (\text{A.8})$$

$$\vec{n} \times (\vec{H}_2 - \vec{H}_1) = \vec{j}_A, \quad (\text{A.9})$$

where \vec{j}_A represents the current density on the interface.

The normal component of the flux density B_n is thus continuous across the boundary surface. The same applies to the tangential component of the magnetic field strength H_t if no surface currents flow on the interface.

$$B_{n,1} = B_{n,2} \quad (\text{A.10})$$

$$H_{t,1} = H_{t,2} \quad (\text{A.11})$$

Fig. A.1 illustrates the field lines on an interface between two media with relative permeabilities $\mu_{r,1}$ and $\mu_{r,2}$.

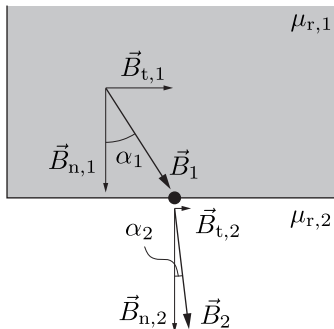


Figure A.1: Deflection of the field lines for transition into a matter of different permeability.

A.3 Forces in the Magnetic Field

The Minkowski tension tensor and Minkowski force density [121] are used to describe the force effect in bearingless motors. Although this description is not able to take into account effects such as magnetostriction, it is sufficient to capture the dominant forces. These are mainly Lorentz and reluctance forces for the motors considered.

A comprehensive explanation of the various stress tensors and force densities can be found in [122].

A.3.1 The Minkowski Stress Tensor

The Minkowski stress tensor is given by

$$\underline{\sigma} = \frac{1}{2} \left(\vec{D}^T \cdot \vec{E} + \vec{B}^T \cdot \vec{H} \right) \mathbb{I} - \vec{D} \otimes \vec{E} - \vec{B} \otimes \vec{H}. \quad (\text{A.12})$$

For the magnetostatic case in an isotropic material, equation (A.12) can be simplified to

$$\underline{\sigma} = \mu \vec{H} \otimes \vec{H} - \frac{1}{2} \mu (\vec{H}^T \cdot \vec{H}) \mathbb{I} \quad (\text{A.13})$$

$$= \mu \begin{pmatrix} H_x^2 - \frac{H^2}{2} & H_x H_y & H_x H_z \\ H_y H_x & H_y^2 - \frac{H^2}{2} & H_y H_z \\ H_z H_x & H_z H_y & H_z^2 - \frac{H^2}{2} \end{pmatrix}, \quad (\text{A.14})$$

where $H^2 = \sum_i H_i^2$ was used. Alternatively, in component notation

$$\sigma_{ij} = \mu H_i H_j - \frac{1}{2} \mu H_k H_k \delta_{ij}. \quad (\text{A.15})$$

Here, the Einstein summation convention applies.

A.3.2 Surface Forces on Boundary Surfaces

The force surface density acting on a surface A with normal vector \vec{n} results from

$$\vec{f}_A = \underline{\sigma} \cdot \vec{n} = \mu \left(\vec{H} \cdot \vec{H}^T \right) \vec{n} - \frac{1}{2} \mu (\vec{H}^T \cdot \vec{H}) \vec{n} = \frac{1}{2} \left(2\mu \vec{H} H_n - \mu H^2 \vec{n} \right). \quad (\text{A.16})$$

If the surface force is divided into a normal and a tangential component, the following is obtained

$$\vec{f}_A = \frac{\mu}{2} \begin{pmatrix} H_n^2 - H_t^2 \\ 2H_n H_t \end{pmatrix} = \frac{1}{2} \begin{pmatrix} \frac{B_n^2}{\mu} - \mu H_t^2 \\ 2B_n H_t \end{pmatrix}. \quad (\text{A.17})$$

When considering a boundary crossing on a surface from permeability μ_1 with normal vector \vec{n}_1 to a permeability μ_2 with normal vector $\vec{n}_2 = -\vec{n}_1$, the two surface forces are given by

$$\vec{f}_{A1} = \underline{\sigma}_1 \cdot \vec{n}_1 = \frac{1}{2} \begin{pmatrix} \frac{B_n^2}{\mu_1} - \mu_1 H_t^2 \\ 2B_n H_t \end{pmatrix}, \quad (\text{A.18})$$

$$\vec{f}_{A2} = -\underline{\sigma}_2 \cdot \vec{n}_1 = -\frac{1}{2} \begin{pmatrix} \frac{B_n^2}{\mu_2} - \mu_2 H_t^2 \\ 2B_n H_t \end{pmatrix}. \quad (\text{A.19})$$

The boundary conditions $B_{n,1} = B_{n,2} = B_n$ and $H_{t,1} = H_{t,2} = H_t$ were used.

The resulting force on the boundary surface is finally determined with vector addition of the forces acting on both sides:

$$\vec{f}_{AG} = \vec{f}_{A1} + \vec{f}_{A2} = \begin{pmatrix} \left(\frac{1}{\mu_1} - \frac{1}{\mu_2}\right) B_n^2 + (\mu_2 - \mu_1) H_t^2 \\ 0 \end{pmatrix}. \quad (\text{A.20})$$

Thus, the reluctance force always acts perpendicular to the boundary surfaces.

At the transition from one medium to another with strongly different permeability ($\mu_2 \gg \mu_1$), the reluctance force is simplified to

$$\vec{f}_{AG} = \frac{1}{2\mu_1} B_n^2 \vec{n}_1 = \frac{1}{2\mu_1} B^2 \vec{n}_1. \quad (\text{A.21})$$

A.3.3 Volume Forces

External forces act on the surface ∂V of any considered volume element V , observed as a cut-out from its surroundings. The resulting force \vec{F}_V on the volume element V can, therefore, be calculated as

$$\vec{F}_V = \int_{\partial V} \underline{\sigma} \cdot d\vec{A}. \quad (\text{A.22})$$

By applying Gauss's theorem extended to tensors, the following applies

$$\vec{F}_V = \int_{\partial A} \underline{\sigma} \cdot d\vec{A} = \int_V \nabla \cdot \underline{\sigma} dV = \int_V \vec{f}_V dV, \quad (\text{A.23})$$

where

$$(\nabla \cdot \underline{\sigma})_j = \sum_i \left(\nabla_i (\mu H_i H_j) - \nabla_i \left(\frac{1}{2} \mu H^2 \delta_{ij} \right) \right). \quad (\text{A.24})$$

When considering a volume element located in a homogeneous material, $\mu \neq \mu(\vec{x})$ applies. The following results:

$$(\nabla \cdot \underline{\sigma})_j = \sum_i \left((\nabla_i \cdot B_i) H_j + (B_i \cdot \nabla_i) H_j - \frac{1}{2} \mu (\nabla_i H^2) \delta_{ij} \right) \quad (\text{A.25})$$

$$= \sum_i \frac{1}{\mu} \left((\nabla_i \cdot B_i) B_j + (B_i \cdot \nabla_i) B_j - \frac{1}{2} \nabla_i B^2 \delta_{ij} \right) \quad (\text{A.26})$$

$$\nabla \cdot \underline{\sigma} = \frac{1}{\mu} \left((\nabla \cdot \vec{B}) \vec{B} + (\vec{B} \cdot \nabla) \vec{B} - \frac{1}{2} \nabla B^2 \right). \quad (\text{A.27})$$

With aid of the vector identity

$$\frac{1}{2} \nabla B^2 = \vec{B} \times (\nabla \times \vec{B}) + (\vec{B} \cdot \nabla) \vec{B}, \quad (\text{A.28})$$

it follows:

$$\vec{f}_V = \nabla \cdot \underline{\sigma} = \frac{1}{\mu} \left((\nabla \cdot \vec{B}) \vec{B} - \vec{B} \times (\nabla \times \vec{B}) \right) \quad (\text{A.29})$$

$$= \frac{1}{\mu} (\nabla \times \vec{B}) \times \vec{B} \quad (\text{A.30})$$

$$= (\nabla \times \vec{H}) \times \vec{B} = \vec{j}_{\text{free}} \times \vec{B}. \quad (\text{A.31})$$

This corresponds to the Lorentz force on the unbound charge carriers.

If previous considerations are generalised and a linear isentropic medium with $\mu = \mu(\vec{x})$ is assumed, an additional term appears. The resulting volume force density can be written as [123]

$$\vec{f}_V = \vec{j}_{\text{free}} \times \vec{B} - \frac{1}{2} H^2 \nabla \mu. \quad (\text{A.32})$$

This is called the Minkowski force density.

It becomes clear that the volume force can be divided into Lorentz and reluctance forces.

Bibliography

- [1] W. E. Gerabek, B. D. Haage, G. Keil, and W. Wegner, *Enzyklo-pädie Medizingeschichte*. Walter de Gruyter, 2011.
- [2] E. Wilkins, L. Wilson, K. Wickramasinghe, P. Bhatnagar, J. Leal, R. Luengo-Fernandez, R. Burns, M. Rayner, and N. Townsend, “European cardiovascular disease statistics 2017,” *European Heart Network, Brussels, Belgium.*, 2017.
- [3] E. J. Benjamin, M. J. Blaha, S. E. Chiuve, M. Cushman, S. R. Das, R. Deo, J. Floyd, M. Fornage, C. Gillespie, C. Isasi *et al.*, “Heart disease and stroke statistics - 2017 update: A report from the american heart association.” *Circulation*, vol. 135, no. 10, pp. e146–e603, Jan. 2017. DOI: [10.1161/CIR.000000000000485](https://doi.org/10.1161/CIR.000000000000485)
- [4] R. L. Kormos, J. Cowger, F. D. Pagani, J. J. Teuteberg, D. J. Goldstein, J. P. Jacobs, R. S. Higgins, L. W. Stevenson, J. Stehlik, P. Atluri *et al.*, “The society of thoracic surgeons intermacs database annual report: Evolving indications, outcomes, and scientific partnerships,” *The Journal of Heart and Lung Transplantation*, vol. 38, no. 2, pp. 114–126, Feb. 2019. DOI: [10.1016/j.jhealum.2018.11.013](https://doi.org/10.1016/j.jhealum.2018.11.013)
- [5] T. Krabatsch, I. Netuka, J. D. Schmitto, D. Zimpfer, J. Garbade, V. Rao, M. Morshuis, F. Beyersdorf, S. Marasco, L. Damme *et al.*, “HeartMate III fully magnetically levitated left ventricular assist device for the treatment of advanced heart failure -1 year results from the CE mark trial,” *Journal of Cardiothoracic Surgery*, vol. 12, no. 1, p. 23, Nov. 2017. DOI: [10.1186/s13019-017-0587-3](https://doi.org/10.1186/s13019-017-0587-3)
- [6] T. V. Brogan, L. Lequier, R. Lorusso, G. MacLaren, and G. J. Peek, *Extracorporeal Life Support: The ELSO Red Book*. Extracorporeal Life Support Organization, 2017.
- [7] Extracorporeal Life Support Organization, “ECLS registry report,” Jan. 2019.
- [8] F. Sangalli, N. Patroniti, A. Pesenti *et al.*, *ECMO - Extracorporeal Life Support in Adults*. Springer, 2014. DOI: [10.1007/978-88-470-5427-1](https://doi.org/10.1007/978-88-470-5427-1)

- [9] D. A. Murphy, L. E. Hockings, R. K. Andrews, C. Aubron, E. E. Gardiner, V. A. Pellegrino, and A. K. Davis, "Extracorporeal membrane oxygenation - Hemostatic complications," *Transfusion Medicine Reviews*, vol. 29, no. 2, pp. 90 – 101, Apr. 2015, Special Issue (Australian Issue). DOI: <https://doi.org/10.1016/j.tmr.2014.12.001>
- [10] C. S. Barrett, J. J. Jagers, E. F. Cook, D. A. Graham, S. K. Rajagopal, C. S. Almond, J. D. Seeger, P. T. Rycus, and R. R. Thiagarajan, "Outcomes of neonates undergoing extracorporeal membrane oxygenation support using centrifugal versus roller blood pumps," *The Annals of Thoracic Surgery*, vol. 94, no. 5, pp. 1635–1641, Nov. 2012. DOI: [10.1016/j.athoracsur.2012.06.061](https://doi.org/10.1016/j.athoracsur.2012.06.061)
- [11] C. S. Barrett, J. J. Jagers, E. F. Cook, D. A. Graham, V. V. Yarlagadda, S. A. Teele, C. S. Almond, S. L. Bratton, J. D. Seeger, H. J. Dalton *et al.*, "Pediatric ECMO outcomes: Comparison of centrifugal versus roller blood pumps using propensity score matching," *ASAIO Journal*, vol. 59, no. 2, pp. 145–151, Apr. 2013. DOI: [10.1097/MAT.0b013e31828387cd](https://doi.org/10.1097/MAT.0b013e31828387cd)
- [12] J. V. McDonald, T. P. Green, and R. H. Steinhorn, "The role of the centrifugal pump in hemolysis during neonatal extracorporeal support," *ASAIO Journal*, vol. 43, no. 1, pp. 35–38, Feb. 1997.
- [13] J. P. Mueller, A. Kuenzli, O. Reuthebuch, K. Dasse, S. Kent, G. Zuend, M. I. Turina, and M. L. Lachat, "The CentriMag: A new optimized centrifugal blood pump with levitating impeller," in *The Heart Surgery Forum*, vol. 7, no. 5, Jan. 2004, pp. E477–80. DOI: [10.1532/HSF98.20041068](https://doi.org/10.1532/HSF98.20041068)
- [14] F. De Robertis, E. Birks, P. Rogers, G. Dreyfus, J. Pepper, and A. Khaghani, "Clinical performance with the Levitronix CentriMag short-term ventricular assist device," *The Journal of Heart and Lung Transplantation*, vol. 25, no. 2, pp. 181–186, Feb. 2006. DOI: [10.1016/j.healun.2005.08.019](https://doi.org/10.1016/j.healun.2005.08.019)
- [15] J. H. Shuhaiber, D. Jenkins, M. Berman, J. Parameshwar, K. Dhital, S. Tsui, and S. R. Large, "The Papworth experience with the Levitronix CentriMag ventricular assist device," *The Journal of Heart and Lung Transplantation*, vol. 27, no. 2, pp. 158–164, Feb. 2008. DOI: [10.1016/j.healun.2007.10.015](https://doi.org/10.1016/j.healun.2007.10.015)

-
- [16] R. John, J. W. Long, H. T. Massey, B. P. Griffith, B. C. Sun, A. J. Tector, O. H. Frazier, and L. D. Joyce, "Outcomes of a multicenter trial of the Levitronix CentriMag ventricular assist system for short-term circulatory support," *The Journal of Thoracic and Cardiovascular Surgery*, vol. 141, no. 4, pp. 932–939, Apr. 2011. DOI: [10.1016/j.jtcvs.2010.03.046](https://doi.org/10.1016/j.jtcvs.2010.03.046)
- [17] T. A. Aziz, G. Singh, E. Popjes, E. Stephenson, S. Mulvey, W. Pae, and A. El-Banayosy, "Initial experience with CentriMag extracorporeal membrane oxygenation for support of critically ill patients with refractory cardiogenic shock," *The Journal of Heart and Lung Transplantation*, vol. 29, no. 1, pp. 66–71, Jan. 2010. DOI: [10.1016/j.healun.2009.08.025](https://doi.org/10.1016/j.healun.2009.08.025)
- [18] A. Loforte, A. Montalto, F. Ranocchi, P. L. Della Monica, G. Casali, A. Lappa, C. Contento, and F. Musumeci, "Levitronix CentriMag third-generation magnetically levitated continuous flow pump as bridge to solution," *ASAIO Journal*, vol. 57, no. 4, pp. 247–253, Aug. 2011. DOI: [10.1097/MAT.0b013e31821f2116](https://doi.org/10.1097/MAT.0b013e31821f2116)
- [19] M. A. Sobieski, G. A. Giridharan, M. Ising, S. C. Koenig, and M. S. Slaughter, "Blood trauma testing of CentriMag and RotaFlow centrifugal flow devices: A pilot study," *Artificial Organs*, vol. 36, no. 8, pp. 677–682, Aug. 2012. DOI: [10.1111/j.1525-1594.2012.01514.x](https://doi.org/10.1111/j.1525-1594.2012.01514.x)
- [20] D. A. Palanzo, A. El-Banayosy, E. Stephenson, C. Brehm, A. Kunselman, and W. E. Pae, "Comparison of hemolysis between CentriMag and RotaFlow rotary blood pumps during extracorporeal membrane oxygenation," *Artificial Organs*, vol. 37, no. 9, pp. E162–E166, 2013. DOI: [10.1111/aor.12158](https://doi.org/10.1111/aor.12158)
- [21] R. Schoeb and N. Barletta, "Magnetic bearing. Principle and application of a bearingless slice motor." *JSME International Journal Series C Mechanical Systems, Machine Elements and Manufacturing*, vol. 40, no. 4, pp. 593–598, Dec. 1997. DOI: [10.1299/jsmec.40.593](https://doi.org/10.1299/jsmec.40.593)
- [22] T. Schneeberger, T. Nussbaumer, and J. W. Kolar, "Magnetically levitated homopolar hollow-shaft motor," *IEEE/ASME Transactions on Mechatronics*, vol. 15, no. 1, pp. 97–107, Feb. 2010. DOI: [10.1109/TMECH.2009.2018836](https://doi.org/10.1109/TMECH.2009.2018836)

- [23] P. Karutz, T. Nussbaumer, W. Gruber, and J. W. Kolar, “Novel magnetically levitated two-level motor,” *IEEE/ASME Transactions on Mechatronics*, vol. 13, no. 6, pp. 658–668, Dec. 2008. DOI: [10.1109/TMECH.2008.2004344](https://doi.org/10.1109/TMECH.2008.2004344)
- [24] H. Sugimoto, Y. Uemura, A. Chiba, and M. A. Rahman, “Design of homopolar consequent-pole bearingless motor with wide magnetic gap,” *IEEE Transactions on Magnetics*, vol. 49, no. 5, pp. 2315–2318, May 2013. DOI: [10.1109/TMAG.2013.2243420](https://doi.org/10.1109/TMAG.2013.2243420)
- [25] W. Gruber, M. Rothböck, and R. T. Schöb, “Design of a novel homopolar bearingless slice motor with reluctance rotor,” *IEEE Transactions on Industry Applications*, vol. 51, no. 2, pp. 1456–1464, Mar. 2015. DOI: [10.1109/TIA.2014.2341739](https://doi.org/10.1109/TIA.2014.2341739)
- [26] S. Jumayev, A. Borisavljevic, K. Boynov, J. Pyrhönen, and E. Lomonova, “Inductance calculation of high-speed slotless permanent magnet machines,” *The International Journal for Computation and Mathematics in Electrical and Electronic Engineering (COMPEL)*, vol. 34, no. 2, pp. 413–427, Mar. 2015. DOI: [10.1108/COMPEL-08-2014-0207](https://doi.org/10.1108/COMPEL-08-2014-0207)
- [27] A. Borisavljevic, S. Jumayev, and E. Lomonova, “Toroidally-wound permanent magnet machines in high-speed applications,” in *International Conference on Electrical Machines (ICEM)*, 2014, pp. 2588–2593. DOI: [10.1109/ICELMACH.2014.6960552](https://doi.org/10.1109/ICELMACH.2014.6960552)
- [28] H. Eckhardt, *Grundzüge der elektrischen Maschinen*. Springer, 1982. DOI: [10.1007/978-3-322-94292-0](https://doi.org/10.1007/978-3-322-94292-0)
- [29] R. Fischer, “Allgemeine Grundlagen elektrischer Maschinen,” in *Elektrische Maschinen*. Carl Hanser Verlag GmbH & Co, 2017, pp. 269–377. DOI: [10.3139/9783446452954.001](https://doi.org/10.3139/9783446452954.001)
- [30] D. K. Steinert, “Der nutzenlose lagerlose Scheibenläufermotor,” Ph.D. dissertation, ETH Zürich, 2015. DOI: [10.3929/ethz-a-010617770](https://doi.org/10.3929/ethz-a-010617770)
- [31] J. Yonnet, “Permanent magnet bearings and couplings,” *IEEE Transactions on Magnetics*, vol. 17, no. 1, pp. 1169–1173, Jan. 1981. DOI: [10.1109/TMAG.1981.1061166](https://doi.org/10.1109/TMAG.1981.1061166)

- [32] S. Earnshaw, “On the nature of the molecular forces which regulate the constitution of the luminiferous ether,” *Transactions of the Cambridge Philosophical Society*, vol. 7, pp. 97–112, Mar. 1842.
- [33] J. J. H. Paulides, K. J. Meessen, and E. A. Lomonova, “Eddy-current losses in laminated and solid steel stator back iron in a small rotary brushless permanent-magnet actuator,” *IEEE Transactions on Magnetics*, vol. 44, no. 11, pp. 4373–4376, Nov. 2008. DOI: [10.1109/TMAG.2008.2001996](https://doi.org/10.1109/TMAG.2008.2001996)
- [34] D. Steinert, I. Kovacevic-Badstübner, T. Nussbaumer, and J. W. Kolar, “Loss investigation of slotless bearingless disk drives,” in *IEEE Energy Conversion Congress and Exposition (ECCE)*, 2015, pp. 4418–4424. DOI: [10.1109/ECCE.2015.7310284](https://doi.org/10.1109/ECCE.2015.7310284)
- [35] J. R. Rumble, *CRC Handbook of Chemistry and Physics*. CRC Press/Taylor & Francis, 2019.
- [36] Surahammars Bruks AB, Surahammar, Sweden. Non-Grain Oriented Electrical Steel M330-35A. Dec. 2009.
- [37] P. Pfister and Y. Perriard, “Slotless permanent-magnet machines: General analytical magnetic field calculation,” *IEEE Transactions on Magnetics*, vol. 47, no. 6, pp. 1739–1752, Jun. 2011. DOI: [10.1109/TMAG.2011.2113396](https://doi.org/10.1109/TMAG.2011.2113396)
- [38] O. Cordier, “Ähnlichkeitsbedingungen für Strömungsmaschinen,” *BWK das Energie-Fachmagazin Verein Deutscher Ingenieure*, vol. 5, no. 10, pp. 337–340, Oct. 1953.
- [39] J. Seume and R. Mailach, “Grundlagen der Strömungsmaschinen,” in *Dubbel*. Springer, 2014, pp. R2–R29. DOI: [10.1007/978-3-642-38891-0_102](https://doi.org/10.1007/978-3-642-38891-0_102)
- [40] J. F. Gülich, *Kreiselpumpen: Handbuch für Entwicklung, Anlagenplanung und Betrieb*. Springer, 2010. DOI: [10.1007/978-3-642-05479-2](https://doi.org/10.1007/978-3-642-05479-2)
- [41] VDI-Gesellschaft Verfahrenstechnik und Chemieingenieurwesen (GVC), *VDI Heat Atlas*, 2nd edition. Springer, 2010.

- [42] J. Gülich and U. Bolleter, “Pressure pulsations in centrifugal pumps,” *Journal of Vibration and Acoustics*, vol. 114, no. 2, pp. 272–279, Apr. 1992. DOI: [10.1115/1.2930257](https://doi.org/10.1115/1.2930257)
- [43] I. J. Karassik, J. P. Messina, P. Cooper, C. C. Heald *et al.*, *Pump Handbook*. McGraw-Hill New York, 2001, vol. 3.
- [44] C. Pfeleiderer, *Strömungsmaschinen*. Springer, 1991. DOI: [10.1007/978-3-662-10101-8](https://doi.org/10.1007/978-3-662-10101-8)
- [45] A. J. Stepanoff, *Centrifugal and Axial Flow Pumps: Theory, Design, and Application*. Wiley New York, 1957.
- [46] A. Agostinelli, D. Nobles, and C. R. Mockridge, “An experimental investigation of radial thrust in centrifugal pumps,” *Journal of Engineering for Power*, vol. 82, no. 2, pp. 120–125, Apr. 1960. DOI: [10.1115/1.3672726](https://doi.org/10.1115/1.3672726)
- [47] A. M. Robertson, A. Sequeira, and M. V. Kameneva, “Hemorheology,” in *Hemodynamical Flows*. Springer, 2008, pp. 63–120. DOI: [10.1007/978-3-7643-7806-6_2](https://doi.org/10.1007/978-3-7643-7806-6_2)
- [48] R. A. McPherson and M. R. Pincus, *Henry’s clinical diagnosis and management by laboratory methods*. Elsevier Health Sciences, 2011.
- [49] R. F. Schmidt and G. Thews, *Physiologie des Menschen*. Springer, 2010. DOI: [10.1007/978-3-642-01651-6](https://doi.org/10.1007/978-3-642-01651-6)
- [50] D. Obrist, P. Jenny, and J. Sznitman, “Fluid dynamic phenomena in the human body,” in *Biofluidynamics*. ARTORG Center, University of Bern, 2016.
- [51] F. H. Martini, J. L. Nath, and E. F. Bartholomew, *Fundamentals of Anatomy & Physiology*, 9th edition. Prentice Hall: Pearson, 2012.
- [52] S. Chien, “Shear dependence of effective cell volume as a determinant of blood viscosity,” *Science*, vol. 168, no. 3934, pp. 977–979, May 1970. DOI: [10.1126/science.168.3934.977](https://doi.org/10.1126/science.168.3934.977)
- [53] D. Arora, “Computational hemodynamics: Hemolysis and viscoelasticity,” Ph.D. dissertation, Citeseer, 2005.

- [54] H. Schmid-Schönbein and R. Wells, “Fluid drop-like transition of erythrocytes under shear,” *Science*, vol. 165, no. 3890, pp. 288–291, Jul. 1969. DOI: [10.1126/science.165.3890.288](https://doi.org/10.1126/science.165.3890.288)
- [55] J. Zhang, A. Koert, B. Gellman, T. M. Gempp, K. A. Dasse, R. J. Gilbert, B. P. Griffith, and Z. J. Wu, “Optimization of a miniature maglev ventricular assist device for pediatric circulatory support,” *ASAIO Journal*, vol. 53, no. 1, pp. 23–31, Jan. 2007. DOI: [10.1097/01.mat.0000247043.18115.f7](https://doi.org/10.1097/01.mat.0000247043.18115.f7)
- [56] M. E. Taskin, K. H. Fraser, T. Zhang, B. Gellman, A. Fleischli, K. A. Dasse, B. P. Griffith, and Z. J. Wu, “Computational characterization of flow and hemolytic performance of the UltraMag blood pump for circulatory support,” *Artificial Organs*, vol. 34, no. 12, pp. 1099–1113, Dec. 2010. DOI: [10.1111/j.1525-1594.2010.01017.x](https://doi.org/10.1111/j.1525-1594.2010.01017.x)
- [57] INTERMACS. Intermacs adverse events definitions. <https://www.uab.edu/medicine/intermacs/intermacs-documents>. May 2013. Accessed 22. Nov 2019.
- [58] L. Wurzinger, R. Opitz, and H. Eckstein, “Mechanical blood trauma. An overview,” *Angeiologie*, vol. 38, no. 3, pp. 81–97, May 1986.
- [59] S. Hashimoto, “Erythrocyte destruction under periodically fluctuating shear rate: Comparative study with constant shear rate,” *Artificial Organs*, vol. 13, no. 5, pp. 458–463, Oct. 1989. DOI: [10.1111/j.1525-1594.1989.tb01558.x](https://doi.org/10.1111/j.1525-1594.1989.tb01558.x)
- [60] D. Steines, D. Westphal, C. Göbel, H. Reul, and G. Rau, “Platelet function and hemolysis in centrifugal pumps: In vitro investigations,” *The International Journal of Artificial Organs*, vol. 22, no. 8, pp. 559–565, Aug. 1999. DOI: [10.1177/039139889902200806](https://doi.org/10.1177/039139889902200806)
- [61] C. Kramer, P. Sand, and W. Bleifeld, “Blutströmung und mechanische Hämolyse,” *Biomedizinische Technik/Biomedical Engineering*, vol. 16, no. 5, pp. 164–168, Jan. 1971. DOI: [10.1515/bmte.1971.16.5.164](https://doi.org/10.1515/bmte.1971.16.5.164)

- [62] G. Heuser and R. Opitz, "A Couette viscometer for short time shearing of blood," *Biorheology*, vol. 17, no. 1-2, pp. 17–24, Oct. 1980. DOI: [10.3233/BIR-1980-171-205](https://doi.org/10.3233/BIR-1980-171-205)
- [63] R. Indeglia, M. Shea, R. Forstrom, and E. Bernstein, "Influence of mechanical factors on erythrocyte sublethal damage," *ASAIO Journal*, vol. 14, no. 1, pp. 264–272, Apr. 1968.
- [64] L. Leverett, J. Hellums, C. Alfrey, and E. Lynch, "Red blood cell damage by shear stress," *Biophysical Journal*, vol. 12, no. 3, pp. 257–273, Mar. 1972. DOI: [10.1016/s0006-3495\(72\)86085-5](https://doi.org/10.1016/s0006-3495(72)86085-5)
- [65] R. Paul, J. Apel, S. Klaus, F. Schügner, P. Schwindke, and H. Reul, "Shear stress related blood damage in laminar Couette flow," *Artificial Organs*, vol. 27, no. 6, pp. 517–529, Jun. 2003. DOI: [10.1046/j.1525-1594.2003.07103.x](https://doi.org/10.1046/j.1525-1594.2003.07103.x)
- [66] A. M. Sallam and N. H. Hwang, "Human red blood cell hemolysis in a turbulent shear flow: Contribution of Reynolds shear stresses," *Biorheology*, vol. 21, no. 6, pp. 783–797, Dec. 1984. DOI: [10.3233/BIR-1984-21605](https://doi.org/10.3233/BIR-1984-21605)
- [67] R. Eilers, "Einsatz und Bewertung rechnergestützter Methoden für die technische Auslegung mechanischer Herzklappenprothesen," Ph.D. dissertation, Technische Hochschule Aachen, 1997.
- [68] L. Goubergrits and K. Affeld, "Numerical estimation of blood damage in artificial organs," *Artificial Organs*, vol. 28, no. 5, pp. 499–507, May 2004. DOI: [10.1111/j.1525-1594.2004.07265.x](https://doi.org/10.1111/j.1525-1594.2004.07265.x)
- [69] L. Wurzinger, R. Opitz, P. Blasberg, and H. Schmid-Schönbein, "Platelet and coagulation parameters following millisecond exposure to laminar shear stress." *Thrombosis and Haemostasis*, vol. 54, no. 2, pp. 381–386, Mar. 1985. DOI: [10.1055/s-0038-1657744](https://doi.org/10.1055/s-0038-1657744)
- [70] M. Giersiepen, L. Wurzinger, R. Opitz, and H. Reul, "Estimation of shear stress-related blood damage in heart valve prostheses - In vitro comparison of 25 aortic valves." *The International Journal of Artificial Organs*, vol. 13, no. 5, pp. 300–306, May 1990. DOI: [10.1177/039139889001300507](https://doi.org/10.1177/039139889001300507)

- [71] S. S. Lee, J. F. Antaki, M. V. Kameneva, J. G. Dobbe, M. R. Hardeman, K. H. Ahn, and S. J. Lee, "Strain hardening of red blood cells by accumulated cyclic supraphysiological stress," *Artificial Organs*, vol. 31, no. 1, pp. 80–86, Jan. 2007.
- [72] P. L. Blackshear Jr, F. D. Dorman, and J. H. Steinbach, "Some mechanical effects that influence hemolysis," *ASAIO Journal*, vol. 11, no. 1, pp. 112–117, Apr. 1965.
- [73] S. D. Chambers, K. R. Laberteaux, S. I. Merz, J. P. Montoya, and R. H. Bartlett, "Effects of static pressure on red blood cells on removal of the air interface." *ASAIO Journal*, vol. 42, no. 6, pp. 947–950, Dec. 1996. DOI: [10.1097/00002480-199642060-00005](https://doi.org/10.1097/00002480-199642060-00005)
- [74] J. Wielogorski, D. Cross, and E. Nwadike, "The effects of sub-atmospheric pressure on the haemolysis of blood," *Journal of Biomechanics*, vol. 8, no. 5, pp. 321–325, Sep. 1975. DOI: [10.1016/0021-9290\(75\)90084-6](https://doi.org/10.1016/0021-9290(75)90084-6)
- [75] J. R. Pohlmann, J. M. Toomasian, C. E. Hampton, K. E. Cook, G. M. Annich, and R. H. Bartlett, "The relationships between air exposure, negative pressure and hemolysis," *ASAIO Journal*, vol. 55, no. 5, p. 469, Oct. 2009. DOI: [10.1097/MAT.0b013e3181b28a5a](https://doi.org/10.1097/MAT.0b013e3181b28a5a)
- [76] N. Handa, T. Yasuda, A. Funakubo, and Y. Fukui, "The relation between physical factors and hemolysis," *Japanese Journal of Artificial Organs*, vol. 27, no. 1, pp. 118–123, Oct. 1998.
- [77] T. Yasuda, A. Funakubo, F. Miyawaki, T. Kawamura, T. Higami, and Y. Fukui, "Influence of static pressure and shear rate on hemolysis of red blood cells," *ASAIO Journal*, vol. 47, no. 4, pp. 351–353, Aug. 2001. DOI: [10.1097/00002480-200107000-00011](https://doi.org/10.1097/00002480-200107000-00011)
- [78] Y. Wakisaka, Y. Taenaka, T. Nakatani, H. Anai, K. Araki, T. Nishimura, E. Tatsumi, T. Masuzawa, Y. Baba, K. Toda *et al.*, "Tandem operation of a turbo blood pump (BP-80-type centrifugal pump) to reduce hemolysis," *Artificial Organs*, vol. 20, no. 5, pp. 572–574, May 1996. DOI: [10.1111/j.1525-1594.1996.tb04483.x](https://doi.org/10.1111/j.1525-1594.1996.tb04483.x)
- [79] Y. Tamari, K. Lee-Sensiba, E. F. Leonard, V. Parnell, and A. J. Tortolani, "The effects of pressure and flow on hemolysis caused

- by Bio-Medicus centrifugal pumps and roller pumps,” *Journal of Thoracic and Cardiovascular Surgery*, vol. 106, no. 6, pp. 997–1007, Dec. 1993. DOI: [10.1016/S0022-5223\(19\)33970-4](https://doi.org/10.1016/S0022-5223(19)33970-4)
- [80] A. Arvand, M. Hormes, and H. Reul, “A validated computational fluid dynamics model to estimate hemolysis in a rotary blood pump,” *Artificial Organs*, vol. 29, no. 7, pp. 531–540, Jul. 2005. DOI: [10.1111/j.1525-1594.2005.29089.x](https://doi.org/10.1111/j.1525-1594.2005.29089.x)
- [81] T. Yasuda, K. Shimokasa, A. Funakubo, T. Higami, T. Kawamura, and Y. Fukui, “An investigation of blood flow behavior and hemolysis in artificial organs,” *ASAIO Journal*, vol. 46, no. 5, pp. 527–531, Oct. 2000. DOI: [10.1097/00002480-200009000-00003](https://doi.org/10.1097/00002480-200009000-00003)
- [82] J. M. Monroe, D. E. True, and M. C. Williams, “Surface roughness and edge geometries in hemolysis with rotating disk flow,” *Journal of Biomedical Materials Research*, vol. 15, no. 6, pp. 923–939, Nov. 1981. DOI: [10.1002/jbm.820150616](https://doi.org/10.1002/jbm.820150616)
- [83] O. Maruyama, Y. Numata, M. Nishida, T. Yamane, I. Oshima, Y. Adachi, and T. Masuzawa, “Hemolysis caused by surface roughness under shear flow,” *Journal of Artificial Organs*, vol. 8, no. 4, pp. 228–236, Dec. 2005. DOI: [10.1007/s10047-005-0316-x](https://doi.org/10.1007/s10047-005-0316-x)
- [84] O. Maruyama, M. Nishida, T. Yamane, I. Oshima, Y. Adachi, and T. Masuzawa, “Hemolysis resulting from surface roughness under shear flow conditions using a rotational shear stressor,” *Artificial Organs*, vol. 30, no. 5, pp. 365–370, May 2006. DOI: [10.1111/j.1525-1594.2006.00227.x](https://doi.org/10.1111/j.1525-1594.2006.00227.x)
- [85] Y. Takami, K. Makinouchi, T. Nakazawa, J. Glueck, R. Benkowski, and Y. Nose, “Effect of surface roughness on hemolysis in a pivot bearing supported Gyro centrifugal pump (C1E3),” *Artificial Organs*, vol. 20, no. 11, pp. 1155–1161, Nov. 1996. DOI: [10.1111/j.1525-1594.1996.tb00655.x](https://doi.org/10.1111/j.1525-1594.1996.tb00655.x)
- [86] Y. Takami, T. Nakazawa, K. Makinouchi, E. Tayama, J. Glueck, R. Benkowski, and Y. Nosé, “Hemolytic effect of surface roughness of an impeller in a centrifugal blood pump,” *Artificial Organs*, vol. 21, no. 7, pp. 686–690, Nov. 1997. DOI: [10.1111/j.1525-1594.1997.tb03723.x](https://doi.org/10.1111/j.1525-1594.1997.tb03723.x)

- [87] M. Nishida, T. Negishi, D. Sakota, R. Kosaka, O. Maruyama, T. Hyakutake, K. Kuwana, and T. Yamane, “Properties of a monopivot centrifugal blood pump manufactured by 3D printing,” *Journal of Artificial Organs*, vol. 19, no. 4, pp. 322–329, Dec. 2016. DOI: [10.1007/s10047-016-0914-9](https://doi.org/10.1007/s10047-016-0914-9)
- [88] H. Yu, S. Engel, G. Janiga, and D. Thévenin, “A review of hemolysis prediction models for computational fluid dynamics,” *Artificial Organs*, Jun. 2017. DOI: [10.1111/aor.12871](https://doi.org/10.1111/aor.12871)
- [89] L. Goubergrits, “Numerical modeling of blood damage: Current status, challenges and future prospects,” *Expert Review of Medical Devices*, vol. 3, no. 5, pp. 527–531, 2006. DOI: [10.1586/17434440.3.5.527](https://doi.org/10.1586/17434440.3.5.527)
- [90] R. Paul, F. Schügner, H. Reul, and G. Rau, “Recent findings on flow induced blood damage: Critical shear stresses and exposure times obtained with a high shear couette-system,” *Artificial Organs*, vol. 23, no. 7, Jul. 1999.
- [91] H. Yu, “Flow design optimization of blood pumps considering hemolysis,” Ph.D. dissertation, Universität Magdeburg, 2015.
- [92] B. Thamsen, B. Blümel, J. Schaller, C. O. Paschereit, K. Affeld, L. Goubergrits, and U. Kertzscher, “Numerical analysis of blood damage potential of the HeartMate II and Heartware HVAD rotary blood pumps,” *Artificial Organs*, vol. 39, no. 8, pp. 651–659, Aug. 2015. DOI: [10.1111/aor.12542](https://doi.org/10.1111/aor.12542)
- [93] X. Song, A. L. Throckmorton, H. G. Wood, J. F. Antaki, and D. B. Olsen, “Computational fluid dynamics prediction of blood damage in a centrifugal pump,” *Artificial Organs*, vol. 27, no. 10, pp. 938–941, Oct. 2003. DOI: [10.1046/j.1525-1594.2003.00026.x](https://doi.org/10.1046/j.1525-1594.2003.00026.x)
- [94] T. Zhang, M. E. Taskin, H.-B. Fang, A. Pampori, R. Jarvik, B. P. Griffith, and Z. J. Wu, “Study of flow-induced hemolysis using novel Couette-type blood-shearing devices,” *Artificial Organs*, vol. 35, no. 12, pp. 1180–1186, Aug. 2011. DOI: [10.1111/j.1525-1594.2011.01243.x](https://doi.org/10.1111/j.1525-1594.2011.01243.x)
- [95] K. H. Fraser, M. E. Taskin, B. P. Griffith, and Z. J. Wu, “The use of computational fluid dynamics in the

- development of ventricular assist devices,” *Medical Engineering & Physics*, vol. 33, no. 3, pp. 263 – 280, Apr. 2011. DOI: <https://doi.org/10.1016/j.medengphy.2010.10.014>
- [96] D. Lacasse, A. Garon, and D. Pelletier, “Mechanical hemolysis in blood flow: User-independent predictions with the solution of a partial differential equation,” *Computer Methods in Biomechanics and Biomedical Engineering*, vol. 10, no. 1, pp. 1–12, Feb. 2007. DOI: [10.1080/10255840600985535](https://doi.org/10.1080/10255840600985535)
- [97] A. Garon and M.-I. Farinas, “Fast three-dimensional numerical hemolysis approximation,” *Artificial Organs*, vol. 28, no. 11, pp. 1016–1025, Nov. 2004. DOI: [10.1111/j.1525-1594.2004.00026.x](https://doi.org/10.1111/j.1525-1594.2004.00026.x)
- [98] M. Grigioni, U. Morbiducci, G. D’Avenio, G. Di Benedetto, and C. Del Gaudio, “A novel formulation for blood trauma prediction by a modified power-law mathematical model,” *Biomechanics and Modeling in Mechanobiology*, vol. 4, no. 4, pp. 249–260, Nov. 2005. DOI: [10.1007/s10237-005-0005-y](https://doi.org/10.1007/s10237-005-0005-y)
- [99] P. K. Kundu, I. Cohen, and H. Hu, *Fluid Mechanics*, 6th edition. Elsevier, 2016. DOI: [10.1016/C2012-0-00611-4](https://doi.org/10.1016/C2012-0-00611-4)
- [100] M. M. Faghih and M. Keith Sharp, “Extending the power-law hemolysis model to complex flows,” *Journal of Biomechanical Engineering*, vol. 138, no. 12, Nov. 2016. DOI: [10.1115/1.4034786](https://doi.org/10.1115/1.4034786)
- [101] R. v. Mises, “Mechanik der festen Körper im plastisch-deformablen Zustand,” *Nachrichten von der Gesellschaft der Wissenschaften zu Göttingen, Mathematisch-Physikalische Klasse*, vol. 1913, pp. 582–592, Nov. 1913.
- [102] M. M. Faghih and M. K. Sharp, “Modeling and prediction of flow-induced hemolysis: A review,” *Biomechanics and Modeling in Mechanobiology*, vol. 18, no. 4, pp. 845–881, Aug. 2019. DOI: [10.1007/s10237-019-01137-1](https://doi.org/10.1007/s10237-019-01137-1)
- [103] ANSYS, Inc., “CFX-solver theory guide,” Jan. 2016, release 17.
- [104] C. Bludszuweit, “Three-dimensional numerical prediction of stress loading of blood particles in a centrifugal pump,” *Artificial Organs*, vol. 19, no. 7, pp. 590–596, Jul. 1995. DOI: [10.1111/j.1525-1594.1995.tb02386.x](https://doi.org/10.1111/j.1525-1594.1995.tb02386.x)

- [105] P. Puentener, M. Schuck, D. Steinert, T. Nussbaumer, and J. W. Kolar, “A 150000 rpm bearingless slice motor,” *IEEE/ASME Transactions on Mechatronics*, Dec. 2018. DOI: [10.1109/tmech.2018.2873894](https://doi.org/10.1109/tmech.2018.2873894)
- [106] ASTM Committee and others, *Annual Book of ASTM Standards, F1844-97(2017)*, 2017, vol. 13, chapter Standard practice for assessment of hemolysis in continuous flow blood pumps, pp. 1–5. DOI: [10.1520/F1841-97R17](https://doi.org/10.1520/F1841-97R17)
- [107] H. Schima, M. R. Müller, S. Tsangaris, G. Gheiseder, C. Schlusche, U. Losert, H. Thoma, and E. Wolner, “Mechanical blood traumatization by tubing and throttles in in vitro pump tests: Experimental results and implications for hemolysis theory,” *Artificial Organs*, vol. 17, no. 3, pp. 164–170, Mar. 1993. DOI: [10.1111/j.1525-1594.1993.tb00425.x](https://doi.org/10.1111/j.1525-1594.1993.tb00425.x)
- [108] J. Ding, S. Niu, Z. Chen, T. Zhang, B. P. Griffith, and Z. J. Wu, “Shear-induced hemolysis: Species differences,” *Artificial Organs*, vol. 39, no. 9, pp. 795–802, Apr. 2015. DOI: [10.1111/aor.12459](https://doi.org/10.1111/aor.12459)
- [109] Sigma-Aldrich, “Drabkin’s reagent (d5941) - Product information,” 2015.
- [110] E. Beutler, *Red cell metabolism: A manual of biochemical methods*. Grune & Stratton New York, Jul. 1984.
- [111] W. Rick, “Klinische Chemie,” in *Klinische Chemie und Mikroskopie*. Springer, 1976, pp. 139–287. DOI: [10.1007/978-3-642-96326-1_4](https://doi.org/10.1007/978-3-642-96326-1_4)
- [112] G. Moore, M. Ledford, and A. Merydith, “A micromodification of the Drabkin hemoglobin assay for measuring plasma hemoglobin in the range of 5 to 2000 mg/dl,” *Biochemical Medicine*, vol. 26, no. 2, pp. 167–173, Oct. 1981. DOI: [10.1016/0006-2944\(81\)90043-0](https://doi.org/10.1016/0006-2944(81)90043-0)
- [113] Sigma-Aldrich, “Hemoglobin - Product information,” 1996.
- [114] R. A. Malinauskas, “Plasma hemoglobin measurement techniques for the in vitro evaluation of blood damage caused by medical devices,” *Artificial Organs*, vol. 21, no. 12, pp. 1255–1267, Dec. 1997. DOI: [10.1111/j.1525-1594.1997.tb00486.x](https://doi.org/10.1111/j.1525-1594.1997.tb00486.x)

- [115] T. Koller and A. Hawrylenko, “Contribution to the in vitro testing of pumps for extracorporeal circulation.” *The Journal of Thoracic and Cardiovascular Surgery*, vol. 54, no. 1, pp. 22–9, Jul. 1967. DOI: [10.1016/S0022-5223\(19\)43109-7](https://doi.org/10.1016/S0022-5223(19)43109-7)
- [116] E. F. Bernstein, P. L. Blackshear, and K. H. Keller, “Factors influencing erythrocyte destruction in artificial organs,” *The American Journal of Surgery*, vol. 114, no. 1, pp. 126–138, Jul. 1967. DOI: [10.1016/0002-9610\(67\)90047-5](https://doi.org/10.1016/0002-9610(67)90047-5)
- [117] F. Menter, “Zonal two equation $k-\omega$ turbulence models for aerodynamic flows,” in *23rd Fluid Dynamics, Plasmadynamics, and Lasers Conference*, Jan. 1993, p. 2906. DOI: [10.2514/6.1993-2906](https://doi.org/10.2514/6.1993-2906)
- [118] H. Schlichting and K. Gersten, *Grenzschicht-Theorie*. Springer, 2006. DOI: [10.1007/3-540-32985-4](https://doi.org/10.1007/3-540-32985-4)
- [119] I. Nezu and W. Rodi, “Open-channel flow measurements with a laser Doppler anemometer,” *Journal of Hydraulic Engineering*, vol. 112, no. 5, pp. 335–355, May 1986. DOI: [10.1061/\(ASCE\)0733-9429\(1986\)112:5\(335\)](https://doi.org/10.1061/(ASCE)0733-9429(1986)112:5(335))
- [120] C. D. Andereck, S. S. Liu, and H. L. Swinney, “Flow regimes in a circular Couette system with independently rotating cylinders,” *Journal of Fluid Mechanics*, vol. 164, p. 155–183, Mar. 1986. DOI: [10.1017/S0022112086002513](https://doi.org/10.1017/S0022112086002513)
- [121] H. Minkowski, “Die Grundgleichungen für die elektromagnetischen Vorgänge in bewegten Körpern,” *Mathematische Annalen*, vol. 68, no. 4, pp. 472–525, Dec. 1910. DOI: [10.1007/BF01455871](https://doi.org/10.1007/BF01455871)
- [122] M. Mansuripur, “Force, torque, linear momentum, and angular momentum in classical electrodynamics,” *Applied Physics A*, vol. 123, no. 10, p. 653, 2017. DOI: [10.1007/s00339-017-1253-2](https://doi.org/10.1007/s00339-017-1253-2)
- [123] M. Mansuripur, “The force law of classical electrodynamics: Lorentz versus Einstein and Laub,” in *Optical Trapping and Optical Micromanipulation X*, vol. 8810. International Society for Optics and Photonics (SPIE), Dec. 2013, pp. 55 – 72. DOI: [10.1117/12.2024808](https://doi.org/10.1117/12.2024808)